UNIVERSITÀ
DEGLI STUDI
FIRENZE

DOTTORATO DI RICERCA IN

TECNOLOGIE ELETTRONICHE PER L'INGEGNERIA DELL'INFORMAZIONE

INDIRIZZO "*RF, Microwaves and Electromagnetics*"

CICLO XXVI

CONTRIBUTIONS TO THE ART OF FINITE ELEMENT ANALYSIS IN ELECTROMAGNETICS

ING-INF/02

Laurent Ntibarikure

Coordinatore:

Prof. Gianfranco Manes

Tutori:

Prof. Giuseppe Pelosi

Dr. Stefano Selleri

2011-2013

To Peter P. Silvester, whose teachings left in the nineties at the University of Florence have brought to me a deep interest on the matter.

Sommario

Il metodo degli elementi finiti è un potente metodo per la soluzione di problemi di valori al contorno complessi, governati da equazioni alle differenze parziali. La sua prima applicazione a problemi di ingegneria risale al 1943, anno in cui Courant divulgò la soluzione numerica di un problema di meccanica strutturale [1]. Da allora, vi sono stati numerosi tentativi di applicazione del metodo ad altri campi dell'ingegneria. Silvester, pioniere del metodo nel campo dell'elettromagnetismo applicato, nei suoi primi lavori datati 1969 illustrò la possibilità di risolvere problemi di guida d'onda con tale metodo [2, 3]. Oggi giorno, vasto è il bagaglio di problemi elettromagnetici risolti e validati sperimentalmente. Molti ormai sono gli applicativi disponibili per l'analisi numerica agli elementi finiti di strutture guidanti e radianti.

Nonostante l'immenso sviluppo degli ultimi decenni, vi sono ancora molti problemi da risolvere. Nella presente tesi analizzeremo due di essi, fornendo alcune idee e tecniche risolutive. Il primo riguarda la soluzione di problemi "grandi", irrisolubili con modesti comuni calcolatori, nel tentativo quindi di sfruttare al meglio le risorse computazionali disponibili ed oltrepassarne i limiti attuali. La strada della scomposizione di dominio è quindi stata impegnata. Suddividendo un problema grande in vari sotto-problemi che per le loro dimensioni limitate risultano affrontabili singolarmente, e raccordando opportunamente le singole soluzioni è possible ottenere la soluzione del problema originale. Il secondo problema è legato all'imminente apparizione di materiali con caratteristiche elettromagnetiche intrinsecamente non lineari, ovvero dipendenti dal campo elettromagnetico in essi contenuto. L'analisi a microonde di tali mezzi con un approccio agli elementi finiti convenzionale non consente di raggiungere un sufficiente livello di accuratezza. L'analisi multiarmonica, includendo gli effetti non lineari, consente di migliorare notevolmente l'accuratezza di analisi. Un applicativo per l'analisi agli elementi finiti di problemi tridimensionali è stato implementato al fine di condurre le suddette ricerche.

Abstract

The finite element method is a powerful method for the approximate solution of boundary value problems governed by partial differential equations. A really first application to structural engineering problems, dating 1943, is attributed to R. Courant [1]. Since then, there has been a lot of successful tentatives to apply the method to other fields. In particular, Silvester showed in 1969 [2, 3] that waveguide modes could be easily computed with the method. His work started a long path for finite elements in electromagnetics, with multiple assessments of the method with real-world problems and gradually improving the efficiency of the algorithms. Nowadays, finite elements in computational electromagnetics has become an invaluable part in radio frequency and microwave application designs, and many packages are widely available to perform these tasks.

However, there remain a lot of problems to be solved. In this dissertation, we have inquired in two of these. The first, the efficient solution of large problems which may not be solvable on a single modern computer. Domain decomposition methods have been thus investigated, these allowing to solve smaller parts of a large problem and to achieve the whole solution upon proper interconnection. Two types of domain decomposition methods have been analyzed, leading to the construction of algorithms for solving large electromagnetic problems at a nearly linear complexity. The other, the accurate solution of electromagnetic problems in which some materials behave nonlinearly, that is their properties vary depending on the intensity of the fields they imbue. Almost all materials behave nonlinearly and their effect is just a matter of fields intensities and accuracy requirements. In many microwave applications, the nonlinear effects, necessary for information processing and control, are still limited to lumped devices for their highly developed models. Accurate modeling of bulk or films of nonlinear materials may open the way to a new variety of controllable materials in flexible, reconfigurable, electromagnetic devices. A finite element package has been implemented to perform several tests here documented.

Index Terms: Electromagnetic radiation and scattering, time-harmonic fields, finite element method, domain decomposition methods, nonlinear materials, multiharmonic analysis, harmonic balance.

Acknowledgements

During these years of Ph.D. studies several persons (and I may forget many of them) have contributed to my work and without their support it would have been impossible for me to complete it. That is why I wish to dedicate this section to recognize their support.

I would like to express my sincere gratitude to the professors of my advisors: Prof. Giuseppe Pelosi and Dr. Stefano Selleri, for their guidance, motivation and support during this period.

Special thanks to all the employees, researchers and students of the Computational Electromagnetics laboratory of the Information Engineering department at the University of Florence, for their courtesy, the pieces of advice and help they gave me, and most of all for the good time spent together.

I would also like to express my appreciation to the pieces of knowledge also transferred to me all along my finite element methods for microwave engineering mastering quest by Prof. Romanus Dyczij-Edlinger, Prof. Jin Fa-Lee and Prof. Oszkár Bíró. Deep appreciation also to Dr. Ortwin Farle, for many implementation skills imparted to me during my master thesis work at the *Lehrstuhl für Theoretische Elektrotechnik* laboratory of Saarland University.

I would also like to express my heartfelt gratitude to my family for encouragement and continuous support given throughout my life.

Last but not least I would like to express my appreciation to my sweetheart, Veronica, for her love, patience, support and understanding throughout these difficult and challenging years.

Contents

List of Figures

List of Tables

List of Algorithms

List of Publications

Refereed papers

[1] L. Ntibarikure, G. Pelosi, S. Selleri, "Efficient harmonic balance analysis of waveguide devices with nonlinear dielectrics," *Microwave and Wireless Components Letters, IEEE*, vol. 22, no. 5, pp. 221–223, 2012.

[2] L. Ntibarikure, G. Pelosi, S. Selleri, "Harmonic balance domain decomposition finite elements for nonlinear passive microwave devices analysis," *Special Issue on "Finite Elements for Microwave Engineering", Electromagnetics*, vol. 34, no. 3, 2014.

Conference proceedings

[1] L. Ntibarikure, "Model order reduction in finite element analysis of phased array antennas," in *Numero Speciale 8 - Serie di Elettromagnetismo su "XIX Riunione Nazionale di Elettromagnetismo (RiNEm)", Atti della "Fondazione Giorgio Ronchi"*, vol. LXVIII, no. 4, pp. 97–102, 2012.

Conferences

[1] L. Ntibarikure, G. Pelosi, and S. Selleri, "Harmonic balance domain decomposition finite element for nonlinear passive microwave devices analysis," in *11th International Workshop on Finite Elements for Microwave Engineering – FEM2012*, Estes Park, Colorado, USA, Jun. 4–6, 2012.

[2] L. Ntibarikure, G. Pelosi, S. Selleri, "Harmonic balance finite element analysis of third order intermodulation products in ferrite devices," in *XIX Riunione Nazionale di Elettromagnetismo – XIX RiNEm*, Rome, Italy, Sep. 10–14, 2012.

[3] L. Ntibarikure, "Model order reduction in finite element analysis of phased array antennas," in *XIX Riunione Nazionale di Elettromagnetismo – XIX RiNEm*, Rome, Italy, Sep. 10-14, 2012.

Chapter 1

Introduction

Nowadays, several successful commercial packages for solving electromagnetic problems are available. Such computational electromagnetics software is typically based on one or more "traditional" rigorous (full-wave) techniques such as the finite differences time-domain [4, 5] and the finite element method [6, 7], which are differential based methods, or the method of moments [8] which is integral based, and sometimes include some of their hybridizations [9–11]. The robust formulations they implement have been validated throughout decades by multiple physical measurements of real-life applications, up to the point they form an invaluable part of current radio frequency and microwave engineering practice. Without these computational modeling methods, probably many highly technological applications would not have been realized yet.

However, many challenging applications still remain to be tackled due to the limited availability of computational resources. The higher is the electrical size of the problem, even if quite geometrically simple, the higher becomes the number of unknowns required to compute the fields and other related parameters. Some of these are large antenna arrays, antenna platform positioning problems, radar cross section of electrically large targets and with composite materials, terahertz and optical devices. The problem size, in terms of unknowns N necessary for an acceptable (error controlled) analysis at a frequency f, typically scales as $N \propto O(f^3)$ for differential based methods and as $N \propto O(f^2)$ for integral methods [12]. The same behavior is encountered for geometrically complicated models. Even if smaller than the wavelength, better accuracy is needed around the conductors corners and at interfaces between materials, some of the known sources of field singularities. Some of these applications are the frequency selective surfaces used as electromagnetic coatings and the signal integrity computation in high frequency integrated circuits [12, 13]. A combination of geometrical and electromagnetic size complexities can be found in recent nano-optical applications, frequencies at which metals behave as high permittivity materials due to surface plasmons surrounded by the unitary permittivity of the air [14]. Accurate solution of these kind of problems is still an active research field [15].

Among all the problems that still remain to be solved, those comprehending nonlinear materials are still currently faced by the computational electromagnetics community, principally by the use of finite differences time-domain schemes which allow for straightforward implementation of nonlinearities [16–23]. The main investigated fields of application initially were at optical frequencies, including harmonic generation, nano-plasmonics and solitons propagation in Kerr-like media. In fact, very high intensity fields are typically generated at those frequencies by lasers or even light emitting diodes, and hence materials that at microwave frequencies may behave as linear cannot anymore be accurately handled at optical ones with linear solvers. At lower frequencies, for the solution magneto-quasi-static problems like eddy currents in ferromagnetic materials ones, a method using finite elements was early introduced by Silvester in 1970 [24]. A time-harmonic scheme was there presented, allowing for fast computation of steady state fields. However, information on the distortion introduced by permeability saturation was still neglected. Years later, Yamada et al. [25–27] introduced a first multi-harmonic scheme, the harmonic balance finite element method, allowing for accurate treatment of nonlinearities [28–31]. Contemporaneously, finite element time domain schemes where introduced to allow transient analyzes [32]. However, due to the immediate extrapolation of steady state fields which indeed are almost always sought for, a frequency-domain scheme often result to be preferable. It still appears that no multi-harmonic schemes have been employed from microwaves to optical frequencies.

1.1 Efficient solvers for computational electromagnetics

Even if they perform worse in terms of electrical size, differential based methods, leading to sparse matrices, can be directly solved with an asymptotic complexity of $O(N^2)$ [33] while the dense matrices of integral methods can be directly inverted with $O(N^3)$ complexity [34]. Furthermore, linear solvers (either stationary or not) behave dramatically worse as N grows, thus require a particular attention to preconditioning in order to restore their performances. Three main approaches have been successfully adopted to steer the computational complexities of electromagnetic solvers down to linear or $O(N \log N)$:

- *Multigrid methods*, which to some extent are based on multiple superimposed discretization levels, where the information derived from a coarse level (where a direct solver performs better) can be used to accelerate the computations on a finer level with a linear solver. This hierarchical decomposition of accuracy levels have been successfully employed for differential based methods [35–41]. The integral based multigrid methods, referred as “multiresolution methods” [42, 43], are not yet affirmed as their differential counterparts.

- *Domain decomposition methods*, which follows the *divide et impera* strategy, dividing a wide fine grid into smaller parts where the field solutions can be easily

computed, then proper transmission conditions or subdomains coupling strategy have to be enforced in order to recover the fields within the whole domain [44–46] . These methods have been extensively studied and employed to solve Maxwell's equations [47–63] for both differential and integral methods (or their hybridization) up to tens of millions of unknowns with common personal computers.

- *Multipole methods*, which fundamentally group local method of moments near field solutions into multipoles that allow to compute far field couplings between the groups. These methods are intrinsically related to integral based methods, where dipole or multipoles can be accurately handled. They are known as the *fast multipole method* or *multilevel fast multipole algorithm* [64, 65] for integral equations.

In many cases, several difficulties remain for all the aforementioned methods. Typically based on some precise assumptions for which the iterative solvers they employ should converge, the end-user of the method still have to be highly skilled and experienced in order to properly conduct the analyzes. A lot of efforts still have to be done in order to achieve robust solvers, especially from the mathematics behind the implemented code.

Also, several improvements have been achieved to perform fast parameter sweeps. Once some solutions, for some parameter values, are computed by one of the previous "traditional" or efficient methods, fast intermediate solutions can be obtained by proper interpolation schemes. These are known as the *model order reduction* methods [66, 67] for differential based methods or as the *characteristic basis functions* methods [68] for integral based methods. Several parameter dependent solutions of full-wave methods are collected and orthonormalized with some spectral decomposition (Gram-Schmidt) or singular value decomposition. These solution vectors are then used to expand large-scale solutions on which the orginal problem is projected. Finally, if these solutions constitute a basis for the whole function space, then a few operations are sufficient to perform a parameter sweep with a controlled order of accuracy. The parameters can be the frequency of analysis, material properties, complex excitation amplitudes of a multiport device and many others. In principle, the large cost of multiple solutions computation in a parameter sweep is truncated once a good basis is found.

Among the "traditional" methods, differential based methods allow a straightforward treatment of materials properties and, for the finite element method, a better discretization of geometrical bodies. Integral methods are better suited for open problems, where the differential based methods require approximative boundary truncation techniques to implement Sommerfeld's radiation condition: absorbing boundary condtions [69, 70] or perfectly matched layers (PMLs) [71]. However, many successful hybridization of differential based and integral based methods have been reported [72, 73]. It is worth noticing that the introduction of integral equa-

tions has a significant drawback in reducing the computational efficiency [51]. This has led to the choice of the finite element method as core development for efficient schemes that will be analyzed throughout this dissertation.

1.2 A reason for nonlinear analyzes at microwaves

It is well known that polycrystalline magnetic oxides like ferrites or other ferromagnetic compounds such the yttrium iron garnet, for their anisotropy, can be used to realize non-reciprocal microwave devices such as circulators, isolators and phase shifters [74, 75]. It is also known that these devices are typically critical when dealing with high power electromagnetic fields, due to the spurious fields they induce [76–78]. Ferromagnetic materials were probably the first to present a nonlinear behavior at microwave frequencies. Very few attempts to predict the spurious fields generated in such devices have been reported in literature [79, 80].

Known as *passive intermodulation*, the nonlinearities cause a critical limit in the design of microwave systems [81] and their calculation methods are still very limited. This phenomenon is also imparted to metal contacts [82], metallic wires and dielectric cables [83] and particularly to metals oxidation [84]. In a general form, these can be viewed as nonlinear electromagnetic properties of materials, that is field dependent permittivities, permeabilities and conductivities.

Also, during the last two decades, due to several improvements in the field of digital electronics, when seeking for thin-films materials with high permittivities to implement the capacitances in dynamic random access memories [85, 86], barium strontium titanate compounds have demonstrated a noticeable nonlinear behavior at microwave frequencies [87–90]. Their electro-optic effect [91], principally due to a second order or Kerr-like permittivity, can hence be exploited to design tunable capacitors [92], or in general to control the characteristics of any microwave device that use this kind of materials.

Finite elements can considerably help in the computation of nonlinear phenomena products, especially for its capability to straightforwardly handle material properties and geometries. Once again, it is the best suited computational electromagnetic method for nonlinear analyzes.

1.3 Contributions of this dissertation

The chosen fields of research have led to the implementation of a finite element software, namely “FES”. Several formulations have been implemented in FES, basically based on the application of the Galerkin framework on both two- and three-dimensional domains. The two-dimensional package, FES-2D, mainly coded in the high level Matlab® language, was prevalently used to assess the formulations, which might result to be excessively time demanding to implement in lower level of abstrac-

tion languages. Then, the transfer of the formulations to tree-dimensional problems in FES-3D could be done relatively faster in an objective paradigm C++ code. FES-3D, using several third party, open source[1], codes, some written in Fortran or C, has been compiled with the GNU GCC 4.8.1 on x86_64 architectures with the -Ofast optimization flag enabled.

The present dissertation is structured as follows:

- The second chapter introduces to the electromagnetic radiation mechanism, which is known since more than a century to be governed by a set of partial differential equations collected into Maxwell's equations. A wave equation for the electric field is then derived, allowing for single partial differential equation solution. It is well known that this equation can be accurately solved by numerical methods as long as the frequency of analysis is above the lower limit that causes badly conditioned matrices, which is the case for all the experiments conducted here. The Galerkin framework is then introduced, with the necessary mathematical background to understand its efficacy. Finally, the formulations employed to solve, later on, several waveguide and radiation problems are introduced. Within this phase, the FES results are compared to commercial models analyzes for validation purposes.

- In the third chapter, the domain decomposition concept is introduced with two different schemes, the Schur complement and the finite element tearing and interconnecting. Both the methods are tested on the simple case of a rectangular waveguide. Preconditioners for Krylov subspace methods are then built on a domain decomposition scheme and the convergence behavior is analyzed extensively. Finally, the numerical complexity of the method is derived to ensure its applicability to very large problems.

- In the fourth chapter, the first known attempt to apply the harmonic balance finite element method to microwave problems is presented. Almost all passive nonlinear problems require steady state computations and hence the method results to be very well suited. Several test cases on two-dimensional problems are shown to explain the method. One of the previous domain decomposition schemes have also been employed to accelerate the nonlinear analyzes. A three-dimensional barium strontium titanate based test case is shown, somehow proving the capabilities of the method.

- Finally, some conclusions will be drawn in the last chapter. The analyzed and implemented methods open the way to many, still unperformed, analyzes. A possible outlook, matter of emerging technologies, will be hence discussed.

[1] Almost all the employed third party codes are at least provided with the in the Lesser General Public Licence, and some where totally free for reuse.

Chapter 2

Finite elements for the wave equation

This chapter introduces the boundary value problem that describes the radiation mechanism in an unbounded medium. The vector wave equation is then derived from Maxwell's eqations, being the partial differential equation that describes waves propagation. The finite element formulation for the electric field wave equation follows, presented for a full wave solution of electromagnetic radiation problems. Several boundary conditions, that will be used throughout this dissertation, will be introduced here, allowing for the treatment of fields propagation analysis from either waveguides ports or free-space impinging waves. Some test cases will be shown, comparing to a commercial package, analyzing the FES implemented formulations behavior. FES is the core of the domain decomposition and the nonlinear analyzes presented, respectively, in chapters 3 and 4.

2.1 Radiation in an unbounded medium

The problem of electromagnetic radiation from a generic distribution of current sources in a unbounded medium relies on the solution of the Maxwell's equations [93]

$$\nabla \times \boldsymbol{\mathcal{E}}(\mathbf{r},t) = -\frac{\partial}{\partial t}\boldsymbol{\mathcal{B}}(\mathbf{r},t) \qquad \textit{Faraday's law}, \tag{2.1.1}$$

$$\nabla \times \boldsymbol{\mathcal{H}}(\mathbf{r},t) = \frac{\partial}{\partial t}\boldsymbol{\mathcal{D}}(\mathbf{r},t) + \boldsymbol{\mathcal{J}}(\mathbf{r},t) \qquad \textit{Maxwell-Ampère's law}, \tag{2.1.2}$$

$$\nabla \cdot \boldsymbol{\mathcal{D}}(\mathbf{r},t) = \varrho(\mathbf{r},t) \qquad \textit{Poisson's equation}, \tag{2.1.3}$$

$$\nabla \cdot \boldsymbol{\mathcal{B}}(\mathbf{r},t) = 0 \qquad \textit{Gauss' law for magnetism}, \tag{2.1.4}$$

where $\boldsymbol{\mathcal{E}}$ is the *electric field intensity*, which carries the S.I.[1] units $\frac{\mathrm{V}}{\mathrm{m}}$, $\boldsymbol{\mathcal{H}}$ the *magnetic field intensity* in $\frac{\mathrm{A}}{\mathrm{m}}$, $\boldsymbol{\mathcal{D}}$ the *electric displacement* in $\frac{\mathrm{C}}{\mathrm{m}^2}$ (or $\frac{\mathrm{As}}{\mathrm{m}^3}$), $\boldsymbol{\mathcal{B}}$ the *magnetic induction*

[1] Système International d'unités.

in $\frac{\mathrm{Wb}}{\mathrm{m}^2}$ (or $\frac{\mathrm{Vs}}{\mathrm{m}^2}$), $\mathcal{J}$ the *electric current density* in $\frac{\mathrm{A}}{\mathrm{m}}$ and ϱ the *electric charge density* in $\frac{\mathrm{C}}{\mathrm{m}^3}$ (or $\frac{\mathrm{As}}{\mathrm{m}^3}$). All these values are dependent on the position vector $\mathbf{r} \in \mathbb{R}^3$ and on the time variable $t \in \mathbb{R}$. Combining the divergence of (2.1.2) with (2.1.3), we obtain the *current continuity equation*

$$\nabla \cdot \mathcal{J}(\mathbf{r}, t) + \frac{\partial}{\partial t} \varrho(\mathbf{r}, t) = 0. \tag{2.1.5}$$

In order to solve Maxwell's system of first order partial differential equations (PDEs), it is necessary to provide the *boundary conditions* and the *initial conditions*. Furthermore, as the number of equations is less than the number of unknowns, we need to supply the *constitutive relations*, which relates the electric displacement and the magnetic induction to the fields

$$\mathcal{D}(\mathbf{r}, t) = \overline{\overline{\epsilon}}(\mathbf{r}, t) \cdot \mathcal{E}(\mathbf{r}, t) \tag{2.1.6}$$

$$\mathcal{B}(\mathbf{r}, t) = \overline{\overline{\mu}}(\mathbf{r}, t) \cdot \mathcal{H}(\mathbf{r}, t), \tag{2.1.7}$$

where $\overline{\overline{\epsilon}}$ and $\overline{\overline{\mu}}$ are dyadic tensors depending on the material in which the fields exist[2]. Also, in presence of conductive materials, the electric field gives birth to an electric current density

$$\mathcal{J}^c(\mathbf{r}, t) = \overline{\overline{\sigma}}(\mathbf{r}, t) \cdot \mathcal{E}(\mathbf{r}, t) \qquad \textit{Ohm's law}, \tag{2.1.8}$$

where $\overline{\overline{\sigma}}$ is the *electric conductivity* dyadic tensor in $\frac{\mathrm{S}}{\mathrm{m}}$, and the superscript c on $\mathcal{J}^c(\mathbf{r}, t)$ indicates that the current density is induced by the electric field. With this additional equation, the current $\mathcal{J}(\mathbf{r}, t)$ in (2.1.2) can be considered to be composed by an induced part, $\mathcal{J}^c(\mathbf{r}, t)$, and by an impressed part, $\mathcal{J}^i(\mathbf{r}, t)$, the latter actually being the source generating the electromagnetic fields.

The boundary conditions ensure the continuity of the fields at the interfaces between different media, and this is stated as[3], for a surface interfacing two media,

$$\hat{\mathbf{n}} \times (\mathcal{E}_1(\mathbf{r}, t) - \mathcal{E}_2(\mathbf{r}, t)) = 0, \tag{2.1.9}$$

$$\hat{\mathbf{n}} \times (\mathcal{H}_1(\mathbf{r}, t) - \mathcal{H}_2(\mathbf{r}, t)) = \mathcal{J}_s(\mathbf{r}, t), \tag{2.1.10}$$

$$\hat{\mathbf{n}} \cdot (\mathcal{D}_1(\mathbf{r}, t) - \mathcal{D}_2(\mathbf{r}, t)) = \varrho_s(\mathbf{r}, t), \tag{2.1.11}$$

$$\hat{\mathbf{n}} \cdot (\mathcal{B}_1(\mathbf{r}, t) - \mathcal{B}_2(\mathbf{r}, t)) = 0, \tag{2.1.12}$$

where $\hat{\mathbf{n}}$ is the unit vector normal to the surface, outwardly directed from the first region. $\mathcal{J}_s$ and ρ_s are the *electric surface current density* in $\frac{\mathrm{A}}{\mathrm{m}}$ and *electric surface charge density* in $\frac{\mathrm{C}}{\mathrm{m}^2}$.

For the radiation problem we need to solve in this chapter, we will consider *isotropic* (*homogeneous*) and *time-invariant* media, for which the dyadics relating the

[2]The constitutive relations in (2.1.6-2.1.7) are stated in a form such that they can represent *isotropic* and *anisotropic* media.

[3]The continuity equations (2.1.9-2.1.12) are derived from an integral solution of the Maxwell's equations, assuming a connected volume made by a part of region 1 and a part of region 2, i.e. a closed surface crossing the boundary interface between the two regions.

fields to the electric displacement and magnetic induction are scalar values (diagonal tensors with equal entries). Thus, the constitutive relations become

$$\boldsymbol{\mathcal{D}}(\mathbf{r},t) = \epsilon\boldsymbol{\mathcal{E}}(\mathbf{r},t) = \epsilon_0\epsilon_r\boldsymbol{\mathcal{E}}(\mathbf{r},t), \tag{2.1.13}$$

$$\boldsymbol{\mathcal{B}}(\mathbf{r},t) = \mu\boldsymbol{\mathcal{H}}(\mathbf{r},t) = \mu_0\mu_r\boldsymbol{\mathcal{H}}(\mathbf{r},t), \tag{2.1.14}$$

where the constant $\epsilon_0 = 8.854 \cdot 10^{-12}\ \frac{\mathrm{F}}{\mathrm{m}}$ is the *free-space permittivity*, ϵ_r the *relative permittivity*, a non-dimensional constant, $\mu_0 = 4\pi \cdot 10^{-7}\ \frac{\mathrm{H}}{\mathrm{m}}$ is the *free-space permeability* and μ_r the *relative permeability*, also non-dimensional. As we expect electromagnetic waves to be propagating, we denote their speed as $c = \frac{1}{\sqrt{\epsilon\mu}} = \frac{c_0}{\sqrt{\epsilon_r\mu_r}}$ with $c_0 \approx 2.998 \cdot 10^8\ \frac{\mathrm{m}}{\mathrm{s}}$ the *free-space speed of light*.

For the solution of Maxwell's equations, there must be also given the initial conditions, that is, the values of the sources and the fields on the boundaries at the initial observation time $t = t_0$. Our treatment will consider the frequency-domain formulation of the fields invoking the spectral representation of time dependent fields by the *Fourier integral theorem*

$$\psi(\mathbf{r},t) = \frac{1}{2\pi}\int_{-\infty}^{\infty}\Psi(\mathbf{r},\omega)\mathrm{e}^{j\omega t}d\omega.$$

Applying the *Fourier integral theorem* to the Maxwell's equations (2.1.1-2.1.4), we obtain

$$\nabla\times\mathbf{E}(\mathbf{r},\omega) = -j\omega\mathbf{B}(\mathbf{r},\omega), \tag{2.1.15}$$

$$\nabla\times\mathbf{H}(\mathbf{r},\omega) = j\omega\mathbf{D}(\mathbf{r},\omega)+\mathbf{J}(\mathbf{r},\omega), \tag{2.1.16}$$

$$\nabla\cdot\mathbf{D}(\mathbf{r},\omega) = \rho(\mathbf{r},\omega), \tag{2.1.17}$$

$$\nabla\cdot\mathbf{B}(\mathbf{r},\omega) = 0, \tag{2.1.18}$$

and to the continuity equation we obtain

$$\nabla\cdot\mathbf{J}(\mathbf{r},\omega)+j\omega\rho(\mathbf{r},\omega) = 0, \tag{2.1.19}$$

where we have used the Fourier integral of the time derivatives operator

$$\frac{\partial}{\partial t}\psi(\mathbf{r},t) \longleftrightarrow j\omega\Psi(\mathbf{r},\omega),$$

ω being the angular frequency ($\omega = 2\pi f$ with f the frequency in Hz) and $j = \sqrt{-1}$. The frequency dependent function $\Psi(\mathbf{r},\omega)$ represents the spectrum of the time dependent function $\psi(\mathbf{r},t)$, obtained by the *Fourier Transform*

$$\Psi(\mathbf{r},\omega) = \int_{-\infty}^{\infty}\psi(\mathbf{r},t)\mathrm{e}^{-j\omega t}dt \qquad \in\mathbb{C},\ \forall\omega\in\mathbb{R}.$$

The spectral formulation allows us to neglect the initial conditions, the spectrum being computed by an integral over the entire domain of t ($t\in\mathbb{R}$). Also, with the spectral representation, the constitutive relations in isotropic media become

$$\mathbf{D}(\mathbf{r},\omega) = \epsilon_0\epsilon_r\mathbf{E}(\mathbf{r},\omega), \tag{2.1.20}$$

$$\mathbf{B}(\mathbf{r},\omega) = \mu_0\mu_r\mathbf{H}(\mathbf{r},\omega). \tag{2.1.21}$$

2.2 The time harmonic wave equation

The solutions $\mathbf{E}(\mathbf{r},\omega)$ and $\mathbf{H}(\mathbf{r},\omega)$ of the Maxwell equations (2.1.15-2.1.18), can be computed using the *frequency-domain wave equations* in the electric field, obtained combining the curl of Faraday's equation (2.1.15) and the constitutive relation (2.1.21),

$$\nabla \times \frac{1}{\mu_r}\nabla \times \mathbf{E}(\mathbf{r},\omega) \quad = \quad -j\omega\mu_0 \nabla \times \mathbf{H}(\mathbf{r},\omega), \tag{2.2.1}$$

then, by the use of Maxwell-Ampère's law (2.1.16) and the constitutive relation (2.1.20), we obtain

$$\nabla \times \frac{1}{\mu_r}\nabla \times \mathbf{E}(\mathbf{r},\omega) - k_0^2 \epsilon_r \mathbf{E}(\mathbf{r},\omega) \quad = \quad -jk_0\zeta_0 \mathbf{J}(\mathbf{r},\omega), \tag{2.2.2}$$

where $k_0 = \omega\sqrt{\epsilon_0\mu_0} = \frac{\omega}{c_0} = \frac{2\pi}{\lambda_0}$ is the *free space wavenumber* in $\frac{1}{\mathrm{m}}$, with λ_0 the *free space wavelength* in meters, and $\zeta_0 = \omega\sqrt{\frac{\mu_0}{\epsilon_0}}$ is the *free space impedance* in Ω[4]. The solutions of these second-order PDEs are the same as the ones of the first-order Maxwell's PDEs, as long as the fields are spatially twice differentiable everywhere. As we will see later, this complication will be removed with the introduction of the weak form employed in the finite elements formulation.

Throughout this dissertation, we will analyze bounded media. Due to computational resources limitations, the real-world domain is restricted to the parts where the fields are to be computed, encompassing the device or object to analyze. As we will see later, proper boundary conditions will be used to enforce continuity of the fields from the domain to the surrounding and *viceversa*. Furthermore, we will consider the computational domain devoid of electromagnetic fields sources, hence $\mathbf{J}^i(\mathbf{r},\omega)$ can be drop in (2.2.2), keeping only the induced current densities $\mathbf{J}^c(\mathbf{r},\omega)$. Also, we will consider the electric field to have a *time-harmonic* dependence (and so will have the magnetic field) of the form

$$\boldsymbol{\mathcal{E}}(\mathbf{r},t) = \mathfrak{Re}\left(\tilde{\boldsymbol{\mathcal{E}}}(\mathbf{r})\, \mathrm{e}^{j\omega t}\right) \quad \leftrightarrow \quad \mathbf{E}(\mathbf{r}). \tag{2.2.3}$$

Only one frequency will be treated at a time where material properties behave linearly (independent form the electromagnetic fields flowing through them), and in nonlinear analyzes (Chapter 4), materials will receive a special treatment in order to consider the higher-order harmonics generated, and their coupling behavior. As a result, the time-harmonic wave equation for the electric field can be written as

$$\nabla \times \frac{1}{\mu_r}\nabla \times \mathbf{E} + jk_0\zeta_0\sigma\mathbf{E} - k_0^2\epsilon_r\mathbf{E} \quad = \quad 0, \tag{2.2.4}$$

where, for the sake of simplicity, $\mathbf{r}$ have been drop. Once (2.2.4) is solved for $\mathbf{E}$, the magnetic field $\mathbf{H}$ can be straightforwardly recovered with of the use of (2.1.15),

[4] One can straightforwardly deduce that the scalar term $\omega\mu_0$ that scales the current density is equivalent to $k_0\zeta_0$.

together with the constitutive relations. For instance,

$$\mathbf{H} = \frac{\nabla \times \mathbf{E}}{-jk_0\zeta_0\mu_r}. \tag{2.2.5}$$

2.3 Finite element method

The principal peculiarity of the finite element method (FEM) is the division of a given domain Ω into a set of simple subdomains, called *finite elements*. The underlying principle of the method is to replace the entire continuous domain with a number of interconnected finite elements, the so-called *mesh* $\mathcal{M}_h(\Omega)$), in which the unknown function is approximated by a finite linear combination of simple basis functions or *shape functions* with unknown coefficients. Then, the local system of algebraic relations, related to the PDE we wish to solve, is derived in each element upon applying either the Rayleigh-Ritz Method (variational procedure) or, most commonly, the Weighted Residual Method in the Galerkin framework. Finally, the local systems of equations computed for each element are assembled to obtain a global system of equations to solve for the unknown function over the whole domain Ω.

The main four steps of the FEM procedure can be summarized as follows:

- *Preprocessing*: define the computational domain Ω of the problem, select the domain truncation method (waveports truncation and radiation boundaries for electromagnetic problems) building a pertinent CAD (Computer Aided Design) model, select the types of finite elements and discretize the domain with finite elements to create the mesh $\mathcal{M}_h(\Omega)$,
- *Assembly*: after accurate evaluation of the function space of the problem to be solved, select the basis functions and their polynomial order. Then generate the element matrices by the application, over each element, of the Rayleigh-Ritz Method or the Weighted Residual Method to the PDE. The integral equation of the previous methods may allow, depending on the PDE, to obtain the weak variational form upon applying integration by parts. Assemble the local element matrices to form the global system of equations which will be sparse due to the compact supports of the basis funcions, and finally impose the boundary conditions,
- *Solution*: the resulting global system of equations, stated in a matrix form, can now be solved either with direct methods (Gaussian elimination optimized for sparse matrices, maybe after LU or Cholesky factorization) or iterative methods (stationary or Krylov subspace), with proper preconditioning (Incomplete LU or Cholesky, Successive Over Relaxation, Jacobi, Gauss-Seidel) of the system matrix,
- *Postprocessing*: retrieve the interpolated function to extract the parameters of interest (modal scattering parameters, radiation pattern, radar cross section or simply the fields for visualization).

2.3.1 Mesh generation

The mesh generation is perhaps the most important and difficult phase of the FEM procedure as it affects the computational requirements (both memory and CPU times), and the accuracy of the results. The shape of elements should provide the best conformity of the mesh to the CAD model, especially for complex geometries. Common element shapes (Fig. 2.1) are triangles and quadrilaterals for 2D models, tetrahedra and hexahedra for 3D models [94]. Triangles and tetrahedra are called simplices. A fundamental characteristic of simplices is that any polygon or polyhedron can be expressed as the union of simplices. This renders them the best suited to model curved surfaces and irregular regions (Fig. 2.2).

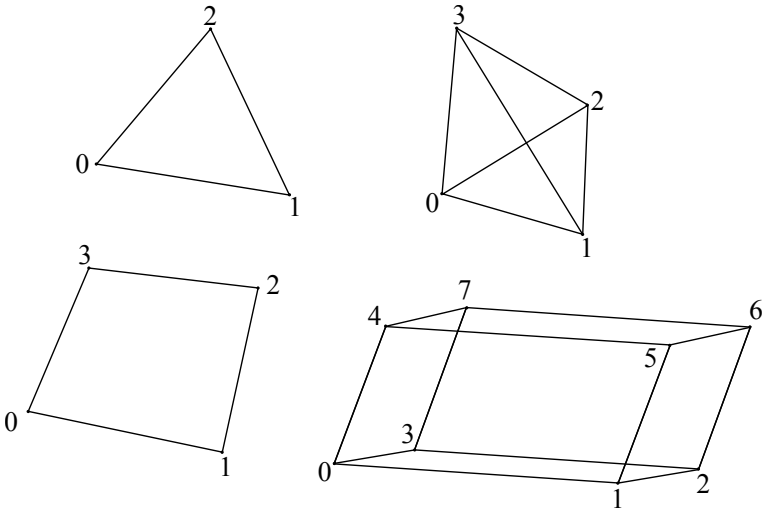

Figure 2.1: Common element shapes. Left to right, top to bottom: triangle, tetrahedron, quadrilateral and hexahedron.

As the mesh is used as the support for a piecewise linear approximation of a function, the accuracy of the approximation directly depends on the sizes and shapes of the elements. If the elements are small enough (typically less than $\frac{\lambda}{10}$ per side), then the field inside the element can be reliably approximated by linear polynomials. For greater dimensions, one may increase the polynomial order to achieve better approximation at the cost of an increase of the interpolation coefficients number.

The accuracy is also related to the elements shape and how far they are to be "regular" or equilateral: there is a mathematical connection between the mesh "quality", the interpolation errors and the global matrix conditioning [15]. Low quality, "needle-like", elements may increase the condition number of the system matrix (poor conditioning), and consequently, may cause a degradation in the accuracy of the results. There have been a lot of efforts in finding the best compromise between the generation of good quality mesh while containing the computational requirements. The most diffused approach is the adaptive mesh refinement (h-AMR), where appropriately chosen error indicators (mainly based on the gradient of the function) are used to refine locally higher error elements (next to metallic corners, disconti-

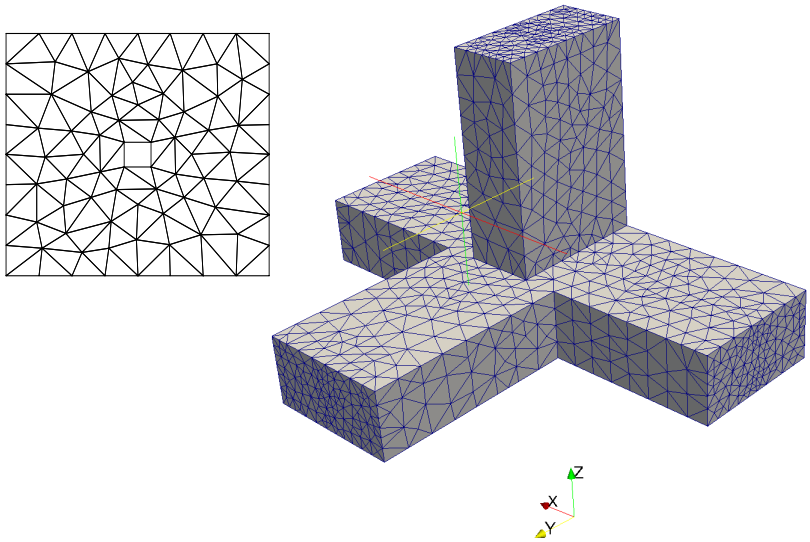

Figure 2.2: Finite element meshes. Left to right: triangularization a square domain surrounding a small square, tetrahedralization of microwave Magic-Tee.

nuities in material properties and any other potential singularity of the function) of the mesh [37, 95]. Other approaches are a combination of the elements refinements (h-refinements) and the polynomial orders refinements (p-refinements) which lead to a better compromise [96].

FES package integrates, in the 2D form, the Triangle Mesh Generator [97] and, in the 3D form, TetGen [98]. Both are based on the Delaunay triangulation which intrinsically allow for optimized mesh quality control, even for really complex geometries. Also, for validation purposes, meshes generated from commercial packages, Comsol (2D) and HFSS (3D), can be imported in the analogous version of FES, restricting in such a way the errors to the steps of the finite element method following the mesh generation, mainly assembly and solve steps.

2.3.2 Shape functions

Accurate definition of the functional space of the solution is necessary to obtain physical solutions. In fact, the PDE with the necessary boundary conditions (initial conditions neglected for the time-harmonic assumption) treated until now, in a totally continuous space, are sufficient to prove existence and uniqueness of the solution. In a discretized world, this might not be true. However, one of the most important results of numerical solution of PDE is given by Cea's theorem [99], the equivalent functional analysis's Max-Milgram theorem, which in simple terms states that once one can prove that a linear operator (the PDE) on a specific functional space is bounded, then the numerical solution to the PDE exists and is unique within a bounded error (maximum error). Furthermore, as the finite discretization tends to the continuous case ($\mathcal{M}_h(\Omega) \to \Omega$), the error tends to vanish. This is the fundamen-

tal aspect of the finite elements: there is a convergence of the numerical solution to the exact solution.

As a consequence, we need to provide the proper function spaces in which the operators for Maxwell's equations (curls, divergences, gradients) are bounded. We define the "boundedness" of the solution in Ω in terms of the Euclidean distance or, more generally, the Lebesgue space $\mathcal{L}^2(\Omega)$. Furthermore, we define the D-dimensional ($D := 2, 3$) Lebesque space to be a Hilbert space in such a way that

$$\left(\mathcal{L}^2(\Omega)\right)^D = \left\{ \mathbf{v} : \Omega \to \mathbb{C}^D \mid \|\mathbf{v}\|_{(\mathcal{L}^2(\Omega))^D} = \int_\Omega |\mathbf{v}|^2 d\Omega < \infty \right\}.$$

To guarantee the boundedness of differential operators in vector spaces, we introduce some important Sobolev spaces [100].

2.3.2.1 $\mathcal{H}^1(\Omega)$ Sobolev space

One of the Sobolev spaces, related to all the square integrable functions that have square integrable gradient, is defined as

$$\mathcal{H}^1(\Omega) = \left\{ \phi \in \mathcal{L}^2(\Omega) \mid \nabla\phi \in (\mathcal{L}^2(\Omega))^D \right\},$$

with the norm

$$\|\phi\|_{\mathcal{H}^1(\Omega)} = \left(\|\phi\|^2_{\mathcal{L}^2(\Omega)} + \|\nabla\phi\|^2_{(\mathcal{L}^2(\Omega))^D} \right)^{1/2}.$$

As we will see, this is the "home" space for the electric field in 2D transversal magnetic formulation for the wave equation. This space and related formulations have been used extensively to assess the domain decomposition and nonlinear analyses of chapters 3 and 4. More generally, this is the home for scalar potentials and for electric charge densities.

2.3.2.2 $\mathcal{H}(\text{curl}, \Omega)$ Sobolev space

Another important Sobolev space, related to all the square integrable functions that have square integrable curl, is defined as

$$\mathcal{H}(\text{curl}, \Omega) = \left\{ \mathbf{v} \in (\mathcal{L}^2(\Omega))^D \mid \nabla \times \mathbf{v} \in (\mathcal{L}^2(\Omega))^D \right\},$$

with the norm

$$\|\mathbf{v}\|_{\mathcal{H}(\text{curl},\Omega)} = \left(\|\mathbf{v}\|^2_{(\mathcal{L}^2(\Omega))^D} + \|\nabla \times \mathbf{v}\|^2_{(\mathcal{L}^2(\Omega))^D} \right)^{1/2}.$$

This space fundamentally represents the electric and magnetic field intensities, **E** and **H**, within Maxwell's equations.

2.3.2.3 $\mathcal{H}(\mathrm{div},\Omega)$ Sobolev space

Another important Sobolev space, related to all the square integrable functions that have square integrable divergence, is defined as

$$\mathcal{H}(\mathrm{div},\Omega)=\left\{\mathbf{v}\in(\mathcal{L}^2(\Omega))^D \mid \nabla\cdot\mathbf{v}\in(\mathcal{L}^2(\Omega))^D\right\},$$

with the norm

$$\|\mathbf{v}\|_{\mathcal{H}(\mathrm{div},\Omega)}=\left(\|\mathbf{v}\|^2_{(\mathcal{L}^2(\Omega))^D}+\|\nabla\cdot\mathbf{v}\|^2_{(\mathcal{L}^2(\Omega))^D}\right)^{1/2}.$$

This space fundamentally represents the electric and magnetic inductions intensities, **D** and **B**, and the electrical current density **J** within Maxwell's equations.

2.3.2.4 de Rham complex

Here comes an interesting result pertaining to the Sobolev spaces defined above: the vector identities $\nabla\times\nabla\phi=0$ and $\nabla\cdot\nabla\times\mathbf{v}=0$, where $\phi\in\mathcal{H}^1(\Omega)$ and $\mathbf{v}\in\mathcal{H}(\mathrm{curl},\Omega)$, can be used to establish a relationship between the spaces. For instance, in view of identity $\nabla\times\nabla\phi=0$, $\nabla\phi\in\mathcal{H}(\mathrm{curl},\Omega)$ and $\nabla\cdot\nabla\times\mathbf{v}=0$ implies $\nabla\times\mathbf{v}\in\mathcal{H}(\mathrm{div},\Omega)$. These relationships can be summarized as

$$\mathcal{H}^1(\Omega)\xrightarrow{\nabla}\mathcal{H}(\mathrm{curl},\Omega)\xrightarrow{\nabla\times}\mathcal{H}(\mathrm{div},\Omega)\xrightarrow{\nabla\cdot}\mathcal{L}^2(\Omega),$$

and important mapping can be immediately visualized with this so-called de Rham complex: gradients map $\mathcal{H}^1(\Omega)$ to $\mathcal{H}(\mathrm{curl},\Omega)$ and curls map $\mathcal{H}(\mathrm{curl},\Omega)$ to $\mathcal{H}(\mathrm{div},\Omega)$.

The electromagnetic quantities and their corresponding function space are shown in table 2.1.

Quantity	Function space
$\mathbf{E},\mathbf{H}$	$\mathcal{H}(\mathrm{curl},\Omega)$
$\mathbf{D},\mathbf{B},\mathbf{J}$	$\mathcal{H}(\mathrm{div},\Omega)$
ρ	$\mathcal{L}^2(\Omega)$
$\epsilon_0\overline{\overline{\epsilon}}_r,\mu_0\overline{\overline{\mu}}_r$	$\mathcal{H}(\mathrm{curl},\Omega)\longrightarrow\mathcal{H}(\mathrm{div},\Omega)$

Table 2.1: Electromagnetic quantities and their function space.

2.3.2.5 Scalar and rotational basis functions

The basis functions chosen to expand the $\mathcal{H}^1(\Omega)$ space, especially tailored to expand scalar functions, are based on the simplex coordinates ϕ_i [101]. ϕ_i is the continuous function that is linear on each triangle or tetrahedron, being one at node i and zero at all other nodes.

Each basis function is associated with either a node $\{i\}$, an edge $\{ij\}$, a triangular face $\{ijk\}$ or a tetrahedron $\{ijkl\}$ of the mesh.

The continuous, scalar ($\mathcal{H}^1(\Omega)$-conforming) finite element spaces of order p are given by $\mathcal{V}^p = \mathcal{S}^1 \oplus \ldots \mathcal{S}^p$, where $\mathcal{S}^p \subset \mathcal{H}^1(\Omega)$ are given in table 2.2. We note that the functions in $\mathcal{V}^p$ are continuous across element boundaries.

Space	Basis functions	Mesh entity
$\mathcal{S}^1$	ϕ_i	$\{i\}$
$\mathcal{S}^2$	$\phi_i\phi_j$	$\{ij\}$
$\mathcal{S}^3$	$\phi_i\phi_j(\phi_i-\phi_j)$	$\{ij\}$
	$\phi_i\phi_j\phi_k$	$\{ijk\}$

Table 2.2: $\mathcal{H}^1(\Omega)$-conforming basis functions up to order $p = 3$.

For the rotational basis functions, we have chosen to expand the $\mathcal{H}(\text{curl}, \Omega)$ with Nédélec incomplete order spaces [102] which often lead to sparser matrices than the complete order counterpart while achieving approximately the same accuracy. They also permit the use of different elemental orders in a single finite element iterative solution with p-multilevel preconditioners. The $\mathcal{H}(\text{curl}, \Omega)$-conforming finite element space of order p is hence constructed recursively,

$$\mathcal{W}^p = \mathcal{W}^{p-1} \oplus \bar{\mathcal{W}}^p \text{ for } p = 2, 3 \text{ and } \mathcal{W}^1 = \mathcal{R}^1,$$

with the incremental space $\bar{\mathcal{W}}^p = \mathcal{R}^p \oplus \nabla\mathcal{S}^p$. The tangential components of $\mathcal{W}^p$ are continuous across element boundaries whereas the normal component may be discontinuous.

Space	Basis functions	Mesh entity
$\mathcal{R}^1$	$\phi_i\nabla\phi_j - \phi_j\nabla\phi_j$	$\{ij\}$
$\mathcal{R}^2$	$3\phi_j\phi_k\nabla\phi_i - \nabla(\phi_i\phi_j\phi_k)$	$\{ijk\}$
	$3\phi_k\phi_i\nabla\phi_j - \nabla(\phi_i\phi_j\phi_k)$	$\{ijk\}$
$\mathcal{R}^3$	$4\phi_j\phi_k(\phi_j-\phi_k)\nabla\phi_i - \nabla\left(\phi_i\phi_j\phi_k(\phi_j-\phi_k)\right)$	$\{ijk\}$
	$4\phi_k\phi_i(\phi_k-\phi_i)\nabla\phi_j - \nabla\left(\phi_i\phi_j\phi_k(\phi_k-\phi_i)\right)$	$\{ijk\}$
	$4\phi_i\phi_j(\phi_i-\phi_j)\nabla\phi_k - \nabla\left(\phi_i\phi_j\phi_k(\phi_i-\phi_j)\right)$	$\{ijk\}$
	$4\phi_j\phi_k\phi_l\nabla\phi_i - \nabla(\phi_i\phi_j\phi_k\phi_l)$	$\{ijkl\}$
	$4\phi_k\phi_l\phi_i\nabla\phi_j - \nabla(\phi_i\phi_j\phi_k\phi_l)$	$\{ijkl\}$
	$4\phi_l\phi_i\phi_j\nabla\phi_k - \nabla(\phi_i\phi_j\phi_k\phi_l)$	$\{ijkl\}$

Table 2.3: $\mathcal{H}(\text{curl}, \Omega)$-conforming basis functions up to order $p = 3$.

2.3.3 Galerkin framework

Among the finite element formulations, the Galerkin approach is the most straightforward to achieve finite element matrices. While the Rayleigh-Ritz approach re-

quires to derive the proper Hamiltonian that describes the physics of the problem, minimizing it, the Galerkin approach simply requires to define projections, which may be intrinsic from the definition of the shape functions in a Hilbert space. In fact, in a Hilbert space, the projection from a space to another is given by the Lebesgue scalar product

$$< \mathbf{u}, \mathbf{v} >= \int_{\Omega} \mathbf{u}^{*}\mathbf{v}\, d\Omega,$$

where * implies the adjoint operator (hermitian transpose). Furthermore, the original Galerkin projection is such that the space of origin $\mathcal{V}$ is the same of the arrival space $\mathcal{V}$.

Consider the linear operator $A : \mathcal{V} \longrightarrow \mathcal{V}$, the corresponding homogeneous system is

$$A\mathbf{v} = \mathbf{f},$$

where $\mathbf{v} \in \mathcal{V}$ and $\mathbf{f} \in \mathcal{V}$. With the Galerkin approach, we seek $\mathbf{v} \in \mathcal{V}$ such that

$$< \mathbf{t}, A\mathbf{v} >=< \mathbf{t}, \mathbf{f} >, \quad \forall \mathbf{t} \in \mathcal{V}.$$

Let us also assume the N-dimensional space $\mathcal{V}_h \in \mathcal{V}$ described by shape functions $\mathbf{v}_j$ such that $\mathbf{v}_h = \sum_{j=1}^{N} x_j \mathbf{v}_j$ and $\mathbf{t}_h = \text{span}\{\mathbf{v}_1, \ldots, \mathbf{v}_i, \ldots, \mathbf{v}_n\}$. If we seek $\mathbf{v}_h \in \mathcal{V}_h$ such that

$$\sum_{i=1}^{N} x_j < \mathbf{v}_i, A\mathbf{v}_j >=< \mathbf{v}_i, \mathbf{f} >, \quad \forall \mathbf{v}_i, \quad i = 1, \ldots, N, \tag{2.3.1}$$

and, by Cae's theorem, $\mathbf{v}_h$ exists and is unique. The system (2.3.1) can be turned into an N-dimensional set of linear equations whose solution is found by solving the $(N \times N)$-matrix system

$$[A]\ [x] = [b].$$

The matrix entries $\mathrm{A}_{ij} =< \mathbf{v}_i, A\mathbf{v}_j >$, the source vector entries are $\mathrm{b}_i =< \mathbf{v}_i, \mathbf{f} >$ and the unknown $[x]$ contains the expansion coefficients x_j for the solution $\mathbf{v} \approx \mathbf{v}_h = \sum_{j=1}^{N} x_j \mathbf{v}_j$.

2.3.3.1 Problem model

Let us consider the domain $\Omega \subset \mathbb{R}^3$ to be bounded by $\partial\Omega = \Gamma = \Gamma_{\mathrm{E}} \cup \Gamma_{\mathrm{H}} \cup \Gamma_{\mathrm{WG}} \cup \Gamma_{\mathrm{R}}$ in the antenna problem and by $\partial\Omega = \Gamma = \Gamma_{\mathrm{E}} \cup \Gamma_{\mathrm{H}} \cup \Gamma_{\mathrm{R}}$ in the scattering probem as depicted in figure 2.3.

Γ_E corresponds to Dirichlet boundary conditions, Γ_H to Neumann boundary conditions, Γ_{WG} to mode matching boundary condition at waveguides ports, and Γ_R corresponds to Robin boundary conditions. The later, also known as *impedance* or *radiation* boundary boundary, allow to mimic open problems. The antenna problem can be straightforwardly reduced to a waveguide device problem upon neglecting the radiation boundaries.

Consider now the discretized domain $\Omega_h = \bigcup_{n=1}^{N} \Omega_n \subset \Omega$, where the subdomains Ω_n (triangles or tetrahedra of the mesh) are such that $\Omega_n \cap \Omega_m = \{\emptyset\}$ for $n \neq m$. Ω_h is

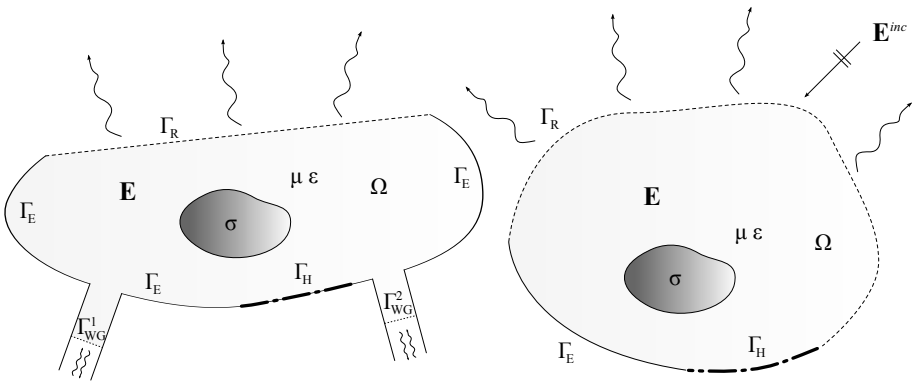

Figure 2.3: Finite element domains for the antenna and the scattering problems.

parameterized in by the maximum dimension h of the subdomains Ω_n, and we shall assume that as $h \to 0$, $\Omega_h \to \Omega$ (the mesh is said to be conforming to the CAD model).

With $\hat{\mathbf{n}}$ pointing outwardly from Ω, consider space $\mathcal{W} = \mathcal{W}(\Omega_h) \subset \mathcal{H}(\text{curl}, \Omega)$ of the curl-conforming shape functions $\mathbf{w}$, defined by the direct sum of two closed subspaces as follows

$$\begin{aligned} \mathcal{W} &= \mathcal{W}_D \oplus \mathcal{W}_E, \\ \mathcal{W}_D &:= \{\mathbf{w} \in \mathcal{W} \mid \hat{\mathbf{n}} \times \mathbf{w} \neq 0 \text{ on } \Gamma_E\} \subset \mathcal{H}(\text{curl}, \Omega), \\ \mathcal{W}_E &:= \{\mathbf{w} \in \mathcal{W} \mid \hat{\mathbf{n}} \times \mathbf{w} = 0 \text{ on } \Gamma_E\} \subset \mathcal{H}(\text{curl}, \Omega, \Gamma_E). \end{aligned}$$

$\mathcal{W}_D$ is in fact the subspace for the imposition of Dirichlet conditions. The total electric field is given by the approximating finite summations

$$\begin{aligned} \mathbf{E} &= \mathbf{E}_E + \mathbf{E}_D, \\ \mathbf{E}_E &:= \sum_{j=1}^{N} x_j \mathbf{w}_j, \qquad \mathbf{w}_j \in \mathcal{W}_E, \\ \mathbf{E}_D &:= \sum_{d=1}^{N^D} x_d \mathbf{w}_d, \qquad \mathbf{w}_d \in \mathcal{W}_D. \end{aligned}$$

The PDE we must solve to retrieve the fields is (2.2.4), reported here for convenience

$$\nabla \times \frac{1}{\mu_r} \nabla \times \mathbf{E} + jk_0\zeta_0\sigma\mathbf{E} - k_0^2\epsilon_r\mathbf{E} = 0,$$

and the boundary conditions can be stated as

$$\hat{\mathbf{n}} \times (\mathbf{E} \times \hat{\mathbf{n}}) = \bar{\mathbf{E}}_t, \qquad \text{on } \Gamma_E, \tag{2.3.2}$$

$$\hat{\mathbf{n}} \times (\mathbf{H} \times \hat{\mathbf{n}}) = \bar{\mathbf{H}}_t, \qquad \text{on } \Gamma_H, \tag{2.3.3}$$

$$\hat{\mathbf{n}} \times (\mathbf{E} \times \hat{\mathbf{n}}) = Z_s \mathbf{H} \times \hat{\mathbf{n}}, \qquad \text{on } \Gamma_R. \tag{2.3.4}$$

$\bar{\mathbf{E}}_t$ and $\bar{\mathbf{H}}_t$ are known electric field and magnetic field distributions. Z_s is the wave impedance at the radiation boundary to mimic the Sommerfeld radiation condition

$$\lim_{r \to \infty} r\left((\nabla \times \mathbf{E}) \times \hat{\mathbf{n}} + jk\mathbf{E}\right) = 0,$$

and hence is chosen as $Z_s = \zeta_0\sqrt{\frac{\mu_r}{\epsilon_r}}$ on Γ_R. One consideration must be done on the condition (2.3.4). In fact, that condition impose total absorbing condition on Γ_R only for waves impinging perpendicularly to the surface, and the absorbing condition behaves poorly as waves come with a different incident angle. This is why it is typically recommended to put these boundaries at least $\frac{\lambda}{4}$ away form the radiators in order to reduce the internal reflections that may appear. Other methods have been employed to reduce this effect, such as increasing the order of the absorbing boundary condition [103] or, in a more rigorous way, employ boundary integral equations [104] to totally absorb the fields from any incident angle.

We proceed with the Galerkin projections, testing with $\mathbf{w}_i \in \mathcal{W}_E$

$$\int_\Omega \mathbf{w}_i^* \cdot \left(\nabla \times \frac{1}{\mu_r} \nabla \times \mathbf{E} + jk_0\zeta_0\sigma\mathbf{E} - k_0^2\epsilon_r\mathbf{E} \right) d\Omega = 0.$$

We integrate by parts the first term

$$\int_\Omega \mathbf{w}_i^* \cdot \nabla \times \frac{1}{\mu_r} \nabla \times \mathbf{E}\, d\Omega = \int_\Omega \nabla \times \mathbf{w}_i^* \cdot \frac{1}{\mu_r} \nabla \times \mathbf{E}\, d\Omega - \int_\Gamma \mathbf{w}_i^* \times \frac{1}{\mu_r} \nabla \times \mathbf{E} \cdot \hat{\mathbf{n}}\, d\Gamma, \quad (2.3.5)$$

and use of Faraday's law for the last right-hand side term

$$-\int_\Gamma \mathbf{w}_i^* \times \frac{1}{\mu_r} \nabla \times \mathbf{E} \cdot \hat{\mathbf{n}}\, d\Gamma = jk_0\zeta_0 \int_\Gamma \mathbf{w}_i^* \times \mathbf{H} \cdot \hat{\mathbf{n}}\, d\Gamma.$$

Evaluating the integrals on boundaries separately, we have

$$\begin{aligned} jk_0\zeta_0 \int_\Gamma \mathbf{w}_i^* \times \mathbf{H} \cdot \hat{\mathbf{n}}\, d\Gamma &= jk_0\zeta_0 \int_{\Gamma_E} \hat{\mathbf{n}} \times \mathbf{w}_i^* \cdot \mathbf{H}\, d\Gamma + \\ &\quad jk_0\zeta_0 \int_{\Gamma_H} \mathbf{w}_i^* \times \mathbf{H} \cdot \hat{\mathbf{n}}\, d\Gamma + \\ &\quad jk_0\zeta_0 \int_{\Gamma_R} \mathbf{w}_i^* \times \mathbf{H} \cdot \hat{\mathbf{n}}\, d\Gamma, \end{aligned} \quad (2.3.6)$$

where we have used the vector identities $\mathbf{A} \times \mathbf{B} \cdot \mathbf{C} = \mathbf{B} \times \mathbf{C} \cdot \mathbf{A} = \mathbf{C} \times \mathbf{A} \cdot \mathbf{B}$ for the first right-hand side integral, which results to be null as the testing functions are null on Γ_E. The magnetic field on Γ_H can be decomposed as

$$\mathbf{H} = \bar{\mathbf{H}}_t + H_n \hat{\mathbf{n}}$$

hence the integral on Γ_H can be reduced to

$$jk_0\zeta_0 \int_{\Gamma_H} \mathbf{w}_i^* \times \mathbf{H} \cdot \hat{\mathbf{n}}\, d\Gamma = -jk_0\zeta_0 \int_{\Gamma_H} \mathbf{w}_i^* \cdot \hat{\mathbf{n}} \times \bar{\mathbf{H}}_t\, d\Gamma.$$

The previous vector identity can be used, in conjunction with the radiation boundary condition, to recast the integral on Γ_R as

$$\begin{aligned} jk_0\zeta_0 \int_{\Gamma_R} \mathbf{w}_i^* \times \mathbf{H} \cdot \hat{\mathbf{n}}\, d\Gamma &= jk_0\zeta_0 \int_{\Gamma_R} \frac{1}{Z_s} \hat{\mathbf{n}} \times (\mathbf{E} \times \hat{\mathbf{n}}) \cdot \mathbf{w}_i^*\, d\Gamma \\ &= jk_0\zeta_0 \int_{\Gamma_R} \hat{\mathbf{n}} \times \mathbf{w}_i^* \cdot \frac{1}{Z_s} \hat{\mathbf{n}} \times \mathbf{E}\, d\Gamma \end{aligned}$$

We finally obtain the following weak form

$$\int_\Omega \nabla\times\mathbf{w}_i^*\cdot\frac{1}{\mu_r}\nabla\times\mathbf{E}\,d\Omega + jk_0\zeta_0\int_\Omega \mathbf{w}_i^*\cdot\sigma\mathbf{E}\,d\Omega + jk_0\zeta_0\int_{\Gamma_R}\hat{\mathbf{n}}\times\mathbf{w}_i^*\cdot\frac{1}{Z_s}\hat{\mathbf{n}}\times\mathbf{E}\,d\Gamma -$$
$$k_0^2\int_\Omega \mathbf{w}_i^*\cdot\epsilon_r\mathbf{E}\,d\Omega = jk_0\zeta_0\int_{\Gamma_H}\mathbf{w}_i^*\cdot\hat{\mathbf{n}}\times\bar{\mathbf{H}}_t\,d\Gamma - \int_\Omega\nabla\times\mathbf{w}_i^*\cdot\frac{1}{\mu_r}\nabla\times\mathbf{E}_D\,d\Omega -$$
$$jk_0\zeta_0\int_\Omega\mathbf{w}_i^*\cdot\sigma\mathbf{E}_D\,d\Omega + k_0^2\int_\Omega\mathbf{w}_i^*\cdot\epsilon_r\mathbf{E}_D\,d\Omega, \qquad \forall\mathbf{w}_i\in\mathcal{W}_E. \quad (2.3.7)$$

In practical microwave applications, the Dirichlet boundary condition is generally associated to perfect electric conductors where we have $\bar{\mathbf{E}}_t = 0$ ($\mathbf{E}_D = 0$) while the Neumann boundary condition corresponds to perfect magnetic conductors with $\bar{\mathbf{H}}_t = 0$. This implies the right-hand side of (2.3.7) vanishes. Thus, the source vector must be supplied by either waveports modal field distributions on Γ_{WG}, for the antenna or the waveguide device, or the impinging external field on Γ_R, for the scattering problem.

2.3.3.2 Waveports boundary conditions

In order to supply excitation on Γ_{WG} two approaches can be employed: the radiation conditions on ports or the transfinite element method. The first is somehow less accurate than the second one, but less computationally involving and easy to implement.

Dominant mode continuity

This approach limits the analysis in Ω to the accuracy provided by considering only the dominant modes to be incident on Γ_{WG} and somehow considering an equivalent radiation condition to absorb the back-scattered field. It is mandatory, for accurate modeling of the problems, that the boundaries are put sufficiently far form any discontinuity, such that any back-scattered higher order mode, evanescent in the waveguide, has vanished (several orders of magnitude lower than the dominant mode) once back at the boundary.

On Γ_{WG}, if we consider the wave ports to be fed only by a k^{th} dominant mode (lowest cut-off frequency), the following relation holds for the port [39, 101]

$$\hat{\mathbf{n}}\times\mathbf{H}_t^k = \frac{1}{Z_k}\hat{\mathbf{n}}\times\hat{\mathbf{n}}\times\mathbf{E}_t^k - \frac{2}{Z_k}\hat{\mathbf{n}}\times\hat{\mathbf{n}}\times\mathbf{E}_t^{k\ inc}, \qquad \text{on } \Gamma_{WG}^k, \quad (2.3.8)$$

where $\mathbf{E}_t^{k\ inc}$ is the incident electric field and Z_k the modal impedance. By analogy

with the previous formulation for Γ_H (2.3.6), (2.3.7) becomes

$$\begin{aligned}\int_\Omega \nabla\times\mathbf{w}_i^*\cdot\frac{1}{\mu_r}\nabla\times\mathbf{E}\,d\Omega + jk_0\zeta_0\int_\Omega \mathbf{w}_i^*\cdot\sigma\mathbf{E}\,d\Omega\ -\\ k_0^2\int_\Omega \mathbf{w}_i^*\cdot\epsilon_r\mathbf{E}\,d\Omega + jk_0\zeta_0\int_{\Gamma_R}\hat{\mathbf{n}}\times\mathbf{w}_i^*\cdot\frac{1}{Z_s}\hat{\mathbf{n}}\times\mathbf{E}\,d\Gamma +\\ jk_0\zeta_0\sum_{m=1}^{N^M}\int_{\Gamma_{WG}^m}\hat{\mathbf{n}}\times\mathbf{w}_i^*\cdot\frac{1}{Z_m}\hat{\mathbf{n}}\times\mathbf{E}_t^m\,d\Gamma\\ = j2k_0\zeta_0\int_{\Gamma_{WG}^k}\hat{\mathbf{n}}\times\mathbf{w}_i^*\cdot\frac{1}{Z_k}\hat{\mathbf{n}}\times\mathbf{E}_t^{k\ inc}\,d\Gamma,\qquad\forall\mathbf{w}_i\in\mathcal{W}_E\end{aligned}\tag{2.3.9}$$

where N^M is the total number of modes and $k=1,\ldots,N^M$. Each of the N^M modes, or a combination of them, can be used as excitation, leading to a non-null right-hand side in the finite element system. Notice that the modal field distributions $\mathbf{E}_t^m$ and relative impedance can be supplied either analytically or computed with a 2D eigenvalue problem (see below the transverse-longitudinal field formulation). The resulting system is

$$[A]\,[x] \;=\; [b],\tag{2.3.10}$$

where $[A]\in\mathbb{C}^{N\times N}$, $[x]$ and $[b]\in\mathbb{C}^N$ with N the number of unknowns equal to the number of shape functions $\mathbf{w}_j\in\mathcal{W}_E$. If materials within Ω are isotropic, then $[A]$ is symmetric positive definite, enabling the use of memory-efficient solvers.

To retrieve scattering coefficients, one must compute, in the postprocessing phase, the following testings

$$S_{mk}=\frac{1}{2}\int_{\Gamma_{WG}^m}\mathbf{E}^*\cdot\frac{1}{Z_m}\mathbf{E}_t^{m\ inc}\,d\Gamma-\delta_{mk},\qquad m=1,\ldots,N^M,$$

where δ_{mk} is Kronecker's delta.

Transfinite element method

The transfinite element method is more accurate in the way that better orthogonality between modes is enforced. On Γ_{WG}, the tangential electric and magnetic fields can be expanded as

$$\mathbf{E}_t \;=\; \hat{\mathbf{n}}\times(\mathbf{E}\times\hat{\mathbf{n}}) \;=\; \sum_k\left(a_k^r+a_k^i\right)\mathbf{E}_t^k,\qquad\text{on }\Gamma_{WG},\tag{2.3.11}$$

$$\mathbf{H}_t \;=\; \hat{\mathbf{n}}\times(\mathbf{H}\times\hat{\mathbf{n}}) \;=\; \sum_k\left(a_k^r-a_k^i\right)\mathbf{H}_t^k,\qquad\text{on }\Gamma_{WG},\tag{2.3.12}$$

where a_k^i, a_k^r the k^{th} complex modal incident and reflected amplitudes. The first step of the transfinite element method is to collect the shape functions defined in Ω apart from the ones defined on Γ_{WG} such that

$$\mathcal{W}_I \;:=\; \{\mathbf{w}\in\mathcal{W}\mid\hat{\mathbf{n}}\times\mathbf{w}=0\text{ on }\Gamma_{WG}\},\tag{2.3.13}$$

$$\mathcal{W}_{WG} \;:=\; \{\mathbf{w}\in\mathcal{W}\mid\hat{\mathbf{n}}\times\mathbf{w}\neq 0\text{ on }\Gamma_{WG}\}.\tag{2.3.14}$$

Hence, the k^{th} mode on Γ_{WG} can be expanded in terms of shape functions such that

$$\mathbf{E}_t^k = \sum_{i=1}^{N_{WG}^k} m_i^k \mathbf{w}_i, \qquad \mathbf{w}_i \in \mathcal{W}_{WG}. \tag{2.3.15}$$

Let us suppose the coefficients m_i^k to be known. Considering one mode impinging on the waveports at a time, the electric field in Ω can be decomposed in the sum

$$\mathbf{E} = \sum_{j=1}^{N-N_{WG}} x_j \mathbf{w}_j + \sum_{m=1}^{N_M} a_m^r \mathbf{E}_t^m + a_k^i \mathbf{E}_t^k, \quad \mathbf{w}_j \in \mathcal{W}_I, \tag{2.3.16}$$

while the tangential magnetic field on Γ_{WG} becomes

$$\mathbf{H}_t = \sum_{m=1}^{N_M} a_m^r \mathbf{H}_t^m - a_k^i \mathbf{H}_t^k. \tag{2.3.17}$$

N_m is the total number of modes retained in modal expansion and $N_{WG} = \sum_{k=1}^{N_M} N_{WG}^k$ is the total number of shape functions pertaining to $\mathcal{W}_{WG}$. The accuracy of the formulation is due to fact the incident mode is absorbed in the modal summation, letting $a_k^r \leftarrow a_k^r + a_k^i$. It follows that

$$\mathbf{E} = \sum_{j=1}^{N-N_{WG}} x_j \mathbf{w}_j + \sum_{m=1}^{N_M} a_m^r \mathbf{E}_t^m, \tag{2.3.18}$$

and

$$\mathbf{H}_t = \sum_{m=1}^{N_M} a_m^r \mathbf{H}_t^m - 2a_k^i \mathbf{H}_t^k. \tag{2.3.19}$$

Again, by analogy with (2.3.6), the following weak form is optained [39]

$$\begin{aligned}
&\int_\Omega \nabla \times \mathbf{w}_i^* \cdot \frac{1}{\mu_r} \nabla \times \left(\sum_{j=1}^{N-N_{WG}} x_j \mathbf{w}_j + \sum_{m=1}^{N_M} a_m^r \mathbf{E}_t^m \right) d\Omega + \\
&\qquad jk_0\zeta_0 \int_\Omega \mathbf{w}_i^* \cdot \sigma \left(\sum_{j=1}^{N-N_{WG}} x_j \mathbf{w}_j + \sum_{m=1}^{N_M} a_m^r \mathbf{E}_t^m \right) d\Omega + \\
&\qquad jk_0\zeta_0 \int_{\Gamma_R} \hat{\mathbf{n}} \times \mathbf{w}_i^* \cdot \frac{1}{Z_s} \hat{\mathbf{n}} \times \left(\sum_{j=1}^{N-N_{WG}} x_j \mathbf{w}_j + \sum_{m=1}^{N_M} a_m^r \mathbf{E}_t^m \right) d\Gamma - \\
&\qquad k_0^2 \int_\Omega \mathbf{w}_i^* \cdot \epsilon_r \left(\sum_{j=1}^{N-N_{WG}} x_j \mathbf{w}_j + \sum_{m=1}^{N_M} a_m^r \mathbf{E}_t^m \right) d\Omega = \\
&jk_0\zeta_0 \int_{\Gamma_{WG}} \mathbf{w}_i^* \cdot \hat{\mathbf{n}} \times \left(\sum_{m=1}^{N_M} a_m^r \mathbf{H}_t^m - 2a_k^i \mathbf{H}_t^k \right) d\Gamma, \qquad \forall \mathbf{w}_i \in \mathcal{W}_I \cap \mathcal{W}_E,
\end{aligned} \tag{2.3.20}$$

having considered Γ_E to be on perfect electric conductor and Γ_H on perfect magnetic conductor. Since the testing shape functions $\mathbf{w}_i$ have been excluded from $\mathcal{W}_{WG}$, the right-hand side integral vanishes and the resulting system of equations is given by

$$[P][x_{WG}] + [A][x_I] = [0], \tag{2.3.21}$$

where $[x_{WG}]$ is a vector corresponding to reflected modal amplitudes on Γ_{WG} and $[x_I]$ is the unknown vector corresponding to the shape functions internal to Ω/Γ_{WG}.

At this point, no excitation is provided yet. We need to supply further testings with the modal expansions (2.3.15), such that

$$\begin{aligned}\int_\Omega \nabla\times\mathbf{E}_t^{i*}\cdot\frac{1}{\mu_r}\nabla\times\left(\sum_{j=1}^{N-N_{WG}} x_j\mathbf{w}_j+\sum_{m=1}^{N_M} a_m^r\mathbf{E}_t^m\right)d\Omega+\\ jk_0\zeta_0\int_\Omega \mathbf{E}_t^{i*}\cdot\sigma\left(\sum_{j=1}^{N-N_{WG}} x_j\mathbf{w}_j+\sum_{m=1}^{N_M} a_m^r\mathbf{E}_t^m\right)d\Omega+\\ jk_0\zeta_0\int_{\Gamma_R}\hat{\mathbf{n}}\times\mathbf{E}_t^{i*}\cdot\frac{1}{Z_s}\hat{\mathbf{n}}\times\left(\sum_{j=1}^{N-N_{WG}} x_j\mathbf{w}_j+\sum_{m=1}^{N_M} a_m^r\mathbf{E}_t^m\right)d\Gamma-\\ k_0^2\int_\Omega \mathbf{E}_t^{i*}\cdot\epsilon_r\left(\sum_{j=1}^{N-N_{WG}} x_j\mathbf{w}_j+\sum_{m=1}^{N_M} a_m^r\mathbf{E}_t^m\right)d\Omega\ =\\ jk_0\zeta_0\int_{\Gamma_{WG}}\mathbf{E}_t^{i*}\cdot\hat{\mathbf{n}}\times\left(\sum_{m=1}^{N_M} a_m^r\mathbf{H}_t^m-2a_k^i\mathbf{H}_t^k\right)d\Gamma,\qquad i=1,\dots,N_m.\end{aligned}\tag{2.3.22}$$

Now the integrals with $\mathbf{w}_j$ vanish, as their subspace is orthogonal to the subspace of the testing functions $\mathbf{E}_t^i$, that is $\mathcal{W}_I\perp\mathcal{W}_{WG}$. The right-hand side can be also written as

$$\begin{aligned}jk_0\zeta_0\int_{\Gamma_{WG}}\mathbf{E}_t^{i*}\cdot\hat{\mathbf{n}}\times\left(\sum_{m=1}^{N_M} a_m^r\mathbf{H}_t^m-2a_k^i\mathbf{H}_t^k\right)d\Gamma=\\ -jk_0\zeta_0\int_{\Gamma_{WG}}\mathbf{E}_t^{i*}\times\sum_{m=1}^{N_M} a_m^r\mathbf{H}_t^m\cdot\hat{\mathbf{n}}\,d\Gamma+\\ j2k_0\zeta_0\int_{\Gamma_{WG}}\mathbf{E}_t^{i*}\times a_k^i\mathbf{H}_t^k\cdot\hat{\mathbf{n}}\,d\Gamma\end{aligned}\tag{2.3.23}$$

By the use of orthonormal identity of the transverse modes

$$\int_{\Gamma_{WG}^p}\mathbf{E}_t^{p*}\times\mathbf{H}_t^q\cdot\hat{\mathbf{n}}\,d\Gamma=\delta_{pq}\quad[\mathrm{W}]\tag{2.3.24}$$

the follow system of equations is obtained

$$[R+jk_0\zeta_0 I][x_{WG}]+[P]^T[x_I]=[f],\tag{2.3.25}$$

where $[R]$ is the matrix obtained by testing on ports, $[I]$ is the identity matrix, and $[f]$ is the column vector with non-null entry $j2k_0\zeta_0 a_k^i$ corresponding to the non-null incident modal amplitude. $(\cdot)^T$ is the transposition operator. a_k^i is usually chosen to be 1 (corresponding to 1 [W] of impinging power) in order to retrieve scattering parameters. Furthermore, multiple righ-hand sides can be used to enforce all the modes, one at a time, without need to modify the system matrices. For instance

$$[f]=j2k_0\zeta_0[I].$$

The full system can finally be cast as

$$\begin{bmatrix} R + jk_0\zeta_0 I & P^T \\ P & A \end{bmatrix} \begin{bmatrix} x_{WG} \\ x_I \end{bmatrix} = \begin{bmatrix} j2k_0\zeta_0 I \\ 0 \end{bmatrix}, \tag{2.3.26}$$

where $x_I = \left[x_1, \ldots, x_{N-N_{WG}}\right]^T$ are the unknowns internal to $\Omega/\{\Gamma_{WG} \cup \Gamma_E \cup \Gamma_H\}$, and $x_{WG} = \left[a^r_1, \ldots, a^r_{N_m}\right]^T$ the complex-valued modal amplitudes for each mode.

Recalling the previously imposed absorbing condition for impinging mode, stated as (1 [W] of impinging power) $a^r_m \leftarrow a^r_m + \delta_{mk}$, the scattering parameters can be straightforwardly computed as

$$S_{mk} = a^r_m - \delta_{mk}, \qquad m = 1, \ldots, N^M.$$

To compute the fields for a different impinging power, one might simply scale of the desired amount, $c = \sqrt{P^{inc}}$ with P^{inc} the incident power, both $a^i_k \leftarrow c a^i_k$ and $a^r_k \leftarrow c(a^r_k + a^i_k)$. The power balance of the formulation is such that the scattering parameters remain the same.

A simple manner to assemble (2.3.26) is first to collect all the finite element coefficients pertaining to Ω apart from those on Γ_{WG} such that

$$\begin{bmatrix} A_{WG,WG} & A_{WG,I} \\ A_{I,WG} & A_{I,I} \end{bmatrix}. \tag{2.3.27}$$

Then, the expansion coefficients (2.3.15) of each mode, which can be viewed as column vectors

$$[m_k] = \left[m^k_1, \ldots, m_{N^k_{WG}}\right]^T,$$

and can be collected in a matrix

$$[M] = \left[[m_1], \ldots, \left[m_{N_M}\right]\right] \in \mathbb{C}^{N_{WG} \times N_M}.$$

The system matrix (2.3.26) is finally obtained by computing

$$\begin{bmatrix} M^T A_{WG,WG} M + jk_0\zeta_0 I & M^T A_{WG,I} \\ A_{I,WG} M & A_{I,I} \end{bmatrix} \begin{bmatrix} x_{WG} \\ x_I \end{bmatrix} = \begin{bmatrix} j2k_0\zeta_0 I \\ 0 \end{bmatrix}. \tag{2.3.28}$$

It is evident that (2.3.28) can be complex valued (due to waveports and radiation boundaries or material losses in terms of non null conductivity or complex permittivity and permeability), but a key point is the symmetry, if the same assumption of isotropic materials is stands, which enables the use of memory-efficient matrix solvers.

Transverse-longitudinal field formulation

The impinging modal field distributions in both dominant mode and transfinite element methods can be supplied by an analytical approach, when the geometry of Γ_{WG} is rather simple and an expansion is already available. When the geometry gets

complicated or the contour boundaries are not simply perfect electric or magnetic, computations becomes much more involving. Also, non homogeneous materials lead to difficult modal distributions computations.

A versatile way to compute the mode amplitudes is to solve an eigenvalue problem by the use of the finite element method, allowing thus to manage arbitrary geometries with arbitrary materials and boundary conditions. In the following, the transverse-longitudinal field formulation will be presented to compute the transverse fields used for waveports excitations.

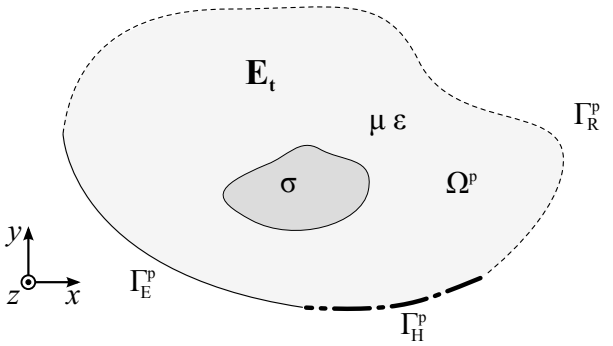

Figure 2.4: Finite element domain for the waveport eigenvalue problem.

The electric field distribution $\mathbf{E}$ (at port p on Γ_{WG}) is computed numerically by solving a 2-D[5] eigenvalue problem on $\Omega \equiv \Gamma_{WG}^p \in \mathbb{R}^2$ (Fig. 2.4) using transverse-longitudinal field formulation [39]. First, the electric field is expressed as the sum of transverse and longitudinal parts

$$\mathbf{E} = [\mathbf{E}_t(x,y) + \hat{\mathbf{z}}\, E_z(x,y)]\, \mathrm{e}^{-\gamma z} \quad \text{on } \Omega, \tag{2.3.29}$$

with $\hat{\mathbf{z}} = -\hat{\mathbf{n}}|_p$ and γ is the propagation constant. After the definition of the vector basis functions $\mathbf{v} = \hat{\mathbf{n}} \times \mathbf{w} \in \mathcal{H}(\mathrm{curl}, \Omega^p, \Gamma_E)$ with $\mathbf{w} \in \mathcal{W}_{WG} \cap \mathcal{W}_E$ such that $\mathbf{E}_t = \sum_{j=1}^{N_t} x_{t,j}\mathbf{v}_j$ and the scalar basis functions $\phi \in \mathcal{H}^1(\Omega^p, \Gamma_E)$ such that $E_z = \sum_{j=1}^{N_z} x_{z,j}\phi_j$, a Galerkin projection is applied to the eigenvalue problem with isotropic materials governed by

$$\nabla \times \frac{1}{\mu_r} \nabla \times \mathbf{E} - k_0^2 \epsilon_r \mathbf{E} = 0, \tag{2.3.30}$$

with $\epsilon_r \leftarrow \epsilon_r + \sigma / j\omega_0\epsilon_0$, leading to the following generalized eigenvalue system of $N_t + N_z$ equations [39, 105]

$$\begin{bmatrix} A_{tt} & 0 \\ 0 & 0 \end{bmatrix} \begin{bmatrix} \gamma x_t \\ x_z \end{bmatrix} = \gamma^2 \begin{bmatrix} B_{tt} & B_{tz} \\ B_{zt} & B_{zz} \end{bmatrix} \begin{bmatrix} \gamma x_t \\ x_z \end{bmatrix}, \tag{2.3.31}$$

[5] Similar considerations can be done for $\Omega \equiv \Gamma_{WG}^p \in \mathbb{R}$ to compute excitations in FES-2D.

where the matrices entries are given by

$$
\begin{aligned}
A_{tt,ij} = & \int_{\Omega_p} \nabla_t \times \mathbf{v}_i \cdot \frac{1}{\mu_r} \nabla_t \times \mathbf{v} \, d\Omega - \\
& k_0^2 \int_{\Omega_p} \mathbf{v}_i \cdot \epsilon_r \mathbf{v}_j \, d\Omega + \\
& jk_0\zeta_0 \int_{\Gamma_R^p} \mathbf{v}_i \cdot \frac{1}{Z_s} \mathbf{v}_j \, d\Gamma, \\
B_{tt,ij} = & \int_{\Omega_p} \mathbf{v}_i \cdot \frac{1}{\mu_r} \mathbf{v}_j \, d\Omega, \\
B_{tz,ij} = & \int_{\Omega_p} \mathbf{v}_i \cdot \frac{1}{\mu_r} \nabla_t \phi_j \, d\Omega, \\
B_{zt,ij} = & \int_{\Omega_p} \nabla_t \phi_i \cdot \frac{1}{\mu_r} \mathbf{v}_j \, d\Omega, \\
B_{zz,ij} = & \int_{\Omega_p} \nabla_t \phi_i \cdot \frac{1}{\mu_r} \nabla_t \phi_j \, d\Omega - \\
& k_0^2 \int_{\Omega_p} \phi_i \epsilon_r \phi_j \, d\Omega + \\
& jk_0\zeta_0 \int_{\Gamma_R^p} \phi_i \frac{1}{Z_s} \phi_j \, d\Gamma.
\end{aligned}
$$

$\nabla_t = \hat{\mathbf{x}} \frac{\partial}{\partial x} + \hat{\mathbf{y}} \frac{\partial}{\partial y}$ is the transverse *del* operator.

The eigenvalue problem (2.3.31), denoted as $[A][x] = \lambda [B][x]$, has $[A]$ and $[B]$ complex symmetric matrices due to the isotropic materials characteristics. The problem can then be solved with a Lanczos-based Krylov subspace solver [106] such as the public domain ARPACK solver [107] in the *shift-invert* mode operation

$$
\begin{aligned}
[A - \tau B]^{-1} [B][x] &= \frac{1}{\lambda - \tau} [x], \\
\tau &= k_0^2 \, \epsilon_{\max} \, \mu_{\max}, \\
\{\epsilon, \mu\}_{\max} &= \max_{(x,y) \in \Omega_p} \Re\mathfrak{e}(\{\epsilon, \mu\}(x,y)).
\end{aligned}
$$

The shift-invert mode expedites the convergence of the employed iterative process when seeking for largest eigenvalues (lowest cut-off frequencies). Furthermore, spurious modes removal is performed by explicit imposition of $[B]$-orthogonality of the Ritz vectors during the iterative process

$$
x_z = -B_{zz}^{-1} B_{zt} \, \gamma x_t.
$$

Then, the k^{th} mode distribution $\mathbf{E}^k$ is normalized such that

$$
\int_{\Omega_p} \mathbf{E}^{k*} \times \mathbf{H}^k \cdot \hat{z} \, d\Omega = 1,
$$

which is achieved upon scaling the unknowns vector such that

$$[x] \longleftarrow \frac{[x]}{\sqrt{[x]^*[B][x]}}.$$

2.3.3.3 Total field scattering

In this section, the total field scattering formulation is presented in order to treat the electromagnetic scattering from incident waves. We recall the formulation (2.3.7) to incorporate the incident field on the radiation boundary Γ_R

$$\int_\Omega \nabla \times \mathbf{w}_i^* \cdot \frac{1}{\mu_r} \nabla \times \mathbf{E}\, d\Omega + jk_0\zeta_0 \int_\Omega \mathbf{w}_i^* \cdot \sigma \mathbf{E}\, d\Omega - k_0^2 \int_\Omega \mathbf{w}_i^* \cdot \epsilon_r \mathbf{E}\, d\Omega = jk_0\zeta_0 \int_{\Gamma_R} \mathbf{w}_i^* \cdot \hat{\mathbf{n}} \times \mathbf{H}\, d\Gamma, \qquad \forall \mathbf{w}_i \in \mathcal{W}_E. \quad (2.3.32)$$

The electric and magnetic fields in Ω can be expressed as the sum of scattered part and an incident part

$$\mathbf{E} = \mathbf{E}^{sc} + \mathbf{E}^{inc}, \qquad \mathbf{H} = \mathbf{H}^{sc} + \mathbf{H}^{inc}$$

Direct substitution in (2.3.4) where the $\mathbf{E} := \mathbf{E}^{sc}$ and $\mathbf{H} := \mathbf{H}^{sc}$ leads to

$$\hat{\mathbf{n}} \times \mathbf{H} = \frac{1}{Z_s}\hat{\mathbf{n}} \times \hat{\mathbf{n}} \times \mathbf{E} + \hat{\mathbf{n}} \times \mathbf{H}^{inc} - \frac{1}{Z_s}\hat{\mathbf{n}} \times \hat{\mathbf{n}} \times \mathbf{E}^{inc}, \qquad \text{on } \Gamma_R. \quad (2.3.33)$$

The first term in right-hand side of (2.3.33) leads to a radiation boundary integral (canonical first order ABC) while the next two terms will enforce the impinging field values on Γ_R. As a result

$$\int_\Omega \nabla \times \mathbf{w}_i^* \cdot \frac{1}{\mu_r} \nabla \times \mathbf{E}\, d\Omega + jk_0\zeta_0 \int_\Omega \mathbf{w}_i^* \cdot \sigma \mathbf{E}\, d\Omega + jk_0\zeta_0 \int_{\Gamma_R} \hat{\mathbf{n}} \times \mathbf{w}_i^* \cdot \frac{1}{Z_s}\hat{\mathbf{n}} \times \mathbf{E}\, d\Gamma - k_0^2 \int_\Omega \mathbf{w}_i^* \cdot \epsilon_r \mathbf{E}\, d\Omega = jk_0\zeta_0 \int_{\Gamma_R} \hat{\mathbf{n}} \times \mathbf{w}_i^* \cdot \left(\frac{1}{Z_s}\hat{\mathbf{n}} \times \mathbf{E}^{inc} - \mathbf{H}^{inc}\right) d\Gamma, \qquad \forall \mathbf{w}_i \in \mathcal{W}_E. \quad (2.3.34)$$

The knowledge of the tangential components of the impinging wave on Γ_R is sufficient to compute the total fields in Ω.

2.3.4 Element matrices and system assembly

Efficient computation [108] of higher-order finite element matrices can be achieved by quadrature integration, and with mappings of the functions from reference elements to the actual element to recover the correct shape functions.

Consider the reference and actual elements of Fig. 2.5. There exist a non degenerate affine mapping $F : K_0 \to K$ from the reference element K_0, defined in simplex

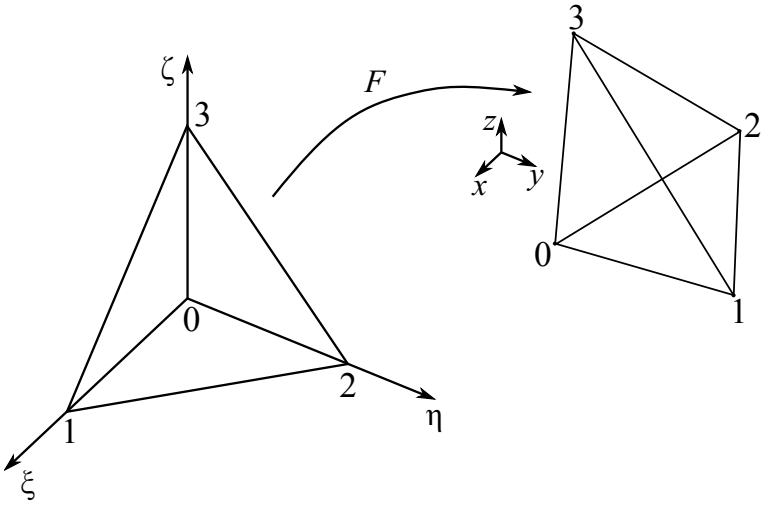

Figure 2.5: Linear mapping F of the reference element to the actual element.

coordinates (ξ,η,ζ) coordinates, the actual element K, defined Cartesian coordinates (x,y,z), defined as

$$\begin{bmatrix} x \\ y \\ z \end{bmatrix} = \begin{bmatrix} x_1-x_0 & x_2-x_0 & x_3-x_0 \\ y_1-y_0 & y_2-y_0 & y_3-y_0 \\ z_1-z_0 & z_2-z_0 & z_3-z_0 \end{bmatrix} \begin{bmatrix} \xi \\ \eta \\ \zeta \end{bmatrix} + \begin{bmatrix} x_0 \\ y_0 \\ z_0 \end{bmatrix}. \tag{2.3.35}$$

The Jacobian matrix $[J]$ of the transformation, defined as

$$\Big[J\Big] = \begin{bmatrix} \frac{\partial x}{\partial \xi} & \frac{\partial y}{\partial \xi} & \frac{\partial z}{\partial \xi} \\ \frac{\partial x}{\partial \eta} & \frac{\partial y}{\partial \eta} & \frac{\partial z}{\partial \eta} \\ \frac{\partial x}{\partial \zeta} & \frac{\partial y}{\partial \zeta} & \frac{\partial z}{\partial \zeta} \end{bmatrix}, \tag{2.3.36}$$

allows for straightforward computation of the partial derivatives of the shape functions: given a scalar function $\phi(\xi,\eta,\zeta)$ on the reference element, its partial derivatives on the actual element can be computed as

$$\begin{bmatrix} \frac{\partial \phi(x,y,z)}{\partial x} \\ \frac{\partial \phi(x,y,z)}{\partial y} \\ \frac{\partial \phi(x,y,z)}{\partial z} \end{bmatrix} = \Big[J\Big]^{-1} \begin{bmatrix} \frac{\partial \phi(\xi,\eta,\zeta)}{\partial \xi} \\ \frac{\partial \phi(\xi,\eta,\zeta)}{\partial \eta} \\ \frac{\partial \phi(\xi,\eta,\zeta)}{\partial \zeta} \end{bmatrix}. \tag{2.3.37}$$

Some of the integrals (the $\mathcal{H}(\mathrm{curl},\Omega)$-conforming *stiffness* matrices) we have seen in the previous formulations involve the curls of the shape functions. They can readily be computed upon employing the vector identities $\nabla\times(\phi\mathbf{A}) = \phi\nabla\times\mathbf{A} + \nabla\phi\times\mathbf{A}$ and $\nabla\times\nabla\phi = 0$ and remembering that the curl operator is linear. The curls of the shape functions of table 2.3 can be recast in functions of the scalar functions and their gradients. Table 2.4 shows their respective curls.

Finally, the reference element with vertices $N_i,\ i = 0,\ldots,3$, in simplex coordi-

Rotational basis ($\mathcal{H}(\text{curl}, \Omega)$)	curl of rotational basis ($\mathcal{H}(\text{div}, \Omega)$)
$\phi_i \nabla \phi_j - \phi_j \nabla \phi_j$	$2(\nabla \phi_i \times \nabla \phi_j)$
$3\phi_j \phi_k \nabla \phi_i - \nabla(\phi_i \phi_j \phi_k)$	$3(\phi_j \nabla \phi_k + \phi_k \nabla \phi_j) \times \nabla \phi_i$
$3\phi_k \phi_i \nabla \phi_j - \nabla(\phi_i \phi_j \phi_k)$	$3(\phi_k \nabla \phi_i + \phi_i \nabla \phi_k) \times \nabla \phi_j$
$4\phi_j \phi_k (\phi_j - \phi_k) \nabla \phi_i - \nabla\left(\phi_i \phi_j \phi_k (\phi_j - \phi_k)\right)$	$4\left((\phi_j^2 - 2\phi_j \phi_k) \nabla \phi_k - (\phi_k^2 - 2\phi_j \phi_k) \nabla \phi_j\right) \times \nabla \phi_i$
$4\phi_k \phi_i (\phi_k - \phi_i) \nabla \phi_j - \nabla\left(\phi_i \phi_j \phi_k (\phi_k - \phi_i)\right)$	$4\left((\phi_k^2 - 2\phi_k \phi_i) \nabla \phi_i - (\phi_i^2 - 2\phi_k \phi_i) \nabla \phi_k\right) \times \nabla \phi_j$
$4\phi_i \phi_j (\phi_i - \phi_j) \nabla \phi_k - \nabla\left(\phi_i \phi_j \phi_k (\phi_i - \phi_j)\right)$	$4\left((\phi_i^2 - 2\phi_i \phi_j) \nabla \phi_j - (\phi_j^2 - 2\phi_i \phi_j) \nabla \phi_i\right) \times \nabla \phi_k$
$4\phi_j \phi_k \phi_l \nabla \phi_i - \nabla(\phi_i \phi_j \phi_k \phi_l)$	$4\left(\phi_k \phi_l \nabla \phi_j + \phi_j \phi_l \nabla \phi_k + \phi_j \phi_k \nabla \phi_l\right) \times \nabla \phi_i$
$4\phi_k \phi_l \phi_i \nabla \phi_j - \nabla(\phi_i \phi_j \phi_k \phi_l)$	$4(\phi_l \phi_i \nabla \phi_k + \phi_k \phi_i \nabla \phi_l + \phi_k \phi_l \nabla \phi_i) \times \nabla \phi_j$
$4\phi_l \phi_i \phi_j \nabla \phi_k - \nabla(\phi_i \phi_j \phi_k \phi_l)$	$4\left(\phi_i \phi_j \nabla \phi_l + \phi_l \phi_j \nabla \phi_i + \phi_l \phi_i \nabla \phi_j\right) \times \nabla \phi_k$

Table 2.4: Curls of $\mathcal{H}(\text{curl}, \Omega)$-conforming basis functions up to order $p = 3$.

nates

$$\begin{aligned} N_0 &:= (0,0,0), \\ N_1 &:= (1,0,0), \\ N_2 &:= (0,1,0), \\ N_3 &:= (0,0,1), \end{aligned}$$

has four scalar (*nodal*) first order shape functions defined as

$$\begin{aligned} \phi_0 &= 1-\xi-\eta-\zeta, \\ \phi_1 &= \xi, \\ \phi_2 &= \eta, \\ \phi_3 &= \zeta. \end{aligned}$$

Considering the linear mapping, the volume integration of a function in K can be transferred to an integration on K_0 such that [101]

$$\int_K f(x,y,z)\, dxdydz = \int_{K_0} f(\xi,\eta,\zeta)\ \det[J]\ d\xi d\eta d\zeta, \tag{2.3.38}$$

where we have made the following transformations

$$\begin{aligned} \phi(x,y,z) &\longrightarrow \phi(\xi,\eta,\zeta) \\ \nabla\phi(x,y,z) &\longrightarrow [J]^{-1}\nabla\phi(\xi,\eta,\zeta) \end{aligned} \tag{2.3.39}$$

As stated before, quadrature integration results to be an easy integration method for higher-order shape functions [109, 110], as a few sampling points of $f(\xi,\eta,\zeta)$ are required to achieve machine precision. As a result,

$$\int_{K_0} f(\xi,\eta,\zeta)\ \det[J]\ d\xi d\eta d\zeta \approx \sum_q^{N_q} f(\xi_q,\eta_q,\zeta_q)\, w_q,$$

where (ξ_q,η_q,ζ_q) is the simplex coordinate of the q^{th} point in the reference element and w_q the corresponding weight. A set of quadrature rules, which have been implemented in FES-3D, can be found in [111]. These allow to compute all the element matrices of first order with 4 points, second order with 11 and third order with 24 points, resulting in, respectively, $\mathbb{R}^{6\times6}$, $\mathbb{R}^{20\times20}$ and $\mathbb{R}^{45\times45}$ dense matrices. The number of points is actually related to the *mass* matrices, associated to the testing with the non-derived shape functions, which lead to the highest polynomial order for $f(x,y,z)$.

Once all the integrals derived from a Galerkin procedure are computed on an element, the coefficients must be added to the global system matrix taking into account, for $\mathcal{H}(\text{curl},K)$ matrices, the direction of the shape function defined on the edges and faces, in order to ensure the effective continuity of tangential components of the field. In fact, adjacent elements may result have opposite vector fields (hence

discontinuous) a their interface, due to arbitrary mappings. Local numbering of the elements may be uncorrelated to the global mapping of the mesh.

An simple and elegant manner to enforce continuity is to number the nodes of each element such that the node indices are taken in an increasing way [108], for instance

$$\begin{aligned} E\{i,j\} \quad &\text{with} \quad i<j, \\ F\{i,j,k\} \quad &\text{with} \quad i<j<k, \\ T\{i,j,k,l\} \quad &\text{with} \quad i<j<k<l, \end{aligned}$$

where the 2-tuple $E\{i,j\}$ with nodes i and j directed from i to j, the 3-tuple $F\{i,j,k\}$ is the face with nodes i, j and k and the 4-tuple $T\{i,j,k,l\}$ is the tetrahedron with nodes i, j, k and l. The face $F\{i,j,k\}$ between two adjacent tetrahedra will have three edges oriented in an unique way on both actual and reference element: $E\{i,j\}$, $E\{i,k\}$ and $E\{j,k\}$.

$$\begin{aligned} E\{i,j\} &\longrightarrow E_0\{i_0,j_0\}, \\ E\{i,k\} &\longrightarrow E_0\{i_0,k_0\}, \\ E\{j,k\} &\longrightarrow E_0\{j_0,k_0\}, \end{aligned}$$

where i_0, j_0 and k_0 are local indices of the reference element nodes. Same considerations can be made on the faces pertaining to a tetrahedron:

$$\begin{aligned} F\{i,j,k\} &\longrightarrow F_0\{0,1,2\}, \\ F\{i,j,l\} &\longrightarrow F_0\{0,1,3\}, \\ F\{i,k,l\} &\longrightarrow F_0\{0,2,3\}, \\ F\{j,k,l\} &\longrightarrow F_0\{1,2,3\}, \\ T\{i,j,k,l\} &\longrightarrow T_0\{0,1,2,3\}. \end{aligned}$$

The global numbering of the hierarchical shape functions can be made such that the resulting finite element coefficients are collected by their polynomial order p

$$\begin{bmatrix} A_{1,1} & A_{1,2} & \cdots & A_{1,p} \\ A_{2,1} & A_{2,2} & & \vdots \\ \vdots & & \ddots & \vdots \\ A_{p,1} & \cdots & \cdots & A_{p,p} \end{bmatrix}.$$

A consequence of this approach is that an efficient p-multilevel preconditioner can be built to accelerate iterative solvers on high-order finite element matrices [112, 113].

The assembly operation, which consists in the summation of finite element coefficients computed from elements that share at least one mesh entity (node, edge or face, depending on the king of shape functions), is done by mapping a local coefficient to a global mesh entity. In FES, the computation of element matrices and their assembly in global system matrix has been parallelized, on multicore CPU, by the use of OpenMP *parallel for* directive [114].

2.3.5 System solution

As introduced above, the system matrices are usually large, although they are sparse and symmetric. Therefore, an efficient solution of the finite element matrix equation is very important, because this aspect typically dominates the overall computer resources requirements.

The matrices produced by the finite element method are sparse, with only a very small percentage of nonzero elements. By storing only the nonzero entries [115], the matrix storage requirement is reduced from $O(N^2)$ to $O(N)$. Popular approaches to sparse matrix storage are those based on either a *compressed row* or a *compressed column* storage format. In these approaches, the nonzero entries of a sparse matrix are stored in a floating-point vector (single or double precision complex entries). In addition, an integer vector is employed to store the row or column indexes of the nonzero entries, and another integer vector is introduced to store the location of the first nonzero entry of each row in the compressed vector. For a symmetric matrix, only the nonzero entries in the upper or lower triangle (including those on the diagonal) need to be stored. In FES, the use of the template library GMM++ [116] has allowed for fast and memory efficient global matrix assembly.

The choice of a matrix solver can have a significant impact on the computational efficiency, and it is therefore important to choose a solver that can best exploit the properties of the finite element system matrix. There are two types of matrix solvers:

- the first, known as a *direct solver*, is based on Gaussian elimination, typically after LU or Cholesky decompositions. These solvers are commonly used for full matrices [117], although they are also applicable to sparse matrices, also called *sparse direct solvers*. During the past two decades, remarkable progress has been made on sparse direct solvers. Today, there are many highly robust and efficient direct solvers available that deal with sparse matrices. Among these, Intel's Math Kernel Library (MKL) [118] implements the PARDISO solver [119], a multicore sparse direct solver for both symmetric and unsymmetric matrices. Other open source solvers are UMFPACK [120], MUMPS [121], and SuperLU [122], which provide a scalable parallel solution on distributed memory computing systems (multiprocessor). FES employs MUMPS, a LU or Cholesky-based (depending on $[A]$ symmetry) sparse direct solver with out-of-core (OOC) capabilities, that is the possibility to store in non-volatile memory the computed factors, while keeping into physical memory only the necessary information for factors to be computed. This approach hence allows to solve larger systems than those can fit into physical memory at the expense of reducing the bandwidth to that of the non-volatile support. Recent hardware improvements such as the advent of solid state drives, which have a significantly greater bandwidth than classical (magneto-resistive) hard-drives, may increase the frontiers in direct matrices solution on a simple computer. FES-3D also make use of a multithreaded BLAS, OpenBLAS [123], to enable multicore

arithmetic operations for MUMPS. Also, the public package METIS [124] is employed for fill-in reduction (elements entries are reorder in order to compress them around the diagonal).

- the other, the *iterative solver*, requires significantly less memory than do direct solvers because they are based on calculating successive matrix-vector products according to an iterative algorithm that is designed to converge to the solution [125]. The main drawback of iterative techniques is that they may require a large number of iterations to converge, due primarily to the locations of the eigenvalues of the matrix in the complex plane. However, if the eigenvalues are all clustered around $(1,0)$, convergence is usually rapid. To improve the convergence of an iterative solver, a preconditioner is typically adopted to move the eigenvalues closer to $(1,0)$, thereby reducing the iteration count. A preconditioner can be constructed based on physical insight into the problem [126] or on the structure of the original matrix [127]. For iterative solvers, SPARSKIT [128] provide a variety of Krylov subspace algorithms, such as those based on the stabilized *biconjugate gradient squared* (BiCGStab) and *generalized minimal residual* (GMRES) methods, and a variety of preconditioners, such as the *incomplete LU* (ILU) and its threshold dropping version ILUT [129], and *successive over relaxation* (SSOR) preconditioners, to speed up the iterative convergence. Note that MKL also contains sparse iterative solvers. FES-3D implements the *restarded*-GMRES solver [130] mainly employed with the domain decomposition preconditioner as it will be shown in 3. The advantage of this Krylov subspace solver is that the number of vectors spanning the solution can be restricted to a "restarting" number r, and the Krylov spanning vectors of the successive GMRES cycle (as convergence may not be achieved within r iterations) are computed at from a starting vector which is the solution achieved at the previous GMRES cycle. This approach does not mathematically guarantee the convergence of the solver (due to restarting), however it has been found to be effective in all the analyses performed with FES-3D, at the expense of increasing the number of iterations.

2.3.6 Post processing

In the section of the finite element formulation, one of the relevant parameters in the analysis of electromagnetic structures with waveguide excitations have been introduced: the scattering parameters or S-parameters. One the finite element matrix has been solved, these can be be obtained after further testings of the field with the mode distributions on Γ_{WG}. The transfinite element method is such that these testings are incorporated in the system matrix, and hence the S-parameters are retrieved during the system solution. A noticeable advantage of the finite element method is that all the ports of an electromagnetic device or antenna array are coupled by means

of the finite element interactions, allowing thus for a rigorous analysis of multiple antennas interactions or the accurate response of a microwave device.

When analyzing antennas, several parameters are of paramount importance in order to define their performances. Some of these are the antenna *directivity* or the *gain*, which are related to the capability of the antenna to radiate fields in a given direction $\hat{\mathbf{r}}$ far away ($kr \gg \lambda$) from the antenna. One can think of an antenna as the medium of transition of an impinging field in the excited port to the free space. Hence, one has to compute the field radiated far away from the antenna in direction $\hat{\mathbf{r}}$. But with the finite element method, we have restricted the domain of analysis to the surrounding of the antenna. However, we can use the Huygens' principle, which states that fields computed on a bounded surface or an advancing front of a propagating wave can be used to compute the next wave-front and so on. Also, it can be proved that tangential fields on any regular bounding surface are sufficient to compute the radiated fields [93]. Hence, the tangential components of the fields $\mathbf{E} \times \hat{\mathbf{n}}$ and $\hat{\mathbf{n}} \times \mathbf{H}$ must be known only on Γ_R. In fact, there might be power flowing through Robin boundaries, which enforce the continuity of waves, whereas Dirichlet or Neumann boundaries are such all the power is reflected on them.

By Sommerfeld's radiation condition states that far-zone fields in the direction $\hat{\mathbf{r}}$, assuming free-space propagation, behave as

$$(\nabla \times \mathbf{E}(\hat{\mathbf{r}})) \times \hat{\mathbf{r}} + jk_0 \mathbf{E}(\hat{\mathbf{r}}) \overset{r\to\infty}{\approx} 0,$$

and hence the following relation between the fields can be obtained

$$\mathbf{E}(\hat{\mathbf{r}}) = \zeta_0 \mathbf{H}(\hat{\mathbf{r}}) \times \hat{\mathbf{r}}.$$

This means the fields behave locally as plane wave, that is the electric and magnetic field are orthogonal and they are both orthogonal to the propagating direction $\hat{\mathbf{r}}$. The corresponding Poynting vector,

$$\mathbf{S}(\hat{\mathbf{r}}) = \frac{1}{2}\mathbf{E}^*(\hat{\mathbf{r}}) \times \mathbf{H}(\hat{\mathbf{r}}) \overset{r\to\infty}{=} \frac{|\mathbf{E}(\hat{\mathbf{r}})|^2}{2\zeta_0}\hat{\mathbf{r}}, \qquad \left[\frac{\mathrm{W}}{\mathrm{m}^2}\right],$$

provides the electromagnetic power density flowing in that direction. To compute the Poynting vector, only the knowledge of the far-zone electric field is required, and it can be computed through Stratton-Chu relations [131] written in Kottler's form in order to remove the the gradients of the free-space Green's function. The resulting integral must be computed in

$$\begin{aligned} \mathbf{E}(\hat{\mathbf{r}}) \;=\; & j\zeta_0 k_0 \frac{\mathrm{e}^{-jkr}}{4\pi r} \int_{\Gamma_R} \mathrm{e}^{jk\hat{\mathbf{r}}\cdot\mathbf{r}'} \left[\left(\hat{\mathbf{n}} \times \mathbf{H}(\mathbf{r}') \cdot \hat{\mathbf{r}}\right)\hat{\mathbf{r}} - \hat{\mathbf{n}} \times \mathbf{H}(\mathbf{r}') \right] d\Gamma \;- \\ & jk_0 \frac{\mathrm{e}^{-jkr}}{4\pi r} \int_{\Gamma_R} \mathrm{e}^{jk\hat{\mathbf{r}}\cdot\mathbf{r}'}\, \mathbf{E}(\mathbf{r}') \times \hat{\mathbf{n}} \times \hat{\mathbf{r}}\, d\Gamma, \end{aligned} \tag{2.3.40}$$

where $\mathbf{r}'$ is a vector pointing to the surface Γ_R. The integral relation (2.3.40) can be computed with quadrature rules over the triangles that constitutes the boundary

Γ_R, as the solution of the finite element system provides the electric and magnetic (through (2.2.5)) fields in Ω. Finally, directivity $D(\hat{\mathbf{r}})$ and gain $G(\hat{\mathbf{r}})$ are computed by

$$D(\hat{\mathbf{r}}) = \lim_{r\to\infty} 4\pi r^2 \frac{\mathbf{S}(\hat{\mathbf{r}})\cdot\hat{\mathbf{r}}}{P_{\text{rad}}} = \lim_{r\to\infty} 2\pi r^2 \frac{|\mathbf{E}(\hat{\mathbf{r}})|^2}{\zeta_0 P_{\text{rad}}}, \tag{2.3.41}$$

$$G(\hat{\mathbf{r}}) = \lim_{r\to\infty} 4\pi r^2 \frac{\mathbf{S}(\hat{\mathbf{r}})\cdot\hat{\mathbf{r}}}{P_{\text{in}}} = \lim_{r\to\infty} 2\pi r^2 \frac{|\mathbf{E}(\hat{\mathbf{r}})|^2}{\zeta_0 P_{\text{in}}}, \tag{2.3.42}$$

where P_{rad} is the power flowing through Γ_R computed as

$$P_{\text{rad}} = \int_{\Gamma_R} \mathbf{E}^* \times \mathbf{H}\cdot\hat{\mathbf{n}}\, d\Gamma,$$

and P_{in} is the total power entering in Ω through Γ_{WG}

$$P_{\text{in}} = -\int_{\Gamma_{WG}} \mathbf{E}^* \times \mathbf{H}\cdot\hat{\mathbf{n}}\, d\Gamma.$$

Once the S-parameters are known, P_{in} can be retrieved upon computing

$$P_{\text{in}} = \sum_{k=1}^{N_M^{\text{feed}}} 1 - |S_{kk}|^2,$$

where N_M^{feed} is the actual number of modes feeding the electromagnetic structure through Γ_{WG}. Note that the limit $r\to\infty$ in (2.3.41) and (2.3.42) can be removed upon neglecting the term $\frac{e^{-jkr}}{r}$ in (2.3.40).

In electromagnetic wave scattering problems, the *(bistatic) radar cross section* RCS provides information on how an object (or electromagnetic structure in Ω) scatters the electromagnetic field coming from an impinging plane wave, and is defined as

$$RCS(\hat{\mathbf{r}}) = \lim_{r\to\infty} 4\pi r^2 \frac{|\mathbf{E}(\hat{\mathbf{r}})|^2}{|\mathbf{E}^{inc}|^2}. \tag{2.3.43}$$

At last but not least, one might be interested in recovering the field values in each point $\mathbf{r}\in\Omega$. This can be done upon retrieving the element of the mesh that contains $\mathbf{r}$ (with efficient algorithms such as octrees [132]) and remembering that

$$\mathbf{E}_E(\mathbf{r}) := \sum_{j=1}^{N} x_j \mathbf{w}_j(\mathbf{r}),$$

and

$$\mathbf{H}_E(\mathbf{r}) := \sum_{j=1}^{N} x_j \frac{\nabla\times\mathbf{w}_j(\mathbf{r})}{-jk_0\zeta_0\mu_r(\mathbf{r})}.$$

The local support of $\mathbf{w}_j(\mathbf{r})$ is such that

$$\mathbf{w}_j(\mathbf{r}) = \begin{cases} \mathbf{w}_j(\mathbf{r}), & \mathbf{r}\in K, \\ 0, & \mathbf{r}\notin K, \end{cases} \tag{2.3.44}$$

where K is any element of the mesh. Notice that for $\mathbf{r}$ located on the face shared by two elements, the tangential components are continuous, hence equal, but normal

components may not. We may approximate the normal component as the average of the normal components computed in both elements. In FES-3D, the evaluation of (2.3.40) has been parallelized with OpenMP for the look angles $\hat{\mathbf{r}}$.

Visualization of electromagnetic quantities in higher-order finite elements, is a computationally demanding step. In fact, most of the rendering environments (DirectX, OpenGL,...) which directly communicate with the GPU interpolate linearly quantities to display. Hence one must increase the number of sampling points of the fields in order to accurately visualize them.

FES, at this stage, samples the fields at the nodes of the mesh and generates a *Visualization ToolKit* (VTK) file [133], an open format for scientific visualization. In particular, packages (ParaView, MayaVi) that adopt this format allow for visualization of scalars and vectors on structured or unstructured 2D or 3D meshes. Also, operations such as cutting planes, contours plotting, arithmetics might be available. For orders $p = 2$ and 3, the mesh is refined (Fig. 2.6) before evaluation of the fields, generating much more sampling nodes. An efficient procedure might be based on oversampling only where the fields vary rapidly, based on error estimation [134].

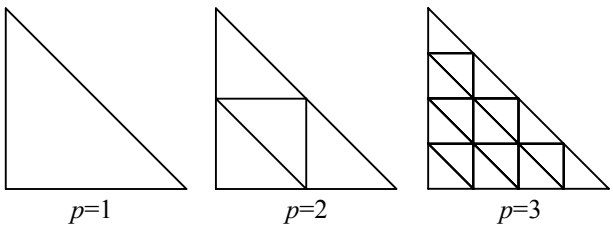

Figure 2.6: Homogeneous refinement for higher-order finite elements solution visualization.

2.4 Numerical tests

This section presents the analysis of four different 3D microwave problems analyzed by FES-3D with the respective comparisons with HFSS (version 10) models:

- a millimeter-wave E-plane bandpass filter [135],
- a Ka-band corrugated circular horn tailored for radio-astronomy [136],
- a simple perfect electric scattering sphere.

The purpose these tests is to validate the capabilities of the formulations implemented and show some of the features of FES. The core of FES will be extended in the next chapters, where a domain decomposition methods and harmonic balance for nonlinear analyzes of microwave devices will be presented. Computations are made on AMD Phenom II X4 965 processor with 16 GB of available DDR3 physical memory.

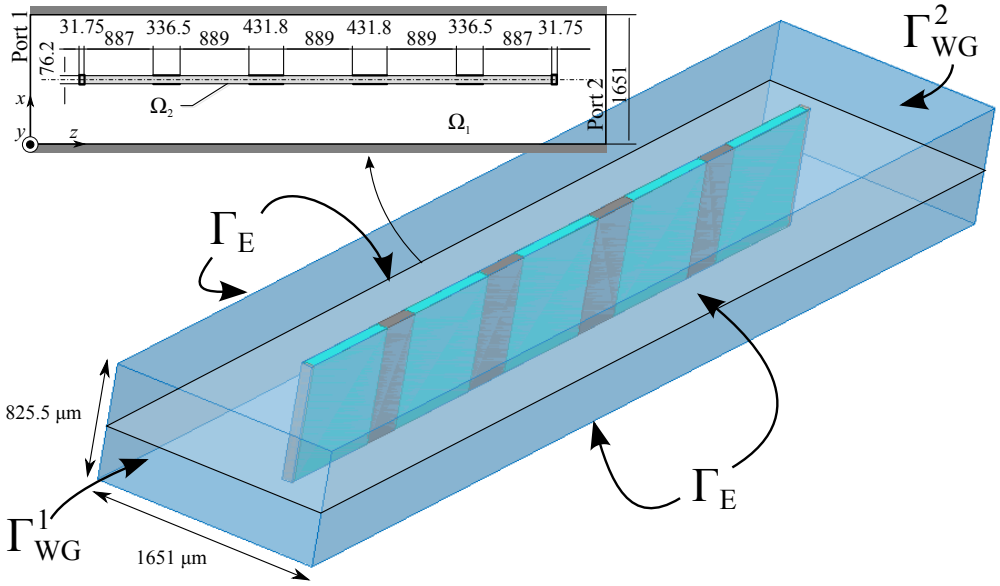

Figure 2.7: Sketch for the millimeter-wave waveguide filter analyzed and its cross section (H-plane). Measures are given in μm.

2.4.1 Millimeter-wave E-plane bandpass filter analysis

The passband filter designed and presented in [135] is realized by placing on the E-plane a dielectric slab ($\epsilon_r = 2.1$ in Ω_2) partially metalized on both sides in a WR6 rectangular waveguide (Fig. 2.7). All metallic parts will be considered in the FE model as perfect electric conductor. The remaining of the device is devoid of air.

The mesh is composed of 9686 tetrahedra (not visible here) for a total of 2074 conjunction nodes. The mesh assembly, with second order basis functions, required about 1.3 s for each frequency of analysis. The boundary conditions where then imposed on the waveports considering both the formulations presented in the previous section. Each 2D eigenmode problem, with second order basis functions, could be solved in approximately 0.4 s. The ARPACK solver, using MUMPS for matrices inversion in the $[B]$-orthogonalization, converged in only 19 iterations (to 10^{-12}). The dominant mode formulation lead to 57 524 unknowns for a full second order assembly while the transfinite element required less, 56 490 unknowns, as the unknowns on the waveports where removed from the system matrix. The overall assembly and solve times where, with the single precision solver, about 5.5 s (2.3 s + 3.2 s) and requiring 132 MB of memory. The double precision solver required approximately the same times, while about twice the memory (255 MB) was needed. Notice that HFSS required only 2 s and about 130 MB of memory for this problem. This could be imparted mainly to the fact it employs a mixed precision solver [137] for real matrices (in fact they are as no material losses or absorbing boundary conditions are introduced). This kind of solvers iteratively refines the solution provided by a single precision solver $[x]_{\mathrm{s}}^{i} = [A]_{\mathrm{s}}^{-1}[b]_{\mathrm{s}} \rightarrow [x]_{\mathrm{d}}^{i}$, upon computing a double precision residual vector $[r]_{\mathrm{d}} = [b]_{\mathrm{d}} - [A]_{\mathrm{d}}[x]_{\mathrm{d}}^{i}$. Then, the problem on the residual ($[r]_{\mathrm{d}} \rightarrow [r]_{\mathrm{s}}$)

is solved and added to the double precision solver: $[x]_{\mathrm{d}}^{i+1} \leftarrow [x]_{\mathrm{d}}^{i} + [A]_{\mathrm{s}}^{-1}[r]_{\mathrm{s}}$. s and d subscripts correspond, respectively, to single and double precision versions of the matrices or vectors. Furthermore, the use of real matrices noticeably reduce the computational requirements. However, as the purpose of the implemented package is to introduce new computational methodologies, for instance domain decomposition and nonlinear analyzes, the use of real solvers (available with MUMPS) has not been implemented yet.

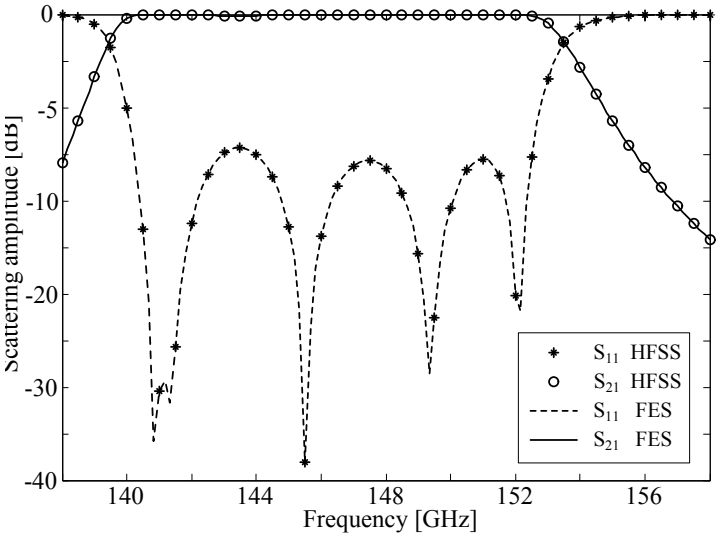

Figure 2.8: Frequency response of the dominant TE_{10} mode in the filter, computed with single precision MUMPS solver and dominant mode waveports boundary condition.

The frequency (linear) response of the filter, computed with the single precision solver with dominant mode boundary condition on ports, visibly results to be in good agreement with HFSS. In fact, as single precision solver has a numerical error floor of $\approx 10^{-6}$, the dynamic response of the device (≈ -40 dB to 0 dB) could fit in the dynamic range of numerical precision.

Dominant (s)	Dominant (d)	Transfinite (s)	Transfinite (d)
$1.5351\ 10^{-6}$	$1.3643\ 10^{-6}$	$5.6383\ 10^{-7}$	$1.6853\ 10^{-12}$

Table 2.5: Comparison between the average Euclidean errors for both waveport continuity formulations (only dominant TE_{10} mode retained), varying the solver precision (s=single, d=double).

Table 2.5 shows the relative error $\mathcal{L}^2([S(f)],\ f \in [138, 158]$ GHz) between the four combinations of waveports formulations and solvers precisions and the solution provided by the mixed precision (real) solver of HFSS in discrete sweep mode. The error is averaged on the 41 equally spaced selected frequency points within the range specified. As we can see, the lower accuracy of the dominant mode formulation is

such that a double precision solver does not improve computations. Nevertheless, there no practically appreciable differences between the responses (Fig. 2.8). The transfinite element formulation, being more robust, is such that equivalence in results is achieved within numerical precision.

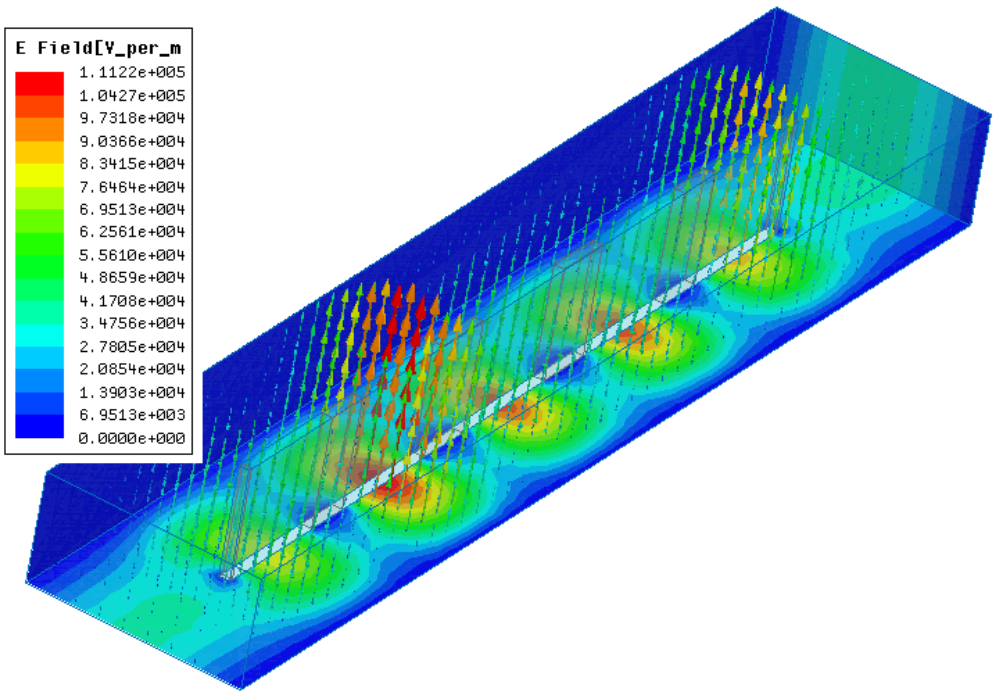

Figure 2.9: Electric field at 150 GHz computed by means of HFSS.

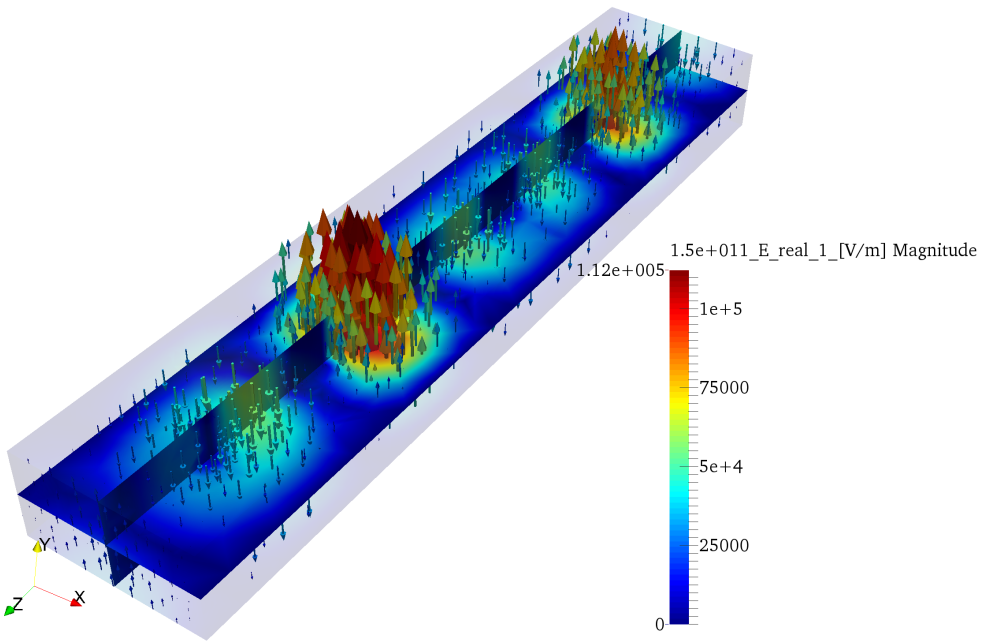

Figure 2.10: Electric field at 150 GHz computed by means of FES and visualized in Paraview.

After the computation of scattering parameters, one might be interested in visualizing the fields at a given frequency. Figs. 2.9 and 2.10 show the electric fields (real parts) computed at 150 GHz. The electric and magnetic fields, in FES, are computed upon interpolating the respective shape functions at the nodes of the mesh (refined in this case as $p = 2$). There is a good agreement between the two electromagnetic solvers and maximum amplitude of the electric field of $\approx 112\ \frac{\text{kV}}{\text{m}}$ is attained within the device. Vertical and horizontal cut-planes can be easily obtained in Paraview upon selecting the "slicing" function.

2.4.2 Corrugated circular horn analysis

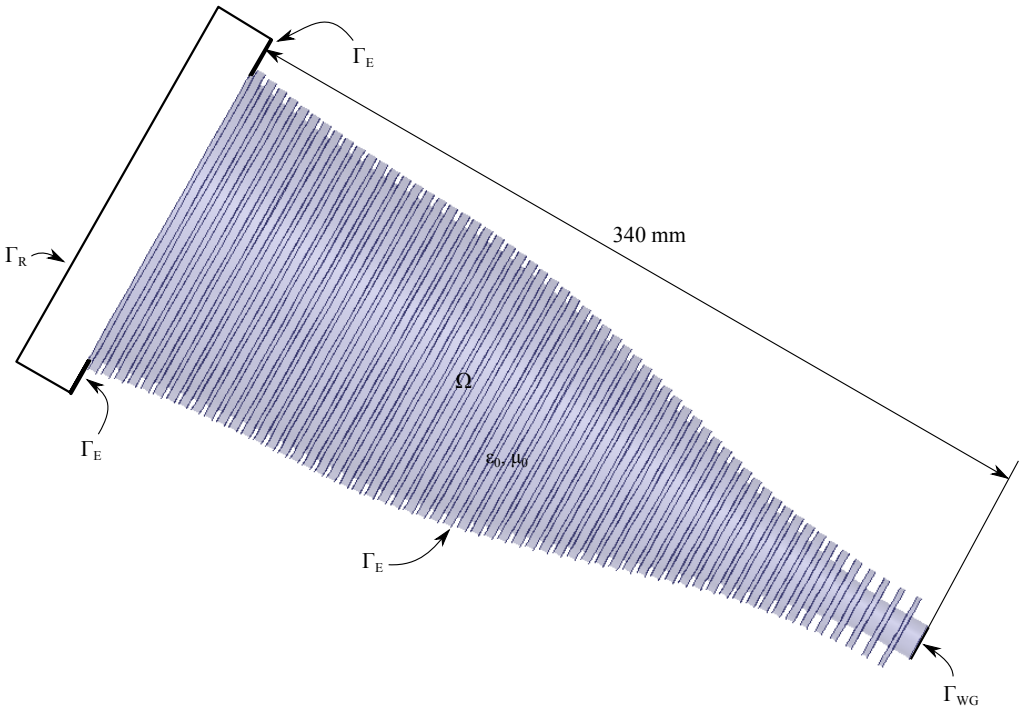

Figure 2.11: Sketch of the 22 GHz corrugated circular horn antenna.

In the work [136], there were shown a 22 GHz corrugated circular horn antenna built at the "Osservatorio Astrofisico di Arcetri", an institute for radio-astronomical studies of the (Italian) National Research Council. That horn, whose model is depicted in Fig. 2.11, is made of 60 corrugations in order to smooth gradually the transition between guided waves to radiated waves and achieve a pure linear polarization. This procedure results in a better tapering of the radiation pattern, significantly lowering the side lobes. In its designed working conditions, the horn is fed with two degenerate TE_{11} circular waveguide modes in quadrature: they are both physically oriented perpendicularly and with 90° of phase shift.

Here, we have tested the capabilities of FES to analyze multimode problems, with the transfinite element method, and it is a first attempt to evaluate radiation boundary conditions. Notice that antenna is about 25 wavelengths long and the

corrugations dramatically increase tetrahedra's number of the mesh, for conformity constraints to the geometry. The antenna is terminated at its narrower end by a circular waveport boundary and at the mouth or aperture of the horn, by a parallelepiped box on which radiation conditions are imposed. Of course, both horn and box are merged in order to have a unique enclosed medium devoid of air. Simulations are performed with cubic order shape functions.

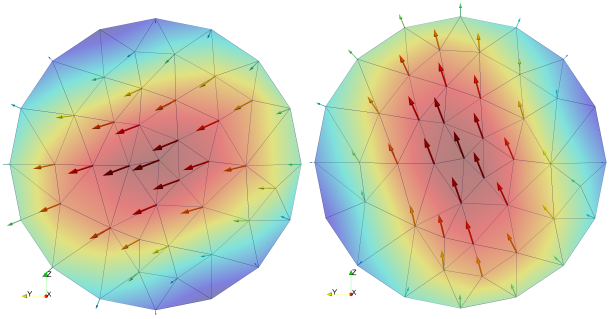

Figure 2.12: Degenerate TE_{11} modes feeding the antenna (in quadrature).

The first five modes were computed with ARPACK, and 36 iterations where needed to converge in about 2 s. The excitation modes are shown Fig. 2.12. Then the assembly and solve on 602 594 unknowns (36 331) required for the single precision solver about 123 s while the double precision 170 s. In fact, as both the matrices are assemble in the double precision, the single precision solver required 47 s less than its double precision counterpart. Also, memory requirements where different: 3158 MB for the single precision and 6159 MB for the double. Notice that HFSS required 146 s and 3.7 GB of memory to solve the problem with its mixed precision complex solver, which is in good agreement with what was stated before.

$$
|[S]|_{\mathrm{dB}}^{\mathrm{HFSS}} = \begin{bmatrix} -49.7001 & -60.5669 & -55.9466 & -82.8433 & -79.8956 \\ -60.5669 & -49.9378 & -46.5148 & -87.5034 & -81.1233 \\ -55.9460 & -46.5148 & -3.4413 & -80.8478 & -86.5927 \\ -82.8433 & -87.5033 & -80.8478 & -48.4840 & -88.2707 \\ -79.8958 & -81.1234 & -86.5927 & -88.2707 & -48.3815 \end{bmatrix},
$$

$$
|[S]|_{\mathrm{dB}}^{\mathrm{TFE,single}} = \begin{bmatrix} -49.0035 & -63.4025 & -64.6486 & -80.1454 & -80.7432 \\ -63.2030 & -49.6485 & -46.1201 & -91.9744 & -82.0608 \\ -64.4864 & -46.1409 & -3.4416 & -81.8164 & -84.3125 \\ -80.1613 & -91.9789 & -81.8047 & -48.5274 & -91.8034 \\ -80.7334 & -82.0586 & -84.3199 & -91.8016 & -48.3397 \end{bmatrix},
$$

$$
|[S]|_{\mathrm{dB}}^{\mathrm{TFE,double}} = \begin{bmatrix} -49.1332 & -63.1736 & -64.5808 & -80.1579 & -80.7213 \\ -63.1736 & -49.9021 & -46.1233 & -92.0040 & -82.1035 \\ -64.5808 & -46.1233 & -3.4414 & -81.8144 & -84.1136 \\ -80.1579 & -92.0040 & -81.8144 & -48.5264 & -91.8808 \\ -80.7213 & -82.1035 & -84.1136 & -91.8808 & -48.3394 \end{bmatrix}.
$$

The magnitudes of the scattering parameters, shown above, agree within an average error of $\approx 7\ 10^{-5}$ for single and double precision FES solvers relatively to HFSS solver. Values are, in practical terms, the same. Differences between the results might be imparted also to the use of different third order shape functions between FES and HFSS.

When analyzing antennas, one might be interested in its performances in terms of directivity or gain. Here, as no lossy materials are present, the gain equals the directivity. Figs. 2.13 and 2.14 show the radiation solids computed by HFSS and FES (VTK file). The gain of the antenna is of about 25.5 dB, and when fed in quadrature, circular polarization is achieved. The postpocessing time was about 302 s for FES, while only about 51 s for HFSS on 259 200 look angles. In Paraview, it is also possible to visualize the far field $\mathbf{E}(\hat{\mathbf{r}})$ as vectors in order to visualize the polarization achieved (in all directions) while time elapses. Also, slices data can be exported for radiation patterns plots on cut-planes (Fig. 2.15).

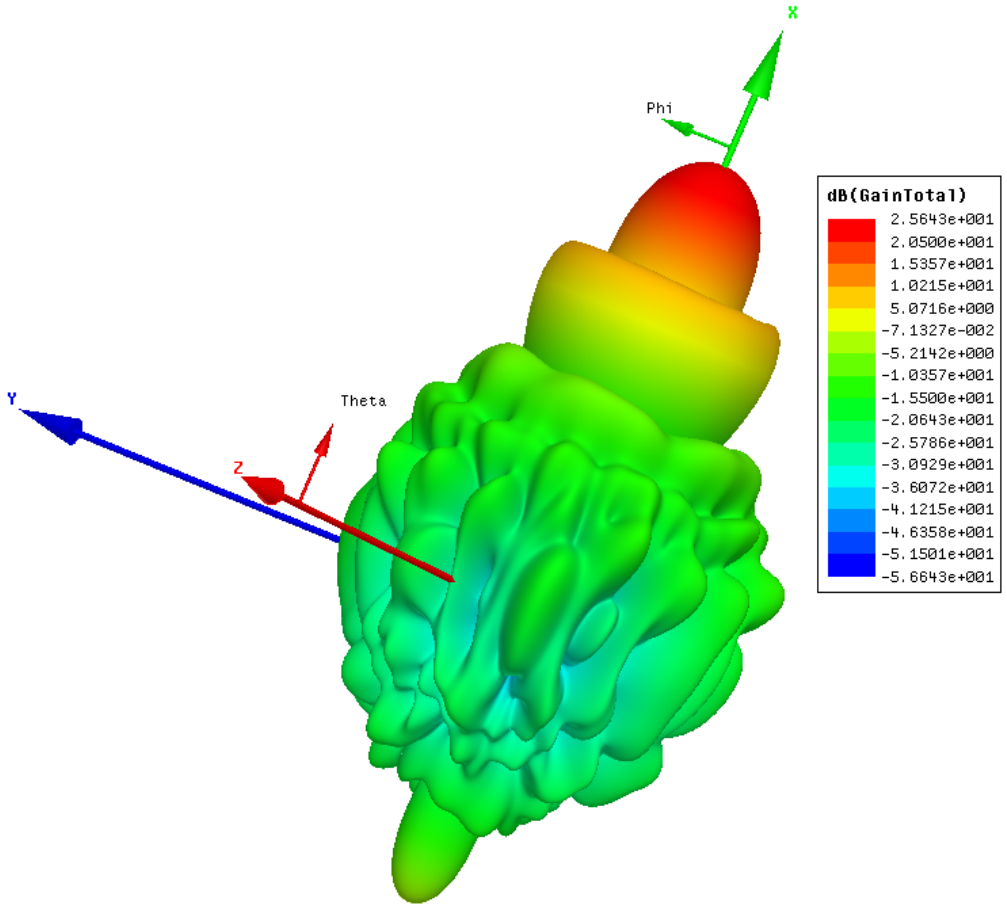

Figure 2.13: Radiation solid at 22 GHz computed with HFSS.

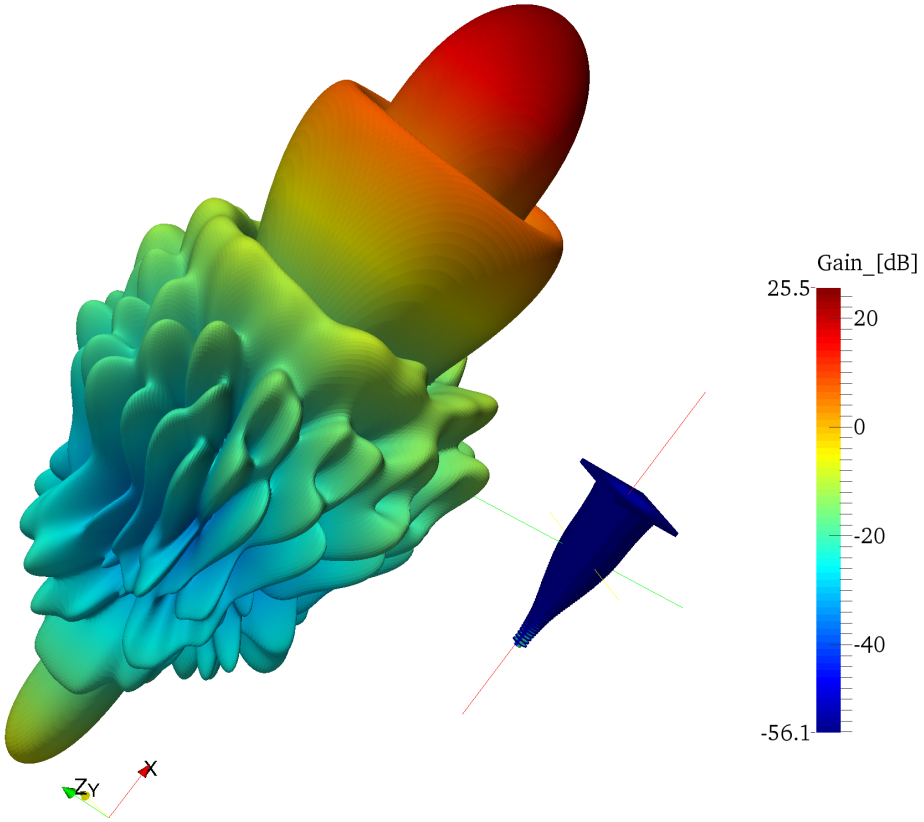

Figure 2.14: Radiation solid at 22 GHz computed with FES.

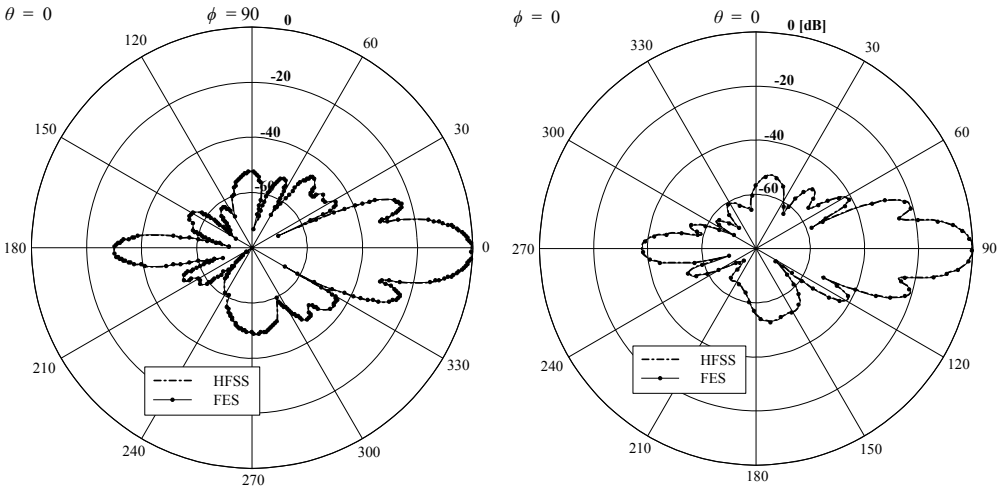

Figure 2.15: Normalized gain patterns on the *XY* (left) and the *XZ* (right) planes.

2.4.3 Perfect electric scattering sphere

Another test, which is "classical" among all the electromagnetic problems as it founds since more than a century an analytical solution, is that of a metallic sphere located in free-space, made of perfect electric conductor, on which impinges a plane wave from one direction. The domain of finite element analysis is shown in Fig. 2.16.

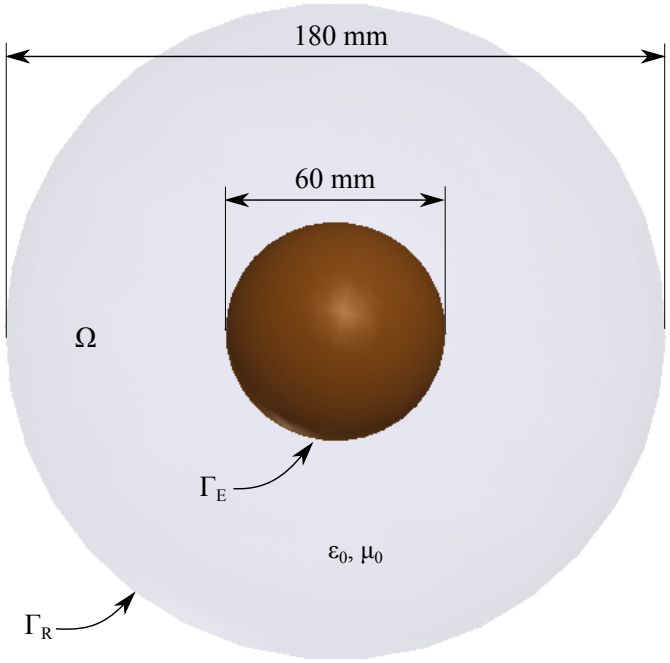

Figure 2.16: Sketch the scattering problem by a perfectly conducting metallic sphere.

Consider a plane wave at frequency f, traveling in free-space in the direction $\hat{\mathbf{z}}$. Hence the incident electric field, polarized along $\hat{\mathbf{x}}$, can be written as

$$\mathbf{E}^{inc} = |\mathbf{E}^{inc}| e^{-jk_0 \hat{\mathbf{z}}\cdot\mathbf{r}}\, \hat{\mathbf{x}},$$

and the magnetic field

$$\mathbf{H}^{inc} = \frac{1}{\zeta_0}\mathbf{E}^{inc} \times \hat{\mathbf{z}} = \frac{1}{\zeta_0}|\mathbf{E}^{inc}| e^{-jk_0 \hat{\mathbf{z}}\cdot\mathbf{r}}\, \hat{\mathbf{y}}.$$

These values can be substituted in the formulation 2.3.34 in order to compute the integrals on Γ_R. In this test case, we have considered the wave, with $|\mathbf{E}^{inc}| = \frac{\mathrm{V}}{\mathrm{m}}$, to be oscillating at 6 GHz. The mesh of 73,252 tetrahedra led to only 89,946 unknowns. The electric fields computed by both HFSS and FES (double precision) are shown in Figs 2.17 and 2.18, considering first order basis functions. The maximum magnitude of the electric field in the domain of analysis Ω was of about 1.52 $\frac{\mathrm{V}}{\mathrm{m}}$ in both cases, and the overall distribution was approximately the same. Due to linear polarization along the $\hat{\mathbf{x}}$ axis, the XZ cut-plane, so-called E-plane, shows a different electric field distribution respectively to that on the YZ cut-plane, the H-plane.

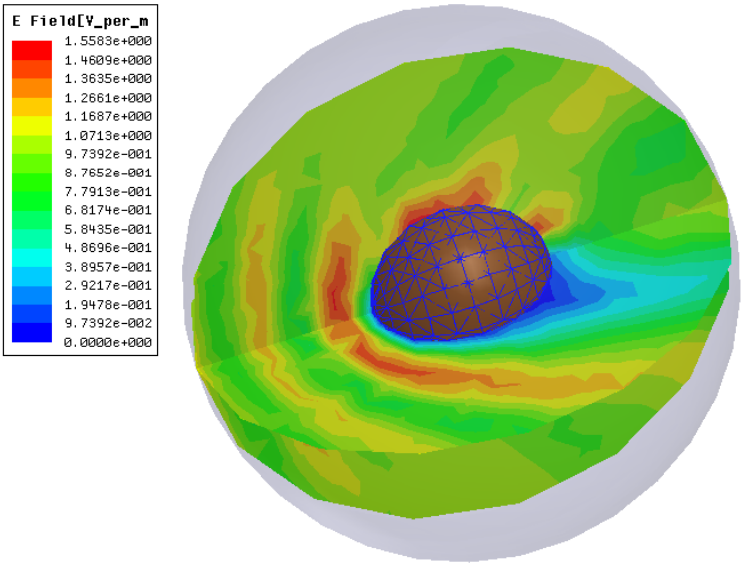

Figure 2.17: Electric field surrounding the perfectly conducting metallic sphere, computed with HFSS.

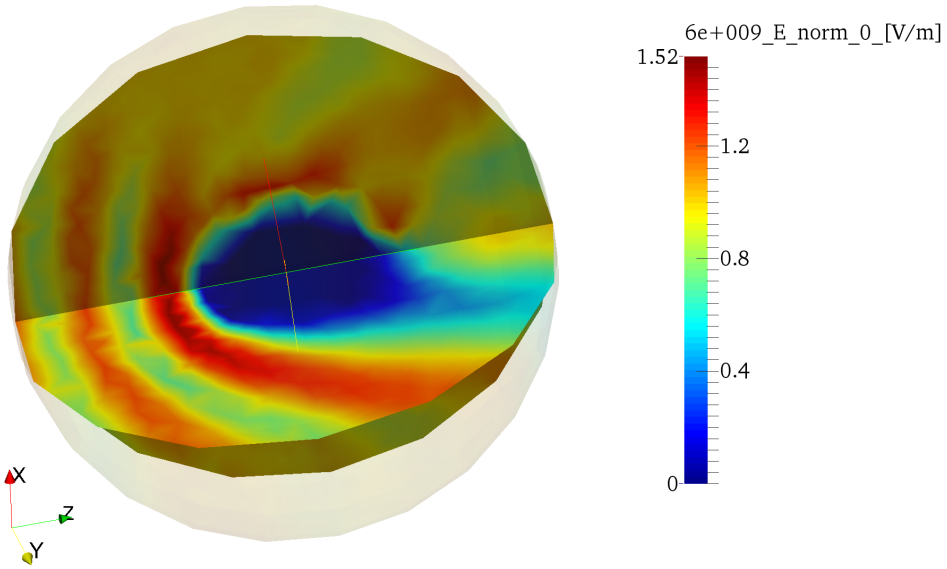

Figure 2.18: Electric field surrounding the perfectly conducting metallic sphere, computed with FES.

The radar cross section magnitude in decibels is shown in Figs. 2.19 and 2.20. Also here there is a good a agreement between the solvers, and a maximum of -12 dB in the $\hat{\mathbf{z}}$ direction. The mean relative error between the single precision and HFSS is of 4.49 10^{-4} while with the double precision solver we had 9.21 10^{-5}, hence the difference in the formulations is more important. However, in practical analyzes, one may consider the results equivalent (1% error is still neglectable).

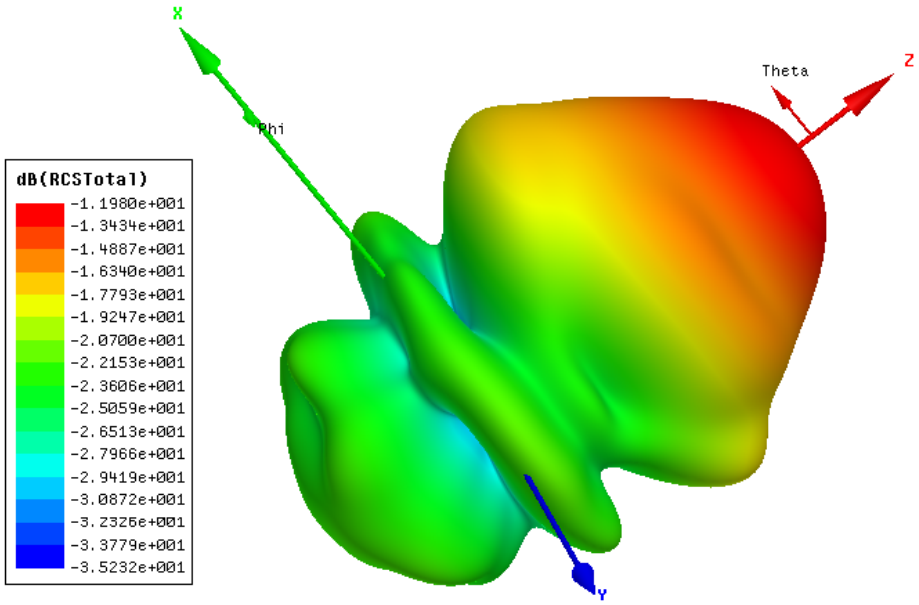

Figure 2.19: Radar cross section of the sphere, computed with HFSS.

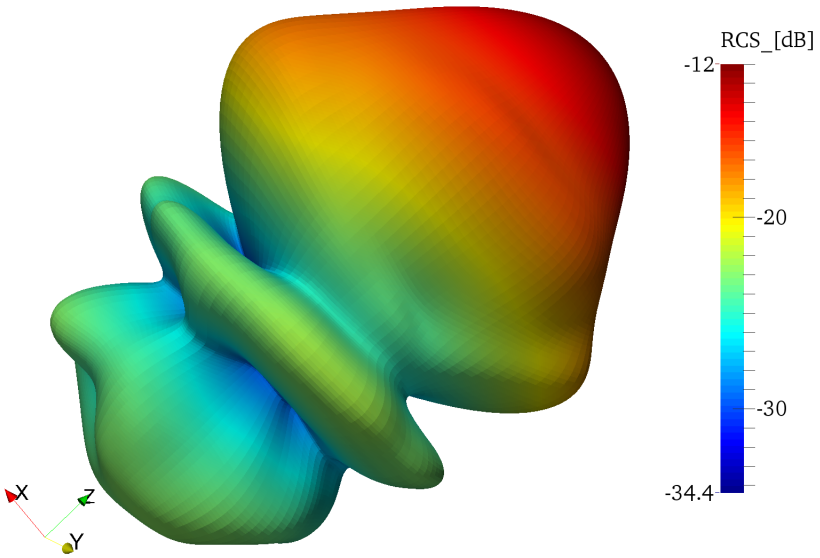

Figure 2.20: Radar cross section of the sphere, computed with FES.

As said previously, in Paraview it is possible to visualize the electric far field vectors (in the limit of $r \to \infty$), and hence its polarization. In Fig. 2.21, these vectors are shown and one can see that the fields scattered in $\hat{\mathbf{z}}$-direction remain polarized as the impinging wave, while in other directions the fields might change their polarization.

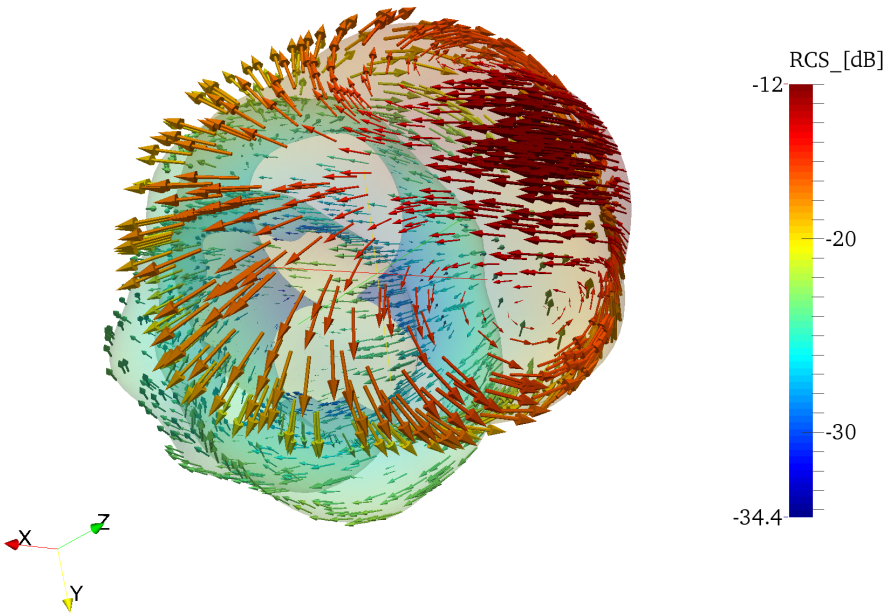

Figure 2.21: Polarization of the electric far field visualized with Paraview.

Chapter 3

Domain decomposition methods for large problems

The most important limit of numerical full-wave electromagnetic analyzes is the fact computational resources are limited, at least when trying to fit all the problem in memory at a time! Even if one had infinite computational resources, many algorithms, say even the solvers, would be such that it would require a huge amount of times to solve very large problems.

Nowadays, we refer to "large problems" to meshes that lead to millions of unknowns, up to several millions. In chapter 2, we could solve acceptably a 600,000 unknowns problem in about 2 minutes (section 2.4.2). But notice that it required about 3.1 GB of memory, which can easily fit in modern (low-cost) personal. But what would happen if we try to analyze an array of this antenna? The problem, if full-wave solution is still sought for, would be to solve the wave equation in the all the horns connected by a wide radiation boundary box to consider mutual coupling between the antennas. This slightly increases the number of finite element unknowns that we would have upon multiplying the 600,000 unknowns by the number of antennas. It is evident that we quickly reach the limit on a simple computer. To overcome this problem, parallel processing needs to be considered, devoting the matrix inversion to multiple computers interconnected through a high speed network. Iterative solvers, even if they require a minimum of memory which necessary to have the finite element system built, the number of iterations grows dramatically with the number of unknowns, hence the amount of times required for an acceptable analysis might not be tolerable.

Among the methods developed to increase the computational efficiency of finite element solvers, domain decomposition (DD) methods have found noticeable interest in the last decade. They allow to analyze a whole problem upon partitioning it and computing solutions for each smaller problem. Then, all the solutions are "connected" in order to recover the effective solution within the whole domain. Relying on a *divide et impera* scheme, these methods are *de facto* intrinsically parallelizable.

In fact, multiple domains can be analyzed contemporaneously on different processors. Another interesting aspect is that, when no cluster of computers is available to scale the problem, each smaller problem or *subdomain* can be tackled faster with direct solvers, one a time, while keeping in memory only the necessary information to recover the global solution.

A critical part of the domain decomposition method is how the information on the subdomains is collected and transferred to the global problem in order to achieve the original problem solution. There exist in literature [45,46] many mathematically proven algorithms that lead to a domain decomposed solution for a variety of problems (Laplace, Helmholtz, Navier-Stokes and other PDEs) given a particular decomposition scheme. The first domain decomposition algorithm is more than a century old: Schwarz proposed, at the end of 19^{th} century, an alternating algorithm for the solution of Poisson problems on overlapping subdomains [138], proving later its the convergence. With the advent of the personal computer, this research field begun to find many interesting applications. The first non-overlapping appeared in 1990 [139] and this opened the investigation to a new class of domain decomposition algorithms. It is evident, from a computational point of view, how this decomposition scheme is easier to handle. However, new truncation conditions have to be enforced as only the informations on the boundaries can be transferred to the adjacent subdomains.

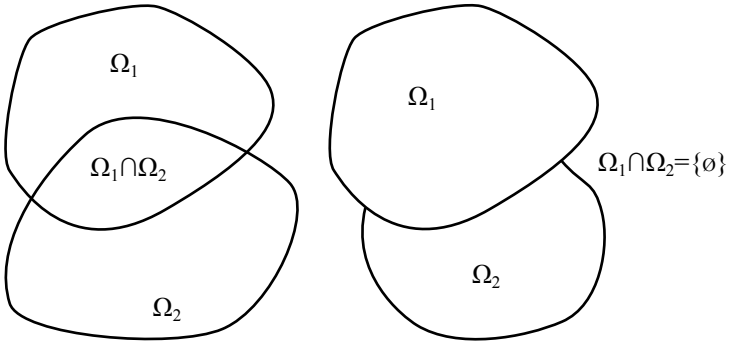

Figure 3.1: Overlaping and non-overlaping domain decomposition schemes.

In this chapter, we investigate two non-overlapping or *iterative substructuring* domain decomposition methods: a Schur Complement based method and a Finite Element Tearing and Interconnecting Dual-Primal (FETI-DP) based method in order to solve large radiation problems either for sequential or parallel computing. In particular, the DD frameworks are employed as preconditionners for iterative solvers for sequential processing. Direct solvers, being the best suited for small problems, can be employed in a DD framework to accelerate the convergence of iterative solvers. Several tests will be performed, first analyzing the performances of the algorithms on an arbitrarily partitioned rectangular waveguide problem.

3.1 Schur complement based domain decomposition

As we have seen in chapter 2, the unknowns resulting from a Galerkin framework are somehow related to mesh entities. If one could collect sequentially, during the mapping to the system matrix, the unknowns pertaining to a subdomain, then the resulting matrix would have a block-diagonal form. Of course, the unknowns related to the subdomain boundaries cannot be duplicated, otherwise the resulting system would be undetermined. Thus, one can collect all the unknowns pertaining to the boundaries between subdomains in a new diagonal block. These unknowns, being dependent on the elements pertaining to two (or more) adjacent subdomains, will lead to coefficient global matrix entries connected to these subdomains unknowns.

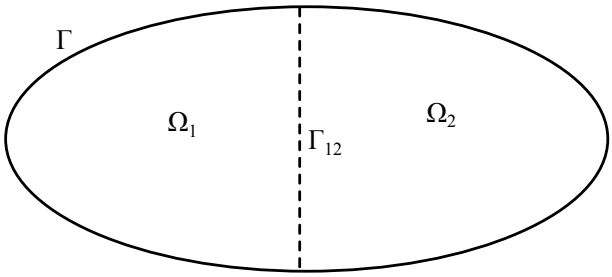

Figure 3.2: Schur complement based domain decomposition sketch for two subdomains.

Consider the domain decomposition of Ω in two subdomains as shown in Fig. 3.2. The resulting system matrix of any formulation employed in chapter 2 is

$$\begin{bmatrix} A_{\Gamma\Gamma} & A_{\Gamma 1} & A_{\Gamma 2} \\ A_{1\Gamma} & A_{11} & \\ A_{2\Gamma} & & A_{22} \end{bmatrix} \begin{bmatrix} x_\Gamma \\ x_1 \\ x_2 \end{bmatrix} = \begin{bmatrix} B_\Gamma \\ \\ \end{bmatrix}, \tag{3.1.1}$$

where the subscript Γ refers to shape functions with related mesh entity on $\Gamma \equiv \Gamma_E \cup \Gamma_H \cup \Gamma_R \cup \Gamma_{WG} \cup \Gamma_{12}$, and the subscript $j \in \{1,2\}$ refers to unknowns pertaining exclusively to mesh entities in Ω_j. Notice that the right-hand side has only non-zero entries for the formulations employed in chapter 2, the Dirichlet boundary conditions corresponding to perfect electric conductors. Furthermore, when isotropic materials are considered (as done almost everywhere throughout this dissertation), the system matrix is symmetric and (3.1.1) can recast in

$$\begin{bmatrix} A_{\Gamma\Gamma} & A_{\Gamma 1} & A_{\Gamma 2} \\ A_{\Gamma 1}^T & A_{11} & \\ A_{\Gamma 2}^T & & A_{22} \end{bmatrix} \begin{bmatrix} x_\Gamma \\ x_1 \\ x_2 \end{bmatrix} = \begin{bmatrix} B_\Gamma \\ \\ \end{bmatrix}. \tag{3.1.2}$$

The system of (3.1.2) can now be solved exploiting the Schur complement concept:

- Assemble the Schur complement matrix $[S] = [A_{\Gamma\Gamma}] - \sum_{j=1}^{2} \left[A_{\Gamma j}\right] \left[A_{jj}\right]^{-1} \left[A_{\Gamma j}\right]^T$ and the relative right-hand side $[G] = [B_\Gamma]$,

- Solve the Schur complement system $[x_\Gamma] = [S]^{-1}[G]$,
- Recover for the internal unknowns $\left[x_j\right] = \left[A_{jj}\right]^{-1}(-\left[A_{\Gamma j}\right]^T[x_\Gamma])$.

In the first step, a matrix denser than the original $[A_{\Gamma\Gamma}]$ is assembled upon adding (as done for the global finite element matrix after the computation of an element matrix) the contributions of each subdomain. This requires the computation of $\left[A_{jj}\right]^{-1}$ (intrinsically dense), which itself can be handled easily with sparse direct solvers (and exploiting symmetries in this case), however, the computation of the matrix-matrix product $\left[A_{jj}\right]^{-1}\left[A_{\Gamma j}\right]^T$ may lead to a memory consuming result. Hence, one should consider making the most of $\left[A_{\Gamma j}\right]^T$ sparsity to reduce the resulting rectangular matrix, avoiding to save into memory its null column vectors.

The second step corresponds to the inversion of a dense $[S]$ matrix. As it is known, this operation has an asymptotic complexity of $O(N_\Gamma^3)$, which indeed increases as the number of subdomains is increased. In fact, the unknowns on the boundary between subdomains increases. One may solve the problem on boundaries with a Krylov subspace iterative solver, preconditioning it with a *thresholded incomplete LU* factorization [129] or the *incomplete Cholesky* factorization which takes the advantage of matrix symmetry. In fact, it has been proved [46] that if the original system is symmetric, then the Schur complement matrix will also be symmetric.

The last step requires subdomains matrices inversion. These can be stored in memory (non-volatile preferably) during the first step where they were also used. An additional matrix-vector product has to be computed.

The resulting concatenated solution vector $[x]_{\text{Schur}} = [x_\Gamma\ x_1\ x_2]^T$ is equal, within numerical error, to that of the direct solution of the whole system in (3.1.2) when direct or iterative solvers are ran up to numerical precision. Furthermore, the parallelization internal to the first and the last steps is immediate.

In our treatment, several critical points have emerged from the use the Schur complement method, when looking forward to analyze large problems

- The assembly of the Schur complement matrix requires the computation of large rectangular matrices $\left[A_{jj}\right]^{-1}\left[A_{\Gamma j}\right]^T$. One may assemble the whole Schur complement to domain Ω_j, $\left[A_{\Gamma j}\right]\left[A_{jj}\right]^{-1}\left[A_{\Gamma j}\right]^T$, upon exploiting the sparsity of $\left[A_{\Gamma j}\right]^T$ and considering a few columns at a time in order to reduce the overall memory fill-in. However, if the number of unknowns pertaining to Ω_j is very large, then this step might result to be excessively time demanding.
- The overall Schur complement matrix $[S]$ is dense, and the complexity of its inversion grows dramatically with the boundary unknowns, and, consequently, with the number of subdomains.

Both the previous points are in contrast: if one tries to alleviate the computation of the Schur complement matrices to each subdomain by increasing the number of

subdomains (hence reducing the related domain unknowns number), then the inversion of the overall Schur complement matrix results hampered by an increase of the boundary unknowns and *viceversa*. This has led to the research of an appropriate Schur complement based domain decomposition preconditionner to be used in an iterative solver for the whole problem (3.1.2).

In contrast with the method that will be introduced in the next section, Schur complement based methods are referred to as "primal" iterative substructuring methods in the way they employ only functions in the space of the unknown global function to enforce the continuity between subdomains. For instance, continuity between the subspaces spanned in each subdomain without its boundaries is enforced by a discrete version of the Steklov-Poicaré operator or "Dirichlet-to-Neumann" map [46], the Schur complement matrix, serving as a mean for continuity of the values and the normal derivatives at the boundaries.

3.2 Finite Element Tearing and Interconnecting Dual Primal domain decomposition

Finite element tearing and interconnecting methods where first introduced in 1991 for solving a computational mechanics problem [140]. These methods are based on the solution of the subdomains problems with their boundary conditions (tearing) and solving the problem at the boundaries with Lagrange multipliers (interconnecting), the coarse problem which enforces through algebraic constraints the continuity of the global solution at subdomain boundaries. The space spanned by the sough function corresponds to "primal" unknowns while the space spanned by the boundary constrains corresponds to "dual" unknowns.

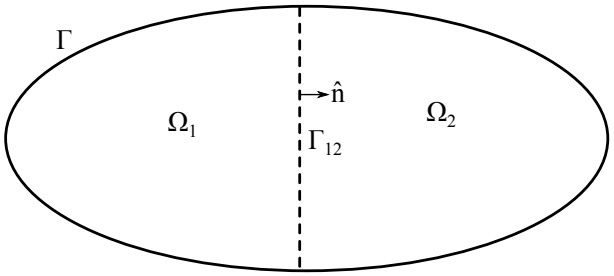

Figure 3.3: FETI-DP based domain decomposition sketch for two subdomains.

Let us consider the problem depicted by Fig. 3.3. We seek to solve the following distinct boundary value problems defined as

$$
\begin{cases}
\nabla \times \dfrac{1}{\mu_r} \nabla \times \mathbf{E}^1 + jk_0\zeta_0\sigma\mathbf{E}^1 - k_0^2\epsilon_r\mathbf{E}^1 = 0, & \text{in } \Omega_1, \\
\hat{\mathbf{n}} \times (\mathbf{E}^1 \times \hat{\mathbf{n}}) = 0, & \text{on } \Gamma_E \cap d\Omega_1, \\
\hat{\mathbf{n}} \times (\mathbf{H}^1 \times \hat{\mathbf{n}}) = 0, & \text{on } \Gamma_H \cap d\Omega_1, \\
\hat{\mathbf{n}} \times \mathbf{H}^1 = \dfrac{1}{Z_s}\hat{\mathbf{n}} \times \hat{\mathbf{n}} \times \mathbf{E}^1 + \hat{\mathbf{n}} \times \mathbf{H}^{inc} - \dfrac{1}{Z_s}\hat{\mathbf{n}} \times \hat{\mathbf{n}} \times \mathbf{E}^{inc}, & \text{on } \Gamma_R \cap d\Omega_1, \\
\hat{\mathbf{n}} \times \mathbf{H}_t^{1,k} = \dfrac{1}{Z_k}\hat{\mathbf{n}} \times \hat{\mathbf{n}} \times \mathbf{E}_t^{1,k} - \dfrac{2}{Z_k}\hat{\mathbf{n}} \times \hat{\mathbf{n}} \times \mathbf{E}_t^{k\ inc}, & \text{on } \Gamma_{WG}^k \cap d\Omega_1, \\
\hat{\mathbf{n}} \times \dfrac{1}{\mu_r} \nabla \times \mathbf{E}^1 - jk_0\ \hat{\mathbf{n}} \times \mathbf{E}^1 \times \hat{\mathbf{n}} = & \\
\qquad -\hat{\mathbf{n}} \times \dfrac{1}{\mu_r} \nabla \times \mathbf{E}^2 - jk_0\ \hat{\mathbf{n}} \times \mathbf{E}^2 \times \hat{\mathbf{n}}, & \text{on } \Gamma_{12} \cap d\Omega_1,
\end{cases}
\tag{3.2.1}
$$

and

$$
\begin{cases}
\nabla \times \dfrac{1}{\mu_r} \nabla \times \mathbf{E}^2 + jk_0\zeta_0\sigma\mathbf{E}^2 - k_0^2\epsilon_r\mathbf{E}^2 = 0, & \text{in } \Omega_2, \\
\hat{\mathbf{n}} \times (\mathbf{E}^2 \times \hat{\mathbf{n}}) = 0, & \text{on } \Gamma_E \cap d\Omega_2, \\
\hat{\mathbf{n}} \times (\mathbf{H}^2 \times \hat{\mathbf{n}}) = 0, & \text{on } \Gamma_H \cap d\Omega_2, \\
\hat{\mathbf{n}} \times \mathbf{H}^2 = \dfrac{1}{Z_s}\hat{\mathbf{n}} \times \hat{\mathbf{n}} \times \mathbf{E}^2 + \hat{\mathbf{n}} \times \mathbf{H}^{inc} - \dfrac{1}{Z_s}\hat{\mathbf{n}} \times \hat{\mathbf{n}} \times \mathbf{E}^{inc}, & \text{on } \Gamma_R \cap d\Omega_2, \\
\hat{\mathbf{n}} \times \mathbf{H}_t^{2,k} = \dfrac{1}{Z_k}\hat{\mathbf{n}} \times \hat{\mathbf{n}} \times \mathbf{E}_t^{2,k} - \dfrac{2}{Z_k}\hat{\mathbf{n}} \times \hat{\mathbf{n}} \times \mathbf{E}_t^{k\ inc}, & \text{on } \Gamma_{WG}^k \cap d\Omega_2, \\
\hat{\mathbf{n}} \times \dfrac{1}{\mu_r} \nabla \times \mathbf{E}^2 - jk_0\ \hat{\mathbf{n}} \times \mathbf{E}^2 \times \hat{\mathbf{n}} = & \\
\qquad -\hat{\mathbf{n}} \times \dfrac{1}{\mu_r} \nabla \times \mathbf{E}^1 - jk_0\ \hat{\mathbf{n}} \times \mathbf{E}^1 \times \hat{\mathbf{n}}, & \text{on } \Gamma_{21} \cap d\Omega_2,
\end{cases}
\tag{3.2.2}
$$

where the superscript on the fields $i \in \{1, 2\}$ correspond to the fields spanned in the i^{th} domain (Ω_i) and $d\Omega_i$ is the whole boundary of Ω_i. $\hat{\mathbf{n}}$ is chosen, as done previously, to be outwardly directed from the subproblem domain. Notice that, in the conditions on Γ_R, if the incident fields vanish, the condition resorts to the classical absorbing boundary condition (2.3.4). The last boundary condition in each problem corresponds the *Robin-Robin transmission condition*, pioneered by Després in 1991 [141, 142], proving the convergence in an iterative solution of the coarse problem. In fact, direct imposition of the continuity of the tangential components of electric and magnetic fields may lead to internal resonances within subdomain problems, and the overall system matrix (see later) could be ill conditioned and hence may suffer from slow convergence or even fail to converge.

Let $\mathcal{W}_E^1$ and $\mathcal{W}_E^2$ be the $\mathcal{H}(\text{curl})$-conforming space spanning the electric field solution such that

$$\mathcal{W}_E^1 := \{\mathbf{w} \in \mathcal{H}(\text{curl}, \Omega_1, \Gamma_E) \mid \hat{\mathbf{n}} \times \mathbf{w} = 0 \text{ on } \Gamma_E\},$$
$$\mathcal{W}_E^2 := \{\mathbf{w} \in \mathcal{H}(\text{curl}, \Omega_2, \Gamma_E) \mid \hat{\mathbf{n}} \times \mathbf{w} = 0 \text{ on } \Gamma_E\},$$

and $\mathcal{H}(\text{curl}, \Omega, \Gamma_E) =\equiv \mathcal{H}(\text{curl}, \Omega_1, \Gamma_E) \times \mathcal{H}(\text{curl}, \Omega_2, \Gamma_E)$. The Galerkin framework leads to the following weak form

$$\int_{\Omega_1} \nabla \times \mathbf{w}_i^* \cdot \frac{1}{\mu_r} \nabla \times \mathbf{E}^1 \, d\Omega + jk_0\zeta_0 \int_{\Omega_1} \mathbf{w}_i^* \cdot \sigma \mathbf{E}^1 \, d\Omega - k_0^2 \int_{\Omega_1} \mathbf{w}_i^* \cdot \epsilon_r \mathbf{E}^1 \, d\Omega + \int_{d\Omega_1} \mathbf{w}_i^* \cdot \hat{\mathbf{n}} \times \frac{1}{\mu_r} \nabla \times \mathbf{E}^1 \, d\Gamma = 0, \qquad \forall \mathbf{w}_i \in \mathcal{W}_E^1, \quad (3.2.3)$$

and for the second subdomain

$$\int_{\Omega_2} \nabla \times \mathbf{w}_i^* \cdot \frac{1}{\mu_r} \nabla \times \mathbf{E}^2 \, d\Omega + jk_0\zeta_0 \int_{\Omega_2} \mathbf{w}_i^* \cdot \sigma \mathbf{E}^2 \, d\Omega - k_0^2 \int_{\Omega_2} \mathbf{w}_i^* \cdot \epsilon_r \mathbf{E}^2 \, d\Omega + \int_{d\Omega_2} \mathbf{w}_i^* \cdot \hat{\mathbf{n}} \times \frac{1}{\mu_r} \nabla \times \mathbf{E}^2 \, d\Gamma = 0, \qquad \forall \mathbf{w}_i \in \mathcal{W}_E^2. \quad (3.2.4)$$

The integrals on $d\Omega_1$ and $d\Omega_2$ take into account all the "classical" boundary conditions seen in chapter 2, in particular Γ_R and Γ_{WG} which allow to excite the finite element domain. On Γ_{12} and Γ_{21}, we introduce a coupling term in order to allow the boundary values to vary, enforcing in such a way the continuity of the function between adjacent subdomains. For instance,

$$\int_{\Gamma_{12}} \mathbf{w}_i^* \cdot \hat{\mathbf{n}} \times \frac{1}{\mu_r} \nabla \times \mathbf{E}^1 \, d\Gamma, \quad (3.2.5)$$

$$\int_{\Gamma_{21}} \mathbf{w}_i^* \cdot \hat{\mathbf{n}} \times \frac{1}{\mu_r} \nabla \times \mathbf{E}^2 \, d\Gamma, \quad (3.2.6)$$

are non-null quantities on, respectively, Γ_{12} and Γ_{21}. We consequently introduce, to simplify our treatment, fictitious variables $\mathbf{j}^1$ and $\mathbf{j}^2$, defined as

$$\mathbf{j}^1 = \frac{1}{k_0} \hat{\mathbf{n}} \times \frac{1}{\mu_r} \nabla \times \mathbf{E}^1, \quad (3.2.7)$$

$$\mathbf{j}^2 = \frac{1}{k_0} \hat{\mathbf{n}} \times \frac{1}{\mu_r} \nabla \times \mathbf{E}^2, \quad (3.2.8)$$

which correspond to the dual unknowns used as Lagrange multipliers in the FETI-DP algorithm. Let $\mathcal{V}_J^i$ be the spanning space for boundary constraints $\mathbf{v}$ on $\Gamma_{ij}, i, j \in \{1, 2 \mid i \neq j\}$, such that

$$\mathcal{V}_J^i := \{\mathbf{v} \in \mathcal{H}(\text{curl}, \Gamma_{ij})\},$$

and

$$\mathbf{j}^1 := \sum_{l=1}^{N^1} \lambda_j \mathbf{v}_j^1, \qquad \mathbf{v}_j^1 \in \mathcal{V}_J^1,$$

$$\mathbf{j}^2 := \sum_{l=1}^{N^2} \lambda_j \mathbf{v}_j^2, \qquad \mathbf{v}_j^2 \in \mathcal{V}_J^2.$$

Finally, the coupling terms in the Galerkin projections on each subdomain, respectively (3.2.5) and (3.2.6), can be written as

$$\int_{\Gamma_{12}} \mathbf{w}_i^* \cdot k_0\, \mathbf{j}^1\, d\Gamma = \sum_{l=1}^{N^1} \lambda_j k_0 \int_{\Gamma_{12}} \mathbf{w}_i^* \cdot \mathbf{v}_j\, d\Gamma, \quad \forall \mathbf{w}_i \in \mathcal{W}_E^1, \mathbf{v}_j \in \mathcal{V}_J^1, \quad (3.2.9)$$

$$\int_{\Gamma_{21}} \mathbf{w}_i^* \cdot k_0\, \mathbf{j}^2\, d\Gamma = \sum_{l=1}^{N^2} \lambda_j k_0 \int_{\Gamma_{21}} \mathbf{w}_i^* \cdot \mathbf{v}_j\, d\Gamma, \quad \forall \mathbf{w}_i \in \mathcal{W}_E^2, \mathbf{v}_j \in \mathcal{V}_J^2. \quad (3.2.10)$$

The Robin-Robin transmission conditions can also be written as

$$\begin{cases} jk_0\, \mathbf{j}^1 + k_0\, \hat{\mathbf{n}} \times \mathbf{E}^1 \times \hat{\mathbf{n}} = -jk_0\, \mathbf{j}^2 + k_0\, \hat{\mathbf{n}} \times \mathbf{E}^2 \times \hat{\mathbf{n}}, & \text{on } \Gamma_{12} \cap d\Omega_1, \\ jk_0\, \mathbf{j}^2 + k_0\, \hat{\mathbf{n}} \times \mathbf{E}^2 \times \hat{\mathbf{n}} = -jk_0\, \mathbf{j}^1 + k_0\, \hat{\mathbf{n}} \times \mathbf{E}^1 \times \hat{\mathbf{n}}, & \text{on } \Gamma_{21} \cap d\Omega_2, \end{cases} \quad (3.2.11)$$

where we have multiplied both sides of the equations by j to achieve a better conditioning of the resulting matrices.
To introduce coupling between subdomains, further Galerkin projections are performed by testing the transmission conditions with $\mathbf{v}_i \in \mathcal{V}_J^1$ for the first subproblem and $\mathbf{v}_i \in \mathcal{V}_J^2$ for the second one. As a result,

$$jk_0 \int_{\Gamma_{12}} \mathbf{v}_i^* \cdot \mathbf{j}^1\, d\Gamma + k_0 \int_{\Gamma_{12}} \mathbf{v}_i^* \cdot \hat{\mathbf{n}} \times \mathbf{E}^1 \times \hat{\mathbf{n}}\, d\Gamma = - jk_0 \int_{\Gamma_{12}} \mathbf{v}_i^* \cdot \mathbf{j}^2\, d\Gamma + k_0 \int_{\Gamma_{12}} \mathbf{v}_i^* \cdot \hat{\mathbf{n}} \times \mathbf{E}^2 \times \hat{\mathbf{n}}\, d\Gamma, \quad \forall \mathbf{v}_i \in \mathcal{V}_J^1, \quad (3.2.12)$$

for the problem in Ω_1 and

$$jk_0 \int_{\Gamma_{21}} \mathbf{v}_i^* \cdot \mathbf{j}^2\, d\Gamma + k_0 \int_{\Gamma_{21}} \mathbf{v}_i^* \cdot \hat{\mathbf{n}} \times \mathbf{E}^2 \times \hat{\mathbf{n}}\, d\Gamma = - jk_0 \int_{\Gamma_{21}} \mathbf{v}_i^* \cdot \mathbf{j}^1\, d\Gamma + k_0 \int_{\Gamma_{21}} \mathbf{v}_i^* \cdot \hat{\mathbf{n}} \times \mathbf{E}^1 \times \hat{\mathbf{n}}\, d\Gamma, \quad \forall \mathbf{v}_i \in \mathcal{V}_J^2, \quad (3.2.13)$$

on Ω_2.

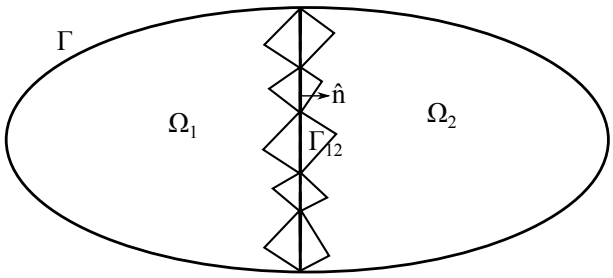

Figure 3.4: Conforming domain decomposition sketch for two subdomains.

Throughout this dissertation, the mesh is assumed to be conforming between adjacent domains, that is, all the elements at the boundaries are connected at their nodes as depicted in Fig. 3.4. The choice of $\mathbf{v} = \hat{\mathbf{n}} \times \mathbf{w}$ has resulted, in terms of simplicity and convergence speed, the best choice. $\mathbf{v} = \hat{\mathbf{n}} \times \mathbf{w} \times \hat{\mathbf{n}}$ led to slower

convergence in the iterative FETI-DP solution. The previous weak forms lead to the following systems

$$\begin{bmatrix} A_{11} & A_{\Gamma_1 1} & \\ A_{\Gamma_1 1}^T & A_{\Gamma_1\Gamma_1} & D_{11} \\ & D_{11}^T & T_{11} \end{bmatrix} \begin{bmatrix} x_1 \\ x_{\Gamma_1} \\ \lambda_1 \end{bmatrix} = \begin{bmatrix} B_1 \\ B_{\Gamma_1} \\ \end{bmatrix} + \begin{bmatrix} & & \\ & & \\ D_{12} & -T_{12} \end{bmatrix} \begin{bmatrix} B_2 \\ x_{\Gamma_2} \\ \lambda_2 \end{bmatrix}, \tag{3.2.14}$$

for the first subproblem and

$$\begin{bmatrix} A_{22} & A_{\Gamma_2 2} & \\ A_{\Gamma_2 2}^T & A_{\Gamma_2\Gamma_2} & D_{22} \\ & D_{22}^T & T_{22} \end{bmatrix} \begin{bmatrix} x_2 \\ x_{\Gamma_2} \\ \lambda_1 \end{bmatrix} = \begin{bmatrix} B_2 \\ B_{\Gamma_2} \\ \end{bmatrix} + \begin{bmatrix} & & \\ & & \\ D_{21} & -T_{21} \end{bmatrix} \begin{bmatrix} \\ x_{\Gamma_1} \\ \lambda_1 \end{bmatrix}, \tag{3.2.15}$$

for the second one. The block matrices $[A_{\Omega\Omega}]$, $\left[A_{\Gamma_\Omega\Omega}\right]$ are $\left[A_{\Gamma_\Omega\Gamma_\Omega}\right]$ those computed as in section 3.1. The last block $[D_{\Gamma\Gamma}]$ is the one that is retrieved by the coupling term integrals of (3.2.5) and (3.2.6). The last row of block-matrices is retrieved by the testing of the transmission conditions (3.2.11) with the dual shape functions $\mathbf{v}$. Explicitly, we have

$$\begin{aligned} D_{mm} &= k_0 \int_{\Gamma_{mn}} \mathbf{v}_i^{m*} \cdot \hat{\mathbf{n}} \times \mathbf{w}_j^m \times \hat{\mathbf{n}}\, d\Gamma, \\ T_{mm} &= jk_0 \int_{\Gamma_{mn}} \mathbf{v}_i^{m*} \cdot \mathbf{v}_j^m\, d\Gamma, \\ D_{mn} &= k_0 \int_{\Gamma_{mn}} \mathbf{v}_i^{m*} \cdot \hat{\mathbf{n}} \times \mathbf{w}_j^n \times \hat{\mathbf{n}}\, d\Gamma, \\ T_{mn} &= jk_0 \int_{\Gamma_{mn}} \mathbf{v}_i^{m*} \cdot \mathbf{v}_j^n\, d\Gamma. \end{aligned}$$

The systems of (3.2.14) and (3.2.15) can be solved directly in an alternating fashion within an iterative procedure. Starting from null solution vectors for each subdomain, $[x]_1 = \left[x_1\ x_{\Gamma_1}\ \lambda_1\right]^T$ and $[x]_2 = \left[x_2\ x_{\Gamma_2}\ \lambda_2\right]^T$, the procedure is expressed by the algorithm 1.

One can also restrict the iterative procedure to the dual-primal unknowns. First a restriction matrix (boolean matrix) $[R]_1$ is built as

$$[R]_1 = \begin{bmatrix} & I_{P_1} & \\ & & I_{D_1} \end{bmatrix},$$

where $\left[I_{P_1}\right]$ and $\left[I_{D_1}\right]$ are unitary matrices of the size, respectively, of the number of primal and dual unknowns. Notice that the sizes might be different if Γ_E crosses the boundary Γ_{12}. Than, the solution process is changed upon apply restriction to the

Algorithm 1 Domain-wise FETI-DP solution procedure.

$[x]_1^0 \leftarrow 0$
$[x]_2^0 \leftarrow 0$
$k \leftarrow 1$
$err \leftarrow 1$
while $err \geq maxerr$ **do**
  $[x]_1^k \leftarrow$ Solve (3.2.14)
  $[x]_2^k \leftarrow$ Solve (3.2.15)
  $err \leftarrow \max\left(\frac{\|[x]_1^k - [x]_1^{k-1}\|}{\|[x]_1^k\|}, \frac{\|[x]_2^k - [x]_2^{k-1}\|}{\|[x]_2^k\|}\right)$
  $k \leftarrow k+1$
end while

subdomains solution vectors

$$\begin{bmatrix} x_{\Gamma_1} \\ \lambda_1 \end{bmatrix} = [R]_1 \begin{bmatrix} x_1 \\ x_{\Gamma_1} \\ \lambda_1 \end{bmatrix} = [R]_1 \begin{bmatrix} A_{11} & A_{\Gamma_1 1} & \\ A_{\Gamma_1 1}^T & A_{\Gamma_1\Gamma_1} & D_{11} \\ & D_{11}^T & T_{11} \end{bmatrix}^{-1} \left(\begin{bmatrix} B_1 \\ B_{\Gamma_1} \\ \end{bmatrix} + \begin{bmatrix} & & \\ & D_{12} & -T_{12} \end{bmatrix} \begin{bmatrix} x_{\Gamma_2} \\ \lambda_2 \end{bmatrix} \right) = \underbrace{[R]_1 \begin{bmatrix} A_{11} & A_{\Gamma_1 1} & \\ A_{\Gamma_1 1}^T & A_{\Gamma_1\Gamma_1} & D_{11} \\ & D_{11}^T & T_{11} \end{bmatrix}^{-1}}_{(1)} \left(\begin{bmatrix} B_1 \\ B_{\Gamma_1} \\ \end{bmatrix} + \begin{bmatrix} & & \\ D_{12} & -T_{12} \end{bmatrix} \begin{bmatrix} x_{\Gamma_2} \\ \lambda_2 \end{bmatrix} \right). \quad (3.2.16)$$

Analogous matrices are computed for the second subproblem upon performing the changes in the subscripts $2 \rightarrow 1$ and $1 \rightarrow 2$. Notice that restriction matrices may result different for the second subproblem. The matrix factor (1) lead to a small rectangular matrix (the row size is as the number of primal and dual unknowns on the boundaries) but dense due to matrix inversion. Once the procedure converged, the whole solution can be recovered by the solution of (3.2.14) and (3.2.15) where the dual and primal unknowns of the coarse problem provide the correct boundary conditions for continuity.

Several works[47, 143–145] have exploited the repetition of subdomains problems such as in finite periodic analyzes to considerably reduce the amount of matrices factors to compute. However, as we seek for the solution of arbitrarily shaped problems, the construction of many dense matrices may not be profitable. Hence, the path of constructing domain decomposition based preconditioners for Krylov subspace iterative solvers have been taken, as will be shown in the next sections. For this purpose, we formulate the global FETI-DP system to be solved with an iterative method as, collecting both systems (3.2.14) and (3.2.15) in a single global system,

$$\begin{bmatrix} A_{11} & A_{\Gamma_1 1} & & & & \\ A_{\Gamma_1 1}^T & A_{\Gamma_1\Gamma_1} & D_{11} & & & \\ & D_{11}^T & T_{11} & & -D_{12} & T_{12} \\ & & & A_{22} & A_{\Gamma_2 2} & \\ & & & A_{\Gamma_2 2}^T & A_{\Gamma_2\Gamma_2} & D_{22} \\ & & -D_{21} & T_{21} & D_{22}^T & T_{22} \end{bmatrix} \begin{bmatrix} x_1 \\ x_{\Gamma_1} \\ \lambda_1 \\ x_2 \\ x_{\Gamma_2} \\ \lambda_2 \end{bmatrix} = \begin{bmatrix} \\ B_{\Gamma_1} \\ \\ \\ B_{\Gamma_2} \\ \end{bmatrix}. \tag{3.2.17}$$

3.3 Domain decomposition based preconditioners for Krylov subspace iterative solvers

In this section, we present the Krylov subspace iterative solvers which exploit the optimality properties of projections (on Krylov spaces) during the iterative search process of the solution, with a deep control on the residual error (with error bounds) [125]. In particular, we have employed the *restarted-Generalized Minimum Residual* (GMRES(r)) which finds the steepest descent upon applying projections in the residual norm between successive refinements of the solution. Its restarted approach is such that the basis vectors spanning the solution is restricted to a given number r, allowing to save memory requirements. Of course, the retarded version leads to different results respectively to the non-restarted version, as the whole projection bases are reset after r iterations, and the next iteration cycle may start with a higher residual error.

3.3.1 Restarted-Generalized Minimum Residual

A general projection method for solving a linear system

$$[A][x] = [b],$$

extracts an approximate solution $[x]_m$ from an affine subspace $[x]_0 + \mathcal{K}_m$ of dimension m by imposing the Petrov-Galerkin condition

$$[b] - [A][x]_m \perp \mathcal{L}_m$$

where $[\mathcal{L}]_m$ is another subspace of dimension m. $[x]_0$ is an initial guess to the solution. A Krylov subspace method is such that

$$\mathcal{K}_m([A], [r]_0) = \text{span}\{[r]_0, [A][r]_0, [A]^2[r]_0, \ldots, [A]^{m-1}[r]_0\}$$

where $[r]_0 = [b] - [A][x]_0$ is the residual. The vectors spanning $\mathcal{K}_m([A], [r]_0)$ might be almost linearly dependent. Thus, an appropriate orthonormalization is employed to build a Krylov subspace basis $[V]_m = \text{span}\{[v]_1, \ldots, [v]_m\}$, the *Arnoldi-Modified Gram-Schmidt* algorithm 2. The Arnoldi process produces and $\mathbb{R}^{m+1\times m}$ upper Hessenberg matrix $[H]_m$, coefficients for the expansion of $[A]$ such that

$$[A][V]_m = [V]_{m+1}[H]_m \tag{3.3.1}$$

Algorithm 2 Arnoldi-Modified Gram-Schmidt.

Choose a vector $[v]_1$ such that $\|[v]_1\|_2 = 1$
for j $= 1, \ldots,$ m **do**
  $[w]_j \leftarrow [A][v]_j$
  for i $= 1, \ldots,$ j **do**
    $h_{i,j} \leftarrow < [w]_j, [v]_i >$
    $[w]_j \leftarrow [w]_j - h_{i,j}[v]_i$
  end for
  $h_{j+1,j} \leftarrow \|[w]_j\|_2$
  if $h_{j+1,j} = 0$ **then**
    Break
  end if
  $[v]_{j+1} \leftarrow \frac{[w]_j}{h_{j+1,j}}$
end for

Any vector $[x] \in [x]_0 + \mathcal{K}_m$ can be now written as

$$[x] = [x]_0 + [V]_m [y]$$

where $[y]$ is a vector of dimension m. Defining

$$J([y]) = \|[b] - [A][x]\|_2 = \|[b] - [A]([x]_0 + [V]_m [y])\|_2,$$

the relation (3.3.1) results in

$$\begin{aligned} [b] - [A][V]_m &= [b] - A([x]_0 + [V]_m [y]), \\ &= [r]_0 - [A][V]_m [y], \\ &= \beta [v]_1 - [V]_{m+1} [H]_m [y], \\ &= [V]_{m+1} (\beta [e]_1 - [H]_m [y]). \end{aligned}$$

with $\beta = \|[r]_0\|_2$ and $[v]_1 = [r]_0/\beta$ is the first vector of unitary norm chose in the first step of the algorithm 2, and $[V]_m^T [r]_0 = [V]_m^T (\beta [v]_1) = \beta [e]_1$ with $[e]_1 = [1\ 0\ \ldots\ 0]^T$ is the first standard basis vector. Since the column-vectors spanning $[V]_{m+1}$ are orthonormal, then

$$J([y]) = \|[b] - [A]([x]_0 + [V]_m [y])\|_2 = \|\beta [e]_1 - [H]_m [y]\|_2.$$

The GMRES [146] (not yet restarted) approximation is the unique vector of $[x]_0 + \mathcal{K}_m$ which minimizes $J([y])$. The approximation is obtained as

$$[x]_m = [x]_0 + [V]_m [y]_m,$$

where

$$[y]_m = \text{argmin}_y \|\beta [e]_1 - [H]_m [y]\|_2.$$

Algorithm 3 Restarted-Generalized Minimum Residual.

while $\beta = \|[r]_0\|_2 \geq maxerr$ with $[r]_0 = [b] - A([x]_0$, $[v]_1 = [r]_0/\beta$ **do**
  for $m = 1, \ldots, r$ **do**
    Generate the Arnoldi basis and $[H]_m$
    Compute $[y]_m$ which minimizes $\|\beta\,[e]_1 - [H]_m\,[y]\|_2$
    Compute $[x]_m = [x]_0 + [V]_m\,[y]_m$
  end for
  $[x]_0 \leftarrow [x]_m$ ▷ The new starting vector is $[x]_m$
end while

A well known difficulty with the restarted GMRES algorithm is that it can stagnate when the matrix is not positive-definite[1]. The full GMRES algorithm is guaranteed to converge in at most N steps (N the system dimensions), but this would be impractical if there were many steps required for convergence, due to large memory requirements: $O(N^2)$, similar to sparse direct solvers, whereas the restarted has only $O(rN)$ memory requirements.

A typical remedy is to use preconditioning techniques whose goal is to reduce the number of steps required to converge. Here follow two types of preconditioners: the block Jacobi and the block Gauss-Seidel. None of these involve the computation of a Schur complement matrix, as a direct assembly of this matrix and its inversion without proper approximation may lead, for very large problem, to memory bottlenecks.

3.3.2 Block Jacobi preconditioner

Let us consider the linear system of equations that leads to the following matrix system

$$\begin{bmatrix} A_{11} & A_{12} & A_{13} \\ A_{21} & A_{22} & A_{23} \\ A_{31} & A_{32} & A_{33} \end{bmatrix} \begin{bmatrix} x_1 \\ x_2 \\ x_3 \end{bmatrix} = \begin{bmatrix} b_1 \\ b_2 \\ b_3 \end{bmatrix}, \tag{3.3.2}$$

where $[A]$ is non necessarily symmetric and we have considered only a single right-hand side vector as the GMRES(r) solves for one right-hand side at a time. The block Jacobi preconditioner is defined as

$$[P]_J = \begin{bmatrix} A_{11} & & \\ & A_{22} & \\ & & A_{33} \end{bmatrix}, \tag{3.3.3}$$

[1]Certain boundary conditions (especially for radiation and waveports continuity) and materials properties may lead to non-positive-definite system matrices.

and the resulting preconditionned system is

$$\begin{bmatrix} [A_{11}]^{-1} & & \\ & [A_{22}]^{-1} & \\ & & [A_{33}]^{-1} \end{bmatrix} \begin{bmatrix} A_{11} & A_{12} & A_{13} \\ A_{21} & A_{22} & A_{23} \\ A_{31} & A_{32} & A_{33} \end{bmatrix} \begin{bmatrix} x_1 \\ x_2 \\ x_3 \end{bmatrix} = \begin{bmatrix} [A_{11}]^{-1} & & \\ & [A_{22}]^{-1} & \\ & & [A_{33}]^{-1} \end{bmatrix} \begin{bmatrix} b_1 \\ b_2 \\ b_3 \end{bmatrix}, \quad (3.3.4)$$

where we have exploited the following relation on the inversion of block diagonal matrices

$$\begin{bmatrix} A_{11} & & \\ & A_{22} & \\ & & A_{33} \end{bmatrix}^{-1} = \begin{bmatrix} [A_{11}]^{-1} & & \\ & [A_{22}]^{-1} & \\ & & [A_{33}]^{-1} \end{bmatrix}.$$

Preconditioning with $[P]_J$ is integrated in the GMRES(r) algorithm after the computation of the residual vector $[r]_m = [b] - [A]([x]_0 + [V]_m [y]) = \left[[r_1]_m \ [r_2]_m \ [r_3]_m \right]^T$ upon performing

$$\begin{aligned} [r_1]_m &\longleftarrow [A_{11}]^{-1} [r_1]_m, \\ [r_2]_m &\longleftarrow [A_{22}]^{-1} [r_2]_m, \\ [r_3]_m &\longleftarrow [A_{33}]^{-1} [r_3]_m. \end{aligned}$$

3.3.3 Block Gauss-Seidel preconditioner

Let us consider again the matrix system (3.3.2), the lower block Gauss-Seidel preconditioner is defined as

$$[P]_{GS} = \begin{bmatrix} A_{11} & & \\ A_{21} & A_{22} & \\ A_{31} & A_{32} & A_{33} \end{bmatrix}. \quad (3.3.5)$$

The inversion of the whole $[P]_{GS}$ results, in the case of symmetric Schur complement based domain decomposition, to the solution of the problem, hence at the cost of a direct solver. In any case, the computational requirements may be prohibitive for large problems. However, it can be shown that the inverse of $[P]_{GS}$

$$\begin{bmatrix} A_{11} & & \\ A_{21} & A_{22} & \\ A_{31} & A_{32} & A_{33} \end{bmatrix}^{-1} = \begin{bmatrix} [A_{11}]^{-1} & & \\ [\tilde{A_{21}}] & [A_{22}]^{-1} & \\ [\tilde{A_{31}}] & [\tilde{A_{32}}] & [A_{33}]^{-1} \end{bmatrix}, \quad (3.3.6)$$

where

$$\begin{aligned} [\tilde{A_{21}}] &= -[A_{22}]^{-1} [A_{21}] [A_{11}]^{-1}, \\ [\tilde{A_{32}}] &= -[A_{33}]^{-1} [A_{32}] [A_{22}]^{-1}, \\ [\tilde{A_{31}}] &= [A_{33}]^{-1} [A_{32}] [A_{22}]^{-1} [A_{21}] [A_{11}]^{-1} - [A_{33}]^{-1} [A_{31}] [A_{11}]^{-1}, \end{aligned}$$

can be computed sequentially on the residual vector, updating it progressively while computing the diagonal blocks inverse. Preconditioning with $[P]_{GS}$ is integrated in the GMRES(r) algorithm after the computation of the residual vector $[r]_m = [b] - [A]([x]_0 + [V]_m[y]) = \left[[r_1]_m \ [r_2]_m \ [r_3]_m\right]^T$ upon performing sequentially

$$\begin{aligned}
[r_1]_m &\longleftarrow [A_{11}]^{-1}[r_1]_m\,, \\
[r_2]_m &\longleftarrow [A_{22}]^{-1}\left([r_2]_m - [A_{21}][r_1]_m\right). \\
[r_3]_m &\longleftarrow [A_{33}]^{-1}\left([r_3]_m - [A_{31}][r_1]_m - [A_{32}][r_2]_m\right).
\end{aligned}$$

3.4 Numerical tests

In this section, we present several results on a simple test case, that of a WR-90 rectangular waveguide segment, where the mesh is partitioned in order to implement the domain decomposition formulations. First, a simple two-domains test will be performed to assess the methods without iterative solvers. Then, the performances of the preconditioners will be analyzed, also varying the number of subdomains.

3.4.1 WR-90 rectangular waveguide

The model analyzed consists of a 240 mm long $\hat{\mathbf{x}}$-directed WR-90 waveguide segment. The metallic walls are considered perfect electric conductors while the two waveports are located at the extremities in the $\hat{\mathbf{x}}$ direction. The mesh consists of 20 602 tetrahedra and has been partitioned, using Metis [124], into two parts separated by an arbitrarily shaped surface composed by faces shared by tetrahedra located in the middle of the segment. Actually, Metis divides a mesh such that the parts result to have approximately the same number of tetrahedra (10 489 and 10 113).

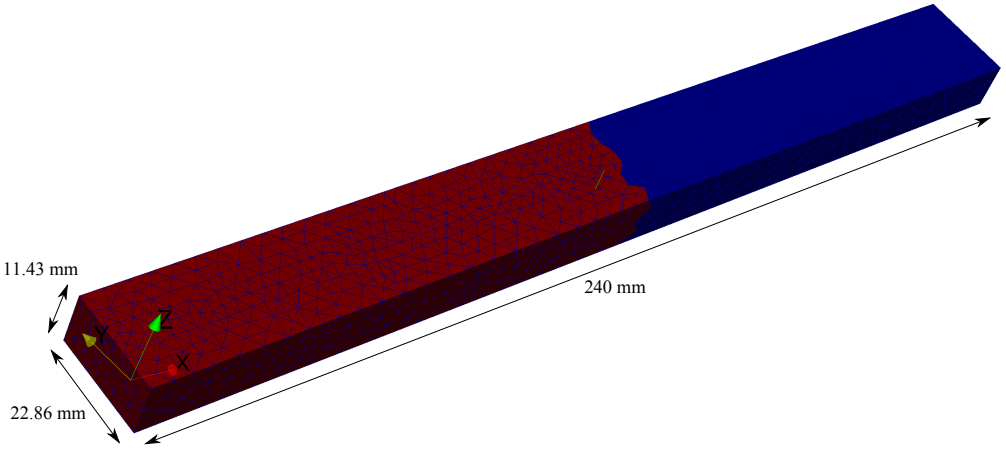

Figure 3.5: $\hat{\mathbf{x}}$-directed WR-90 waveguide segment and conformal mesh partitioning.

3.4.2 Direct analysis

The first conducted analysis is a direct solution of the whole problem upon imposing either dominant mode (DOM) or transfinite element method (TFE) on the waveports, and computing its spectral response over the mono-modal bandwidth. First order basis functions have been used to compute the scattering parameters (TE_{10}) of Fig. 3.6.

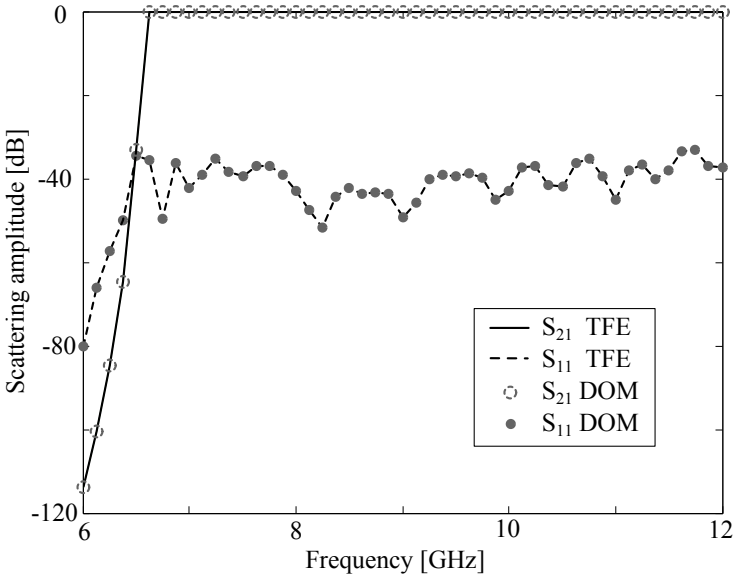

Figure 3.6: Frequency response of the WR-90 waveguide segment.

As expected, all the power is transmitted to the second port only when the frequency of excitation is higher than the cut-off frequency of 6.557 GHz for the TE_{10} mode in a WR-90. No significant differences are noticed between TFE and DOM for this frequency range. The peak memory required by the process was of about 50 MB and the times for assembly and solve of 0.7 s for each frequency point.

3.4.3 Schur complement analysis

Next, the Schur complement solution is performed. The assembled DD system matrix is shown in Fig. 3.7. The assembly timings were of about 2.5 s. While the direct solution required only 0.45 s, the Schur approach required considerably more times and memory, as reported in table 3.1. The assembly of the Schur complement matrix required approximately 10 s, due principally to the 155 column vectors of $[A_{\Gamma 1}]^T$ which have to be multiplied by the dense matrix $[A_{11}]^{-1}$. This step can be enhanced, exploiting the fact many of these column vectors are identically null. The computation of boundary unknowns is rather rapid and inexpensive for their small dimensions. The high density of the Schur complement matrix is shown in Fig. 3.8. Even if symmetries are exploited, the use of direct solvers ($O(N^3)$) would quickly lead to memory overload. The scattering parameters computed by this solution are

reported in Fig. 3.9 , as the maximum error recorded in this process has been of $\approx 10^{-12}$ in both TFE and DOM excitations.

Step	Time	Memory
$[A_{\Gamma 1}][A_{11}]^{-1}[A_{\Gamma 1}]^T$ (8557)	5.2 s	10 MB
$[A_{\Gamma 2}][A_{22}]^{-1}[A_{\Gamma 2}]^T$ (8082)	4.8 s	9.5 MB
$[x_\Gamma] = [S]^{-1}[G]$ (155)	0.002 s	$<$ 1 MB
$[x_1] = [A_{11}]^{-1}(-[A_{\Gamma 1}]^T[x_\Gamma])$	0.15 s	2 MB
$[x_2] = [A_{22}]^{-1}(-[A_{\Gamma 2}]^T[x_\Gamma])$	0.14 s	2 MB

Table 3.1: Direct Schur solution times and memory requirements.

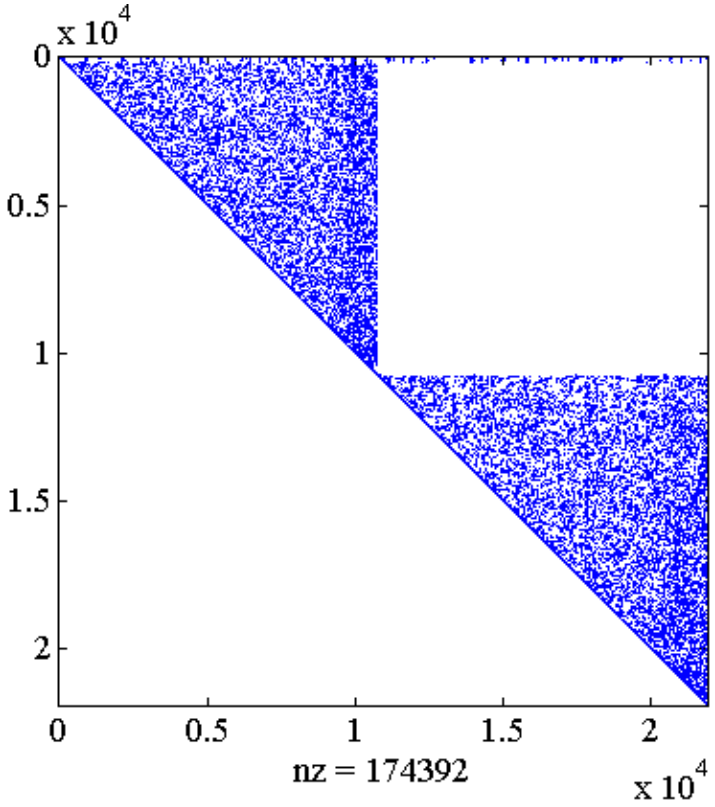

Figure 3.7: Upper triangular part of the Schur complement based domain decomposition system matrix.

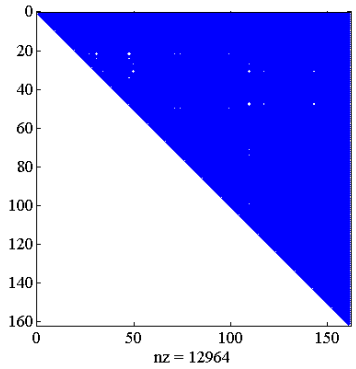

Figure 3.8: Upper triangular part of the Schur complement matrix.

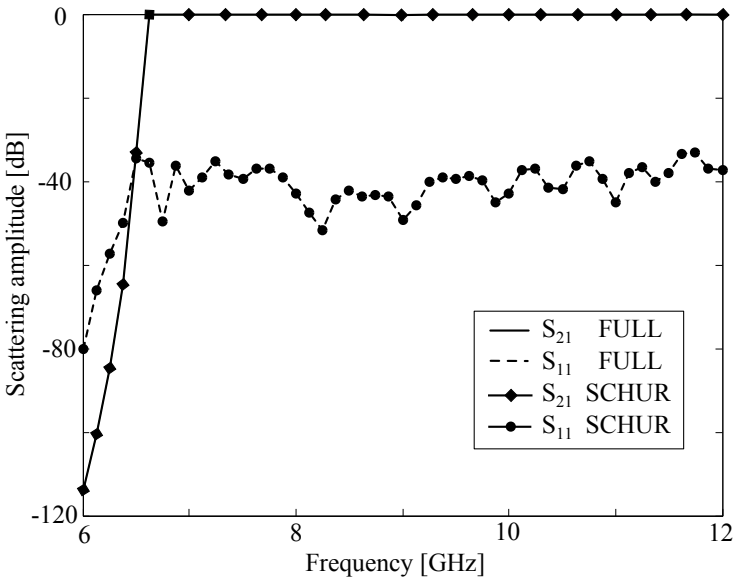

Figure 3.9: Frequency response of the WR-90 waveguide segment computed with the Schur complement algorithm.

3.4.3.1 FETI-DP analysis

We proceed with the analysis employing the FETI-DP algorithm in his version restricted to dual-primal unknowns. The global matrix, assembled as a whole for Fig. 3.10, is composed of a block-diagonal part which is symmetric and and non-symmetric off-diagonal blocks parts.

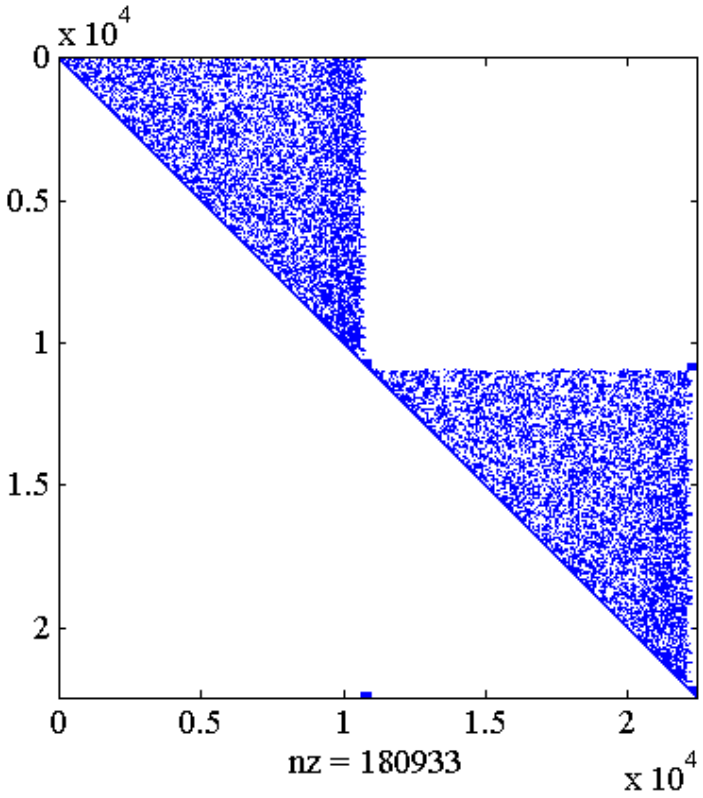

Figure 3.10: FETI-DP based domain decomposition global system matrix. The upper triangular part of the symmetric blocks are shown to enhance visibility of these parts.

The first test is performed exciting the structure with DOM at 10 GHz. The convergence history in the relative error between successive approximations of the dual-primal unknowns on the boundary is shown in Fig. 3.11. The algorithm required in the average 430 iterations ($\approx$ 200 s) to achieve an error of 10^{-2}. The spectral response, when dominant mode boundary condition on waveports is used, is depicted in Fig. 3.12. An average Euclidean error on the spectrum is of 2.1 %.

The poor convergence behavior is due to a non-optimal residual minimization. This result has motivated the use of the FETI-DP as a preconditioner for Krylov iterative solvers which not only guarantee the convergence of the solution, but somehow choose the best directions.

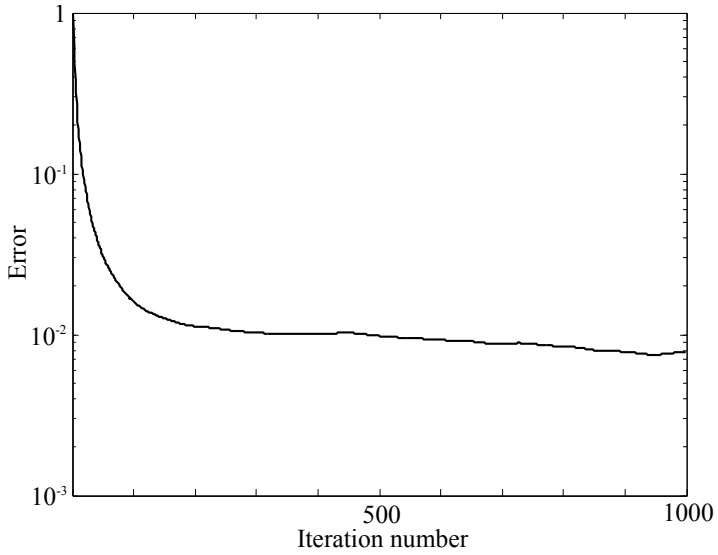

Figure 3.11: Convergence history of the restricted FETI-DP algorithm.

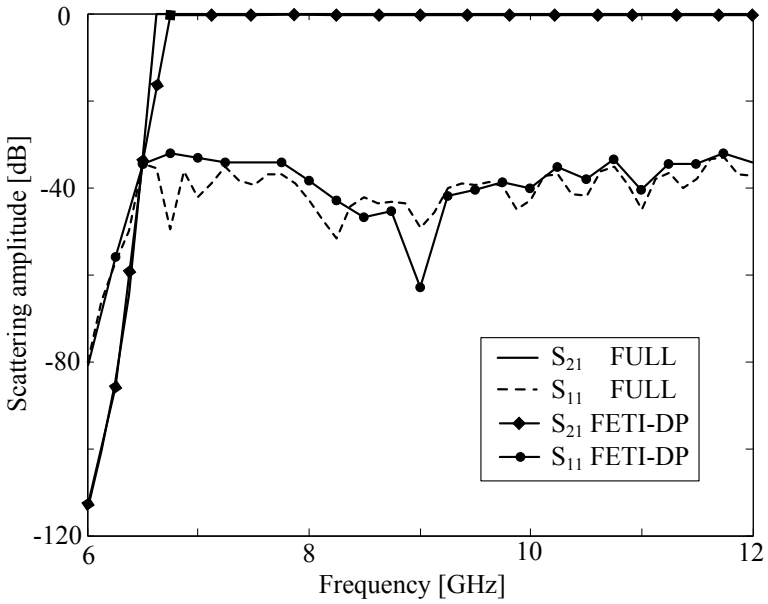

Figure 3.12: Comparison of the frequency response computed with direct full-domain solution and restricted FETI-DP (dominant mode waveports).

3.4.4 DD preconditioned GMRES(r)

One of the main advantage of iterative solvers, when convergence is guaranteed, is the possibility to achieve approximate solutions within a prescribe tolerance. In many practical applications, the gaps between the CAD model, virtual, and the realized model are such that their electromagnetic behaviors differ of some "realization tolerances". Hence, it may not be necessary to achieve numerical precision for acceptable simulation results. The numerical solution tolerance may be limited to one or a couple of magnitude orders lower to keep relatively good agreement with the real model.

Direct solvers might be used in single precision to decrease computational resources demand, but they still suffer from quadratic complexity for sparse matrices. One may also use an iterative solver, limiting the residual (error) norm to the desired tolerance. However the convergence speed, and hence the number of iterations and the overall computational times, tightly depend on the conditioning of the system matrix. It is also known that the conditioning gets worse as the problem gets larger. Adequate preconditioning of large problems matrices has to be performed in order to tackle iterative solutions in relatively acceptable amount of times. We will see that, due to block-matrix form of the domain decomposition systems, one can compute almost inexpensive very good preconditioners to tackle large problems.

3.4.4.1 Performances of the various preconditioners

To compare the performances of preconditioners, the WR-90 waveguide segment, partitioned in two subdomains as in Fig. 3.5, have been analyzed at 10 GHz using double precision direct solvers to invert block-diagonal matrices. The results are compared with non-preconditioned full-domain solution. A restarting size of $r = 100$ has been chosen and the residual error set to 10^{-12}.

Due to low residual error, all the simulation converge to the accuracy of a double precision sparse direct solution. This demonstrates that even the global FETI-DP problem is well posed and no energy is lost within interconnecting process (with only one interface). The effect of the restarting after 100 iterations can be appreciated on the DD-SCHUR Jacobi preconditioner run. In fact, after 100 and 200 iterations, the descent of the residual norm varies, leading for some iterations to a slower convergence.

While the full-domain non preconditioned solution required about 276 s (8459 iterations), the domain decomposition preconditioners allowed to reduce the amount of times as shown in table 3.2. The memory required by all the runs has been of about 69 MB, mainly allocated for the 100 orthonormal vectors (dense) used as Krylov space basis. In fact, all the assembled matrices required approximately 24 MB and the mesh about 10 MB.

It is clear that the Gauss-Seidel preconditioner leads to a better conditioning of

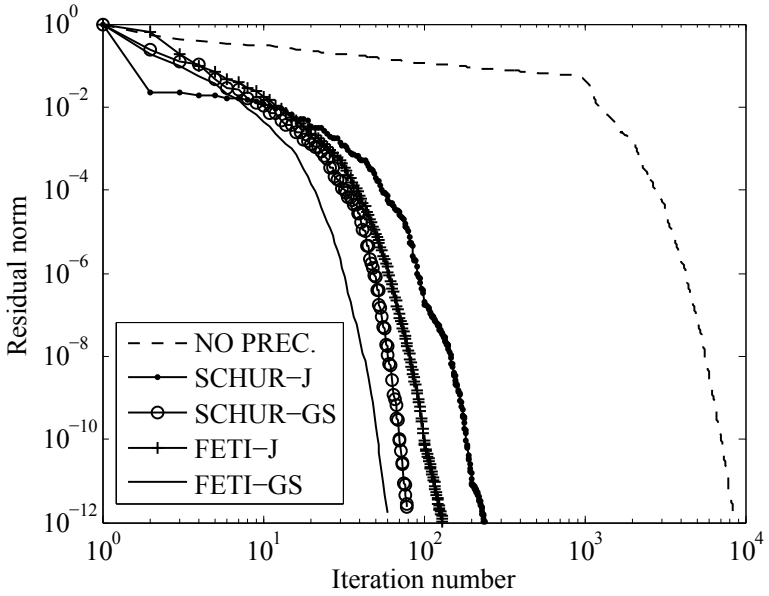

Figure 3.13: Comparison between the domain decomposition preconditioners and not preconditioned full-domain GMRES(100) solution.

Solver	Iterations	Time	Peak memory
Direct (double precision)	-	1 s	49.5 MB
No preconditioner	8459	276 s	68.2 MB
DD-Schur Jacobi precond.	238	160 s	68.6 MB
DD-Schur Gauss-Seidel precond.	78	54.5 s	69.1 MB
DD-FETI Jacobi precond.	130	90 s	69.7 MB
DD-FETI Gauss-Seidel precond.	58	41.8 s	69.2 MB

Table 3.2: Times and memory requirements for different GMRES(100) runs at 10 GHz.

the system matrix in both DD-SCHUR and DD-FETI cases. Let us analyze the performances of these solvers as the frequency of excitation varies (8, 10 and 12 GHz).

As expected [147], the condition number of the system matrices grows with the frequency, resulting in more iterations (Fig. 3.14). The FETI approach behaves clearly better that the SCHUR alternative. However, the SCHUR approach remains an invaluable method for arbitrary domain partitioning, as the transfinite element waveports boundary conditions (with better accuracy) can be straightforwardly implemented. In fact, waveports interfaces shared by multiple subdomains may lead to non strictly block-diagonal system matrices and hence worse performances.

In Fig. 3.15, the convergence of both dominant mode and transfinite element waveports are shown. The higher accuracy of mode continuity is paid with a worse conditioning of the global DD-SCHUR system matrix.

As we are typically interested in error controlled solvers, we proceed evaluating the error induced in the scattering parameters while varying the maximum residual

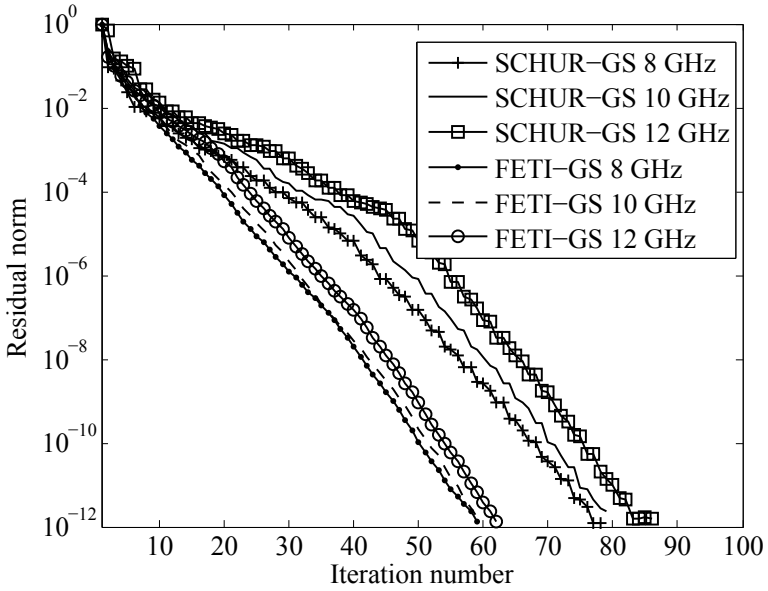

Figure 3.14: Comparison between the SCHUR and FETI Gauss-Seidel preconditioned GMRES(100) runs as the frequency of excitation varies.

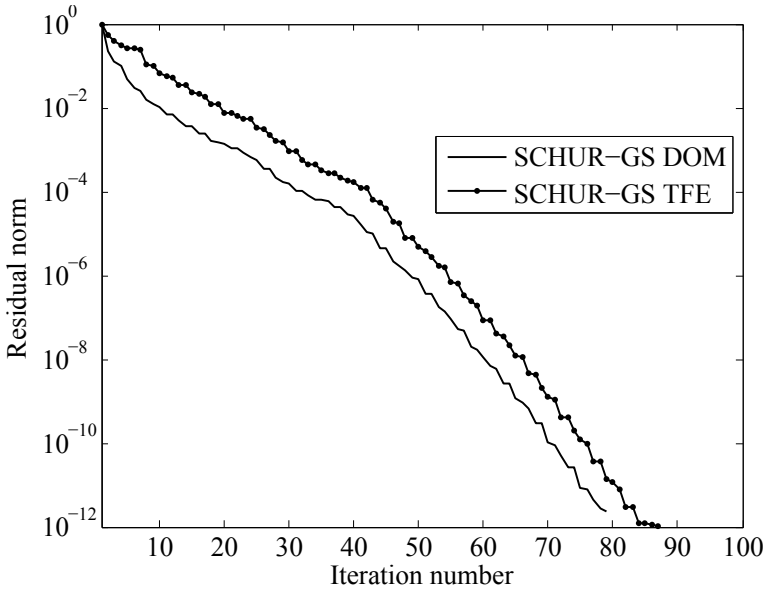

Figure 3.15: Convergence history for SCHUR-GS GMRES(100) solution at 10 GHz with either dominant mode or transfinite element method waveports boundary conditions.

error. Several runs have been performed, considering dominant mode waveports boundary conditions at 10 GHz. Table 3.3 shows that the FETI based method achieves faster a better overall accuracy than the Schur complement based. Also, while the scattering parameters error in the Schur complement based method might not be strictly lower than the prescribed residual error, in the case of the FETI they are. However, when employing the transfinite element method on the waveports, the Schur complement based method behaves differently as shown in table 3.4, assuring an error lower than the prescribed residual error.

In the case of simply partitioned electromagnetic devices, the use of SCHUR-TFE (simply SCHUR) and FETI-DOM (simply FETI) might result to be reliable in the sense of the residual error. The first usually requires more iterations than the second (hence more time), but as it results from the formulation, should provide more accurate results, especially in multi-mode analyzes in which higher-order modes are excited.

Solver	Residual error	$\lvert S_{11}\rvert$ [dB]	$\lvert S_{21}\rvert$ [dB]	$\frac{\lVert \lvert S_{ref}\rvert - \lvert S\rvert \rVert_2}{\lVert \lvert S_{ref}\rvert \rVert_2}$
Direct (reference)	-	-42.8389	-0.0024	0
DD-Schur Gauss-Seidel preconditioned	10^{-2}	-26.7529	-0.1958	$2.23\ 10^{-2}$
"	10^{-4}	-42.5118	-0.0030	$1.4234\ 10^{-4}$
"	10^{-6}	-42.8397	-0.0025	$4.0786\ 10^{-7}$
"	10^{-8}	-42.8389	-0.0024	$3.4517\ 10^{-9}$
"	10^{-10}	-42.8389	-0.0024	$8.2561\ 10^{-11}$
"	10^{-12}	-42.8389	-0.0024	$1.2571\ 10^{-13}$
DD-FETI Gauss-Seidel preconditioned	10^{-2}	-40.5331	-0.0603	$3.5\ 10^{-3}$
"	10^{-4}	-42.8404	-0.0024	$2.0280\ 10^{-6}$
"	10^{-6}	-42.8389	-0.0024	$1.1615\ 10^{-8}$
"	10^{-8}	-42.8389	-0.0024	$5.5698\ 10^{-10}$
"	10^{-10}	-42.8389	-0.0024	$1.8771\ 10^{-12}$
"	10^{-12}	-42.8389	-0.0024	$1.7357\ 10^{-14}$

Table 3.3: Scattering parameters accuracy for different prescribed residual errors (runs at 10 GHz with dominant mode on waveports).

Solver	Residual error	$\lvert S_{11}\rvert$ [dB]	$\lvert S_{21}\rvert$ [dB]	$\frac{\lVert S_{\text{ref}}-S\rVert_2}{\lVert S_{\text{ref}}\rVert_2}$
Direct (reference)	-	-42.8035	-0.0002	0
DD-Schur Gauss-Seidel preconditioned	10^{-2}	-35.1814	-0.0682	$6.4\ 10^{-3}$
"	10^{-4}	-42.7897	-0.0002	$6.8925\ 10^{-6}$
"	10^{-6}	-42.8034	-0.0002	$1.3365\ 10^{-7}$
"	10^{-8}	-42.8035	-0.0002	$3.9561\ 10^{-10}$
"	10^{-10}	-42.8035	-0.0002	$8.2355\ 10^{-12}$
"	10^{-12}	-42.8035	-0.0002	$2.0021\ 10^{-13}$

Table 3.4: Scattering parameters accuracy for different prescribed residual errors (runs at 10 GHz with transfinite elements on waveports).

3.4.4.2 Performances against subdomains number

We proceed analyzing the behavior of both SCHUR and FETI (with Gauss-Seidel preconditioners) while increasing the number of domains on the same mesh. A residual error of 10^{-4} can be retained, as it leads in both cases to a very good approximation of the solution. The whole waveguide is partitioned using Metis in 4, 8, 12 and 16 subdomains as depicted in Fig. 3.16.

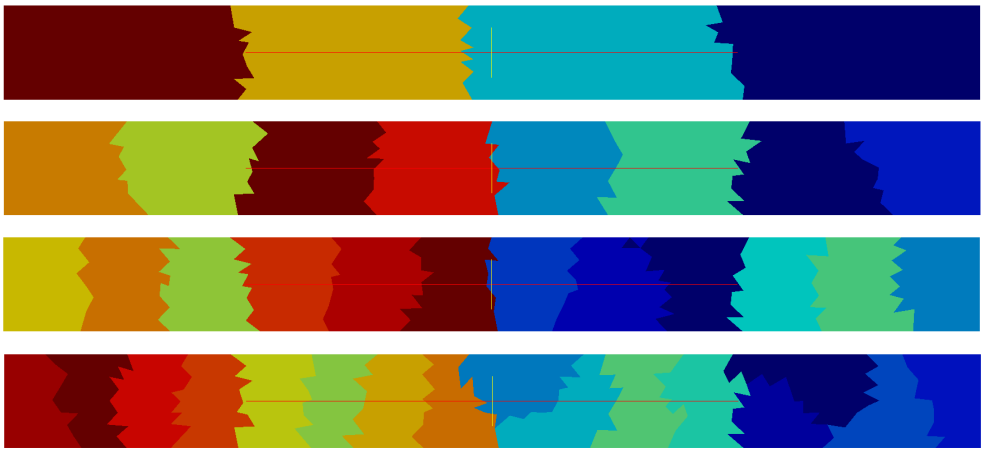

Figure 3.16: Rectangular waveguide partitionned in 4, 8, 12 and 16 subdomains with Metis.

The convergence histories for a 10 GHz excitations are shown in Fig. 3.17. In the first three analyzes, an increase of the number of subdomains resulted in a slightly larger number of iterations to achieve the residual error for both solvers. In the case of 16 domains, the convergence resulted to be much harder to achieve, especially for FETI. Furthermore, in this case, the error on the scattering parameters resulted not to be bounded by the residual error as shown in table 3.5.

Solver (Nbr of Tetrahedra)	Nbr. of Sub-domains	$\frac{\|\|\|S_{ref}\|-\|S\|\|\|_2}{\|\|S_{ref}\|\|_2}$
SCHUR (20 602)	4	$1.5926\ 10^{-6}$
"	8	$5.95814\ 10^{-6}$
"	12	$3.29779\ 10^{-5}$
"	16	$2.96923\ 10^{-4}$
FETI (20 602)	4	$2.14849\ 10^{-6}$
"	8	$5.48124\ 10^{-6}$
"	12	$1.02953\ 10^{-5}$
"	16	$5.93607\ 10^{-3}$
SCHUR (25 093)	16	$8.29628\ 10^{-6}$
FETI (25 093)	16	$1.90617\ 10^{-6}$

Table 3.5: Scattering parameters accuracy for different prescribed residual errors (runs at 10 GHz) when edge corners are avoided.

The slower convergence is mainly associated to the fact there exist some edges of the mesh shared by multiple subdomains. In fact, slightly increasing the number of tetrahedra, from 20 602 to 25 093, and partitioning the new mesh in 16 subdomains without "edge corners" (Fig. 3.18) has led to a significantly better behavior (Fig. 3.19). Furthermore, the residual error bound could be projected, as empirically found in the previous analyzes, on the scattering parameters.

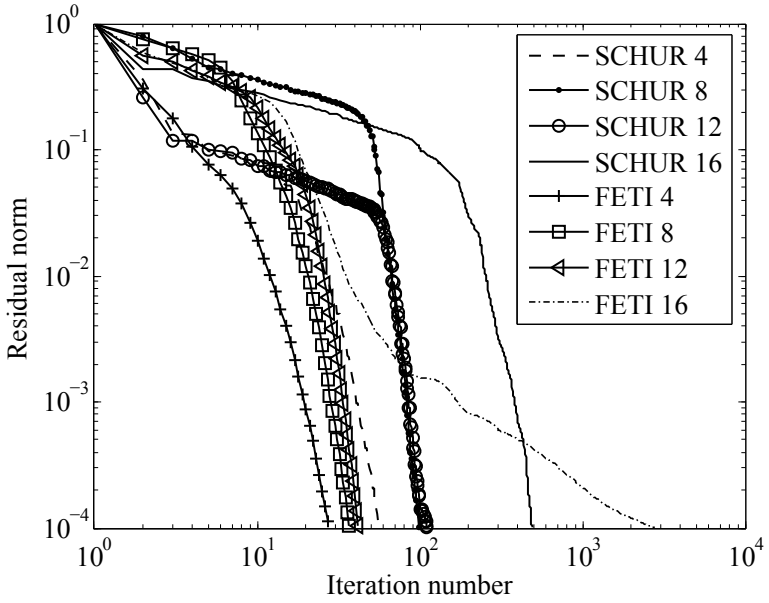

Figure 3.17: Convergence histories for SCHUR and FETI GMRES(100) solvers as the number of subdomains is increased, respectively to TFE and DOM full analyzes at 10 GHz on relative mesh.

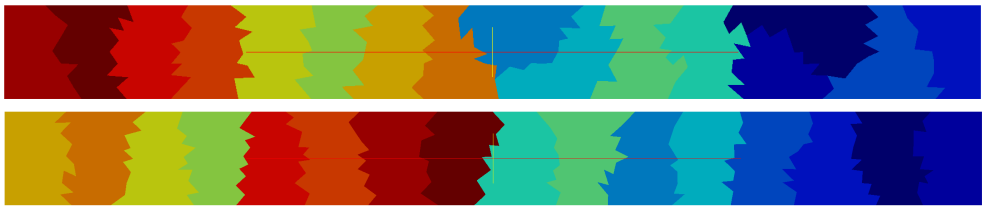

Figure 3.18: The two different meshes of the rectangular waveguide both partitioned in 16 subdomains. Top to bottom: 20 602 and 25 093 tetrahedra.

In the average, increasing the number of subdomains on a given mesh leads to slower convergence. When partitioning the mesh, edge corners must be avoided for reliable analysis, until some solution is found to remove their bad contribution.

3.4.4.3 Performances against problem size

Although the electrical size remains the same (same structure at 10 GHz), let us analyze the performances of the solvers while increasing the mesh density and hence the number of unknowns, in order to evaluate their overall complexities. The simu-

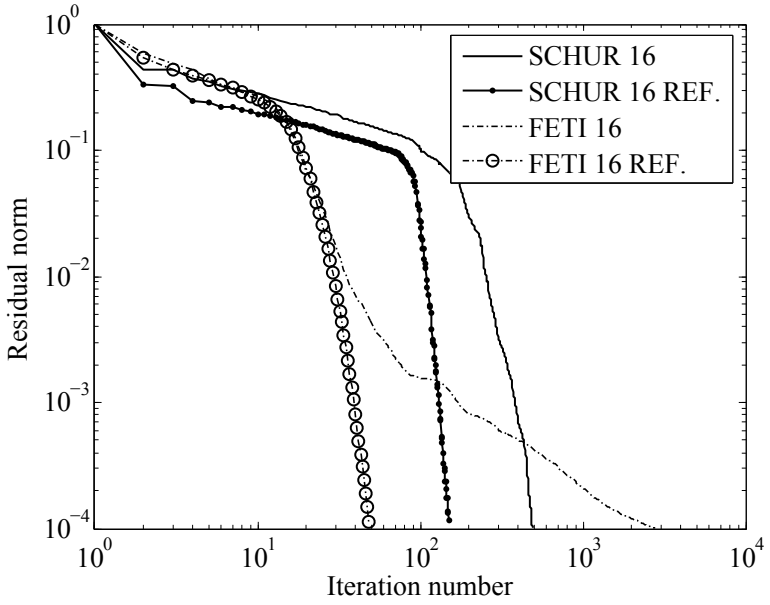

Figure 3.19: Convergence histories for SCHUR and FETI GMRES(100) solvers on initial (20 602 tetrahedra) and refined (25 093 tetrahedra) meshes partitioned in 16 subdomains.

lations are run on a workstation equipped with an Intel Xeon CPU E5-1607 3 GHz 4 cores CPU and 64 GB of physical memory. The plots for several runs on the previous WR-90 waveguide are shown in Figs. 3.20 and 3.21.

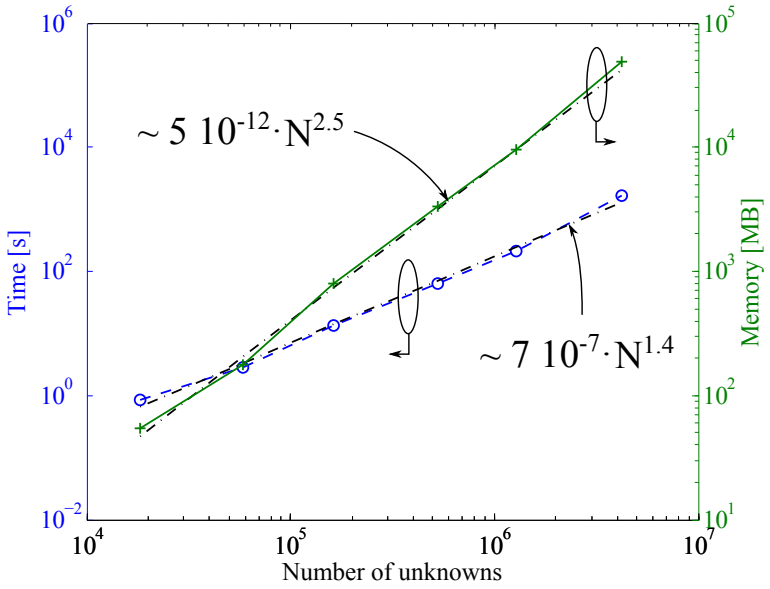

Figure 3.20: CPU time and memory consumption for different problem sizes analyzed with FES employing the double precision sparse direct solver.

The direct solver has a complexity of about $O(N^{2.5})$ in terms of memory, which agrees with what was stated in chapter 1, and the CPU times scale almost with an $O(N^{1.4})$ complexity. The GMRES(100) solver, FETI-DP preconditioned with the max-

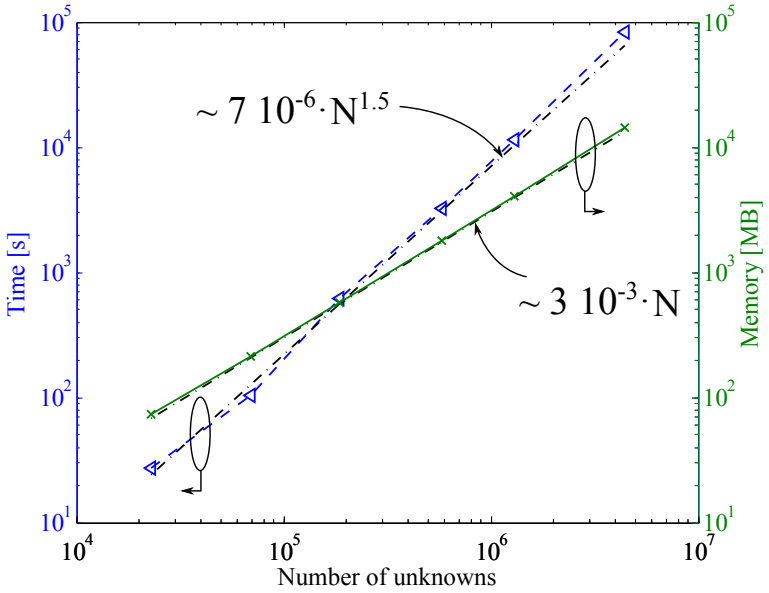

Figure 3.21: CPU time and memory consumption for different problem sizes analyzed with FES employing the GMRES(100) FETI-DP preconditioned solver.

imum number of partitions without edge corners formation and residual error of 10^{-4}, fundamentally scales linearly in terms of memory ($O(N)$) and the times behave as $O(N^{1.5})$. It is worth noticing that while the direct solver totally exploits all the 4 cores of the CPU on which the simulations are run, the GMRES does not totally and only the sequential preconditioning does on each subdomain. Also, in the last simulation of 4.3 millions of unknowns, the direct solver required 48 GB of memory while the iterative solver on 14 GB, and hence a four times larger problem (16 millions of unknowns) could be solved on the same workstation.

Chapter 4

Nonlinear Analysis of Passive Microwave Devices

It is well known that time-domain analysis of microwave devices including nonlinear materials often results to be computationally prohibitive when steady state fields are sought for [148]. A time-harmonic finite element (FE) approach at a single frequency is not sufficient to include all relevant phenomena. Higher-order harmonics are needed and may be taken into account, by using the harmonic balance finite element (HBFE) method [25–27], also known as multiharmonic finite element method [149, 150], which have demonstrated to provide a fast and accurate solution for low frequency, magneto-quasi-static problems.

In this chapter, the formulation of the HBFE is applied, for the first time, to the wave equation [151, 152]. Several test cases will be shown, demonstrating the capabilities of the method for high frequency problems. Also, as some 3D problems have been reconducted to their 2D case with some restricting assumptions. The relative formulations will be presented.

4.1 Harmonic balance finite elements for the wave equation

Given a generic multiport device (Fig. 4.1), its domain Ω, with boundary Γ, can be divided into a part Ω_1 comprising only linear media, and another part Ω_2 comprising all nonlinear media, with $\Omega = \Omega_1 \cup \Omega_2$ and $\Omega_1 \cap \Omega_2 = \emptyset$.

The permittivity, the inverse of the permeability, that is the reluctivity, and the

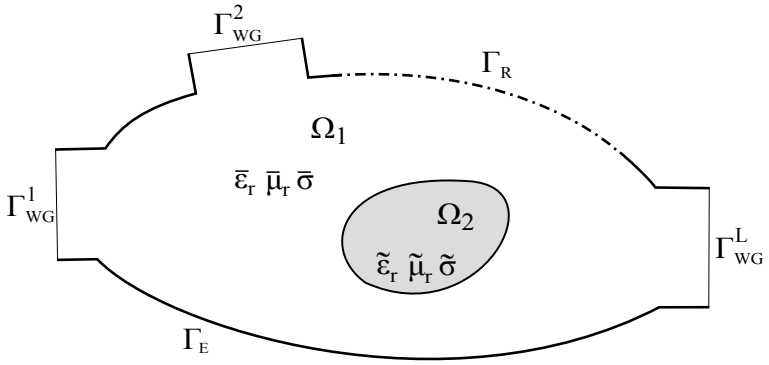

Figure 4.1: Generic multiport device where the total domain Ω is subdivided into linear subdomain Ω_1 and a nonlinear subdomain Ω_2.

conductivity in Ω can be expressed as

$$\epsilon_r(\mathbf{E}(\mathbf{r}),\mathbf{r}) = \begin{cases} \bar{\epsilon}_r(\mathbf{r}), & \mathbf{r}\in\Omega_1, \\ \tilde{\epsilon}_r(\mathbf{E}(\mathbf{r}),\mathbf{r}) = \bar{\epsilon}_r(\mathbf{r}) + \mathcal{N}_\epsilon(\mathbf{E}(\mathbf{r})), & \mathbf{r}\in\Omega_2, \end{cases} \tag{4.1.1}$$

$$\mu_r^{-1}(\mathbf{H}(\mathbf{r}),\mathbf{r}) = \nu_r(\mathbf{H}(\mathbf{r}),\mathbf{r}) = \begin{cases} \bar{\nu}_r(\mathbf{r}), & \mathbf{r}\in\Omega_1, \\ \tilde{\nu}_r(\mathbf{H}(\mathbf{r}),\mathbf{r}) = \bar{\nu}_r(\mathbf{r}) + \mathcal{N}_\nu(\mathbf{H}(\mathbf{r})), & \mathbf{r}\in\Omega_2, \end{cases} \tag{4.1.2}$$

$$\sigma(\mathbf{E}(\mathbf{r}),\mathbf{r}) = \begin{cases} \bar{\sigma}(\mathbf{r}), & \mathbf{r}\in\Omega_1, \\ \tilde{\sigma}(\mathbf{E}(\mathbf{r}),\mathbf{r}) = \bar{\sigma}(\mathbf{r}) + \mathcal{N}_\sigma(\mathbf{E}(\mathbf{r})), & \mathbf{r}\in\Omega_2, \end{cases} \tag{4.1.3}$$

where $\mathbf{E}(\mathbf{r})$ is the electric field in the generic point $\mathbf{r}$, $\mathbf{H}(\mathbf{r})$ is the magnetic field tightly bound to the electric field by (2.2.5). $\mathcal{N}_\times(\cdot)$ denotes a generic scalar operator describing the nonlinear behavior [153].

The electric field satisfies, within Ω, the wave equation (2.2.4), here reported for convenience,

$$\nabla\times\nu_r(\mathbf{H}(\mathbf{r}),\mathbf{r})\,\nabla\times\mathbf{E}(\mathbf{r}) + jk_0\zeta_0\sigma(\mathbf{E}(\mathbf{r}),\mathbf{r})\,\mathbf{E}(\mathbf{r}) - k_0^2\epsilon_r(\mathbf{E}(\mathbf{r}),\mathbf{r})\,\mathbf{E}(\mathbf{r}) = 0, \tag{4.1.4}$$

where material properties are substituted by the relations (4.1.1), (4.1.2) and (4.1.3). The boundary conditions on Γ can be any of those employed in chapter 2. For instance, in the following sections only transfinite elements will be employed on the waveports.

The Galerkin framework applied to the problem leads to (see chapter 2)

$$\int_\Omega \nabla \times \mathbf{w}_i^*(\mathbf{r}) \cdot \nu_r(\mathbf{H}(\mathbf{r}),\mathbf{r}) \nabla \times \mathbf{E}(\mathbf{r})\, d\Omega + jk_0\zeta_0 \int_\Omega \mathbf{w}_i^*(\mathbf{r}) \cdot \sigma(\mathbf{E}(\mathbf{r}),\mathbf{r})\, \mathbf{E}(\mathbf{r})\, d\Omega - k_0^2 \int_\Omega \mathbf{w}_i^*(\mathbf{r}) \cdot \epsilon_r(\mathbf{E}(\mathbf{r}),\mathbf{r})\, \mathbf{E}(\mathbf{r})\, d\Omega = \int_\Gamma \mathbf{w}_i^*(\mathbf{r}) \times \nu_r(\mathbf{H}(\mathbf{r}),\mathbf{r}) \nabla \times \mathbf{E}(\mathbf{r}) \cdot \hat{\mathbf{n}}\, d\Gamma, \quad \forall \mathbf{w}_i(\mathbf{r}) \in \mathcal{W}_E. \tag{4.1.5}$$

The multiharmonic dependence in the HBFE method is introduced by approximating the time and space dependent electric field $\boldsymbol{\mathcal{E}}(\mathbf{r},t)$ as a finite sum of harmonic components [154]

$$\hat{\boldsymbol{\mathcal{E}}}(\mathbf{r},t) = \sum_{p=1}^{P} \left(\mathbf{E}_p^{(s)}(\mathbf{r}) \sin(p\omega_0 t) + \mathbf{E}_p^{(c)}(\mathbf{r}) \cos(p\omega_0 t) \right) \tag{4.1.6}$$

where ω_0 is the fundamental angular frequency and, here and in the following, the hat over a quantity denotes its approximated value given by the truncated Fourier series. $\mathbf{E}_p^{(s)}(\mathbf{r})$ and $\mathbf{E}_p^{(c)}(\mathbf{r})$ are the spatial basis functions defined as

$$\mathbf{E}_p^{(s)}(\mathbf{r}) := \sum_{j=1}^{N} x_j^{(s)} \mathbf{w}_j(\mathbf{r}), \qquad \mathbf{w}_j(\mathbf{r}) \in \mathcal{W}_E,$$

and

$$\mathbf{E}_p^{(c)}(\mathbf{r}) := \sum_{j=1}^{N} x_j^{(c)} \mathbf{w}_j(\mathbf{r}), \qquad \mathbf{w}_j(\mathbf{r}) \in \mathcal{W}_E.$$

and they expand, as in the conventional single harmonic case the field at $p\omega_0$. Hence they must individually satisfy the wave equation with $k_0 \leftarrow pk_0$.

The material properties can also be approximated as a truncated Fourier series [149]

$$\hat{\epsilon}_r(\mathbf{E}(\mathbf{r}),\mathbf{r},t) = \epsilon_{r_0}(\mathbf{E}(\mathbf{r}),\mathbf{r}) + \sum_{g=1}^{G_\epsilon} \epsilon_{r_g}^{(s)}(\mathbf{E}(\mathbf{r}),\mathbf{r}) \sin(g\omega_0 t) + \sum_{g=1}^{G_\epsilon} \epsilon_{r_g}^{(c)}(\mathbf{E}(\mathbf{r}),\mathbf{r}) \cos(g\omega_0 t), \tag{4.1.7}$$

$$\hat{\nu}_r(\mathbf{H}(\mathbf{r}),\mathbf{r},t) = \nu_{r_0}(\mathbf{H}(\mathbf{r}),\mathbf{r}) + \sum_{g=1}^{G_\nu} \nu_{r_g}^{(s)}(\mathbf{H}(\mathbf{r}),\mathbf{r}) \sin(g\omega_0 t) + \sum_{g=1}^{G_\nu} \nu_{r_g}^{(c)}(\mathbf{H}(\mathbf{r}),\mathbf{r}) \cos(g\omega_0 t), \tag{4.1.8}$$

$$\hat{\sigma}(\mathbf{E}(\mathbf{r}),\mathbf{r},t)=\sigma_0(\mathbf{E}(\mathbf{r}),\mathbf{r})+\sum_{g=1}^{G_\sigma}\sigma_g^{(s)}(\mathbf{E}(\mathbf{r}),\mathbf{r})\sin(g\omega_0 t)+\sum_{g=1}^{G_\sigma}\sigma_g^{(c)}(\mathbf{E}(\mathbf{r}),\mathbf{r})\cos(g\omega_0 t), \quad (4.1.9)$$

where the coefficients of the expansions are given by

$$\begin{cases} \epsilon_{r_0}(\mathbf{E}(\mathbf{r}),\mathbf{r})=\dfrac{\omega_0}{2\pi}\displaystyle\int_0^{\frac{2\pi}{\omega_0}}\epsilon_r(\mathbf{E}(\mathbf{r}),\mathbf{r})\,dt, \\ \epsilon_{r_g}^{(s)}(\mathbf{E}(\mathbf{r}),\mathbf{r})=\dfrac{\omega_0}{\pi}\displaystyle\int_0^{\frac{2\pi}{\omega_0}}\epsilon_r(\mathbf{E}(\mathbf{r}),\mathbf{r})\,\sin(g\omega_0 t)\,dt, \\ \epsilon_{r_g}^{(c)}(\mathbf{E}(\mathbf{r}),\mathbf{r})=\dfrac{\omega_0}{\pi}\displaystyle\int_0^{\frac{2\pi}{\omega_0}}\epsilon_r(\mathbf{E}(\mathbf{r}),\mathbf{r})\,\cos(g\omega_0 t)\,dt, \end{cases} \quad (4.1.10)$$

$$\begin{cases} \nu_{r_0}(\mathbf{H}(\mathbf{r}),\mathbf{r})=\dfrac{\omega_0}{2\pi}\displaystyle\int_0^{\frac{2\pi}{\omega_0}}\nu_r(\mathbf{H}(\mathbf{r}),\mathbf{r})\,dt, \\ \nu_{r_g}^{(s)}(\mathbf{H}(\mathbf{r}),\mathbf{r})=\dfrac{\omega_0}{\pi}\displaystyle\int_0^{\frac{2\pi}{\omega_0}}\nu_r(\mathbf{H}(\mathbf{r}),\mathbf{r})\,\sin(g\omega_0 t)\,dt, \\ \nu_{r_g}^{(c)}(\mathbf{H}(\mathbf{r}),\mathbf{r})=\dfrac{\omega_0}{\pi}\displaystyle\int_0^{\frac{2\pi}{\omega_0}}\nu_r(\mathbf{H}(\mathbf{r}),\mathbf{r})\,\cos(g\omega_0 t)\,dt, \end{cases} \quad (4.1.11)$$

$$\begin{cases} \sigma_0(\mathbf{E}(\mathbf{r}),\mathbf{r})=\dfrac{\omega_0}{2\pi}\displaystyle\int_0^{\frac{2\pi}{\omega_0}}\sigma(\mathbf{E}(\mathbf{r}),\mathbf{r})\,dt, \\ \sigma_g^{(s)}(\mathbf{E}(\mathbf{r}),\mathbf{r})=\dfrac{\omega_0}{\pi}\displaystyle\int_0^{\frac{2\pi}{\omega_0}}\sigma(\mathbf{E}(\mathbf{r}),\mathbf{r})\,\sin(g\omega_0 t)\,dt, \\ \sigma_g^{(c)}(\mathbf{E}(\mathbf{r}),\mathbf{r})=\dfrac{\omega_0}{\pi}\displaystyle\int_0^{\frac{2\pi}{\omega_0}}\sigma(\mathbf{E}(\mathbf{r}),\mathbf{r})\,\cos(g\omega_0 t)\,dt. \end{cases} \quad (4.1.12)$$

The orders of the approximations P and $G_\times$ reflects on the accuracy of the solution and hence must be chosen upon appropriate energy criterion, for example retaining the part of the spectrum that have more than a prescribed portion of spectral power.

A conventional Galerkin approach, discretization of (4.1.5) leads to a system in the form $[A][x]=[b]$ with $[A]\in\mathbb{C}^{N\times N}$, $[x]$ and $[b]\in\mathbb{C}^N$ (chapter 2).

In an HBFE approach, the following substitutions are performed in (4.1.5)

$$\begin{aligned} \mathbf{E}(\mathbf{r}) &\longrightarrow \hat{\boldsymbol{\mathcal{E}}}(\mathbf{r},t), \\ \epsilon_r(\mathbf{E}(\mathbf{r}),\mathbf{r}) &\longrightarrow \hat{\epsilon}_r(\mathbf{E}(\mathbf{r}),\mathbf{r},t), \\ \nu_r(\mathbf{H}(\mathbf{r}),\mathbf{r}) &\longrightarrow \hat{\nu}_r(\mathbf{H}(\mathbf{r}),\mathbf{r},t), \\ \sigma(\mathbf{E}(\mathbf{r}),\mathbf{r}), &\longrightarrow \hat{\sigma}(\mathbf{E}(\mathbf{r}),\mathbf{r},t). \end{aligned}$$

Then, upon performing further testing with weights $\sin(q\omega t)$ or $\cos(q\omega t)$, $q = 1 \dots P$, and integrating over the time period of the fundamental $\left[0, \frac{2\pi}{\omega}\right)$, a large linear system is obtained which has formally the same structure as a conventional finite element system but multiple matrices $[A]$ and vectors $[x]$ and $[b]$ are assembled depending on the harmonic of testing. The final system matrix can hence be represented as

$$\begin{bmatrix} [A]^{(1s1s)} & [A]^{(1s1c)} & \dots & [A]^{(1sPc)} \\ [A]^{(1c1s)} & [A]^{(1c1c)} & \dots & [A]^{(1cPc)} \\ \vdots & \vdots & \ddots & \vdots \\ [A]^{(Pc1s)} & [A]^{(Pc1c)} & \dots & [A]^{(PcPc)} \end{bmatrix} \begin{bmatrix} [x]^{(1s)} \\ [x]^{(1c)} \\ \vdots \\ [x]^{(Pc)} \end{bmatrix} = \begin{bmatrix} [b]^{(1s)} \\ [b]^{(1c)} \\ \dots \\ [b]^{(Pc)} \end{bmatrix}. \tag{4.1.13}$$

The superscripts $(q[s|c])$ and $(p[s|c])$ indicates that the corresponding entry was computed by testing (4.1.5) with $[\sin(q\omega t)|\cos(q\omega t)]$ while the corresponding harmonic basis of (4.1.6) was $[\sin(p\omega t)|\cos(p\omega t)]$. Harmonic coupling, which clearly worsen the system matrix sparsity, only occurs within elements pertaining to nonlinear material solids, for instance, off-diagonal sub-matrices of (4.1.13) vanish within linear materials.

The nonlinearity is finally handled via a relaxed iteration. As a starting point a null electric field $[x]^0$ is assumed, computing the pertinent system matrix $\left[A_{([x]^0)}\right]$ and known term $\left[b_{([x]^0)}\right]$ and solving the system $\left[A_{([x]^0)}\right][x]^1 = \left[b_{([x]^0)}\right]$. The newly computed field $[x]^1$ can now be used to update system matrix and known term and perform the following relaxed iteration:

$$\left[A_{(\gamma[x]^{i-1}+(1-\gamma)[x]^{i-2})}\right][x]^i = \left[b_{(\gamma[x]^{i-1}+(1-\gamma)[x]^{i-2})}\right], \tag{4.1.14}$$

with $i \geq 2$ and $\gamma \in (0, 1]$. $\gamma = 1$ gives the standard Picard iteration [153], while low γ values damps the oscillations which may arise with highly nonlinear materials or high intensity impressed fields at the cost of a slower convergence [155]. The process is repeated until the relative error between the updated solution and the previous one, in the sense of the Euclidean norm, is less than a prescribed value τ, that is

$$\frac{\| [x]^i - [x]^{i-1} \|_2}{\| [x]^i \|_2} < \tau.$$

4.2 Harmonic testing generalities

The multi-harmonic testing can straightforwardly exploit the orthogonality between sine and cosine function defined as

$$\begin{aligned} \frac{\omega_0}{\pi} \int_0^{\frac{2\pi}{\omega_0}} \cos(m\omega_0 t)\, \cos(n\omega_0 t)\, dt &= \delta_{mn}, \\ \frac{\omega_0}{\pi} \int_0^{\frac{2\pi}{\omega_0}} \sin(m\omega_0 t)\, \sin(n\omega_0 t)\, dt &= \delta_{mn}, \\ \frac{\omega_0}{\pi} \int_0^{\frac{2\pi}{\omega_0}} \sin(m\omega_0 t)\, \cos(n\omega_0 t)\, dt &= 0, \end{aligned}$$

and for the constant terms in materials characteristics we have

$$\begin{aligned}\frac{\omega_0}{2\pi}\int_0^{\frac{2\pi}{\omega_0}} \cos(n\omega_0 t)\,dt &= 1,\\ \frac{\omega_0}{2\pi}\int_0^{\frac{2\pi}{\omega_0}} \sin(n\omega_0 t)\,dt &= 1,\end{aligned}$$

where $m \neq 0$, $n \neq 0$ and δ_{mn} is the Kronecker delta. Once the material properties expansion coefficients are computed, it might seem that the testing of (4.1.5) on the time period involves more than two trigonometric functions. It is possible to compute such testing integrals simply upon exploiting the following relations between the products of trigonometric functions

$$\cos(m\omega t)\cos(n\omega t) = \frac{1}{2}\cos((m-n)\omega t) + \frac{1}{2}\cos((m+n)\omega t), \tag{4.2.1}$$

$$\sin(m\omega t)\sin(n\omega t) = \frac{1}{2}\cos((m-n)\omega t) - \frac{1}{2}\cos((m+n)\omega t), \tag{4.2.2}$$

$$\sin(m\omega t)\cos(n\omega t) = \frac{1}{2}\sin((m-n)\omega t) + \frac{1}{2}\sin((m+n)\omega t), \tag{4.2.3}$$

hence splitting them into integrals that involve only two trigonometric functions.

All the testings on material properties can be either precomputed analytically, up to some prescribed orders, or numerically by the use of the fast fourier transform (FFT) [156]. The FFT is an efficient algorithm that implements the discrete Fourier transform, defined as

$$X_q = \sum_{k=0}^{N-1} x_k \mathrm{e}^{-j\frac{2\pi}{N}kq}, \qquad q = 0, 1, \ldots, N-1. \tag{4.2.4}$$

When x_k is a sequence of N samples of $\hat{\epsilon}_r(\mathbf{E}(\mathbf{r}), \mathbf{r}, t)$, $\hat{\nu}_r(\mathbf{H}(\mathbf{r}), \mathbf{r}, t)$ or $\hat{\sigma}(\mathbf{E}(\mathbf{r}), \mathbf{r}, t)$ within the period $[0, \frac{2\pi}{\omega_0})$, then X_q correspond to the expansion coefficients at the given normalized frequencies $q = \frac{g\omega_0}{\omega_0}$. Of course, one must use Euler formulas

$$\cos(nt) = \frac{\mathrm{e}^{jnt} + \mathrm{e}^{-jnt}}{2}, \tag{4.2.5}$$

$$\sin(nt) = \frac{\mathrm{e}^{jnt} - \mathrm{e}^{-jnt}}{2j}, \tag{4.2.6}$$

$$\mathrm{e}^{jnt} = \cos(nt) + j\sin(nt), \tag{4.2.7}$$

before and after the FFT and changing the phase where necessary to recover the proper values.

As will be shown in the intermodulation products example, p, q and g do not necessarily need to be integers. In fact, when considering multiple signals feeding a nonlinear device, these generate higher-order harmonics at multiples of the sum or difference between the impinging signals frequencies. Hence, for the necessary computational accuracy, the largest sampling period has to be considered in an FFT testing algorithm, and this is given by the largest common divisor between all the impinging signals.

4.3 Transverse magnetic field formulation

Let us assume the electric field $\mathbf{E}$ to be only $\hat{\mathbf{z}}$-directed such that $\mathbf{E} = E_z\hat{\mathbf{z}}$. Both fields and material properties are assumed not to vary along the $\hat{\mathbf{z}}$ direction and hence $E_z = E_z(x,y)$ and the magnetic field will have only transverse components, that is $H_x(x,y)$ and $H_y(x,y)$. Then the wave equation

$$\nabla \times \overline{\overline{\nu}}_r \ \nabla \times \mathbf{E} + jk_0\zeta_0\overline{\overline{\sigma}}\ \mathbf{E} - k_0^2\overline{\overline{\epsilon}}_r\ \mathbf{E} = 0,$$

becomes

$$\nabla \cdot \overline{\overline{\nu}}_r\ \nabla E_z - jk_0\zeta_0\overline{\overline{\sigma}}\ E_z + k_0^2\overline{\overline{\epsilon}}_r\ E_z = 0. \tag{4.3.1}$$

In fact, we have

$$\nabla \times \overline{\overline{\nu}}_r \nabla \times E_z\hat{\mathbf{z}} = \nabla \times (-\hat{\mathbf{z}} \times \overline{\overline{\nu}}_r \nabla E_z),$$

and by the use of the relation [157] $\nabla \times (\hat{\mathbf{z}} \times \mathbf{v}) = \hat{\mathbf{z}}\nabla \cdot \mathbf{v} - \frac{\partial \mathbf{v}}{\partial z}$ and remembering that $E_z(x,y)$ is independent on the z variable, we have

$$\nabla \times (-\hat{\mathbf{z}} \times \overline{\overline{\nu}}_r \nabla E_z) = -\hat{\mathbf{z}}\nabla \cdot \overline{\overline{\nu}}_r \nabla E_z - \underbrace{\frac{\partial \overline{\overline{\nu}}_r \nabla E_z}{\partial z}}_{=0}.$$

Finally we achieve

$$-\hat{\mathbf{z}}\nabla \cdot \overline{\overline{\nu}}_r\ \nabla E_z + jk_0\zeta_0\overline{\overline{\sigma}}\ E_z\hat{\mathbf{z}} - k_0^2\overline{\overline{\epsilon}}_r\ E_z\hat{\mathbf{z}} = 0.$$

which can be written as (4.3.1) upon removing the $\hat{\mathbf{z}}$ and multiplying by -1 all the terms of the equation. The field E_z can be expanded with scalar basis functions $\phi \in \mathcal{V}(\Omega_h) := \{\phi \in\} \subset \mathcal{H}^1(\Omega, \Gamma_E)$ such that

$$E_z = \sum_{j=1}^{N_z} x_{z,j}\phi_j.$$

Galerkin projection leads to the following weak form

$$\int_\Omega \nabla\phi_i^* \cdot \overline{\overline{\nu}}_r\ \nabla E_z\ d\Omega + jk_0\zeta_0 \int_\Omega \phi_i^* \overline{\overline{\sigma}}\ E_z\ d\Omega - k_0^2 \int_\Omega \phi_i^* \overline{\overline{\epsilon}}_r\ E_z d\Omega = \int_\Gamma \phi_i^* \overline{\overline{\nu}}_r\ \nabla E_z \cdot \hat{\mathbf{n}}\ d\Gamma. \tag{4.3.2}$$

where the vector identity $A\nabla \cdot \mathbf{B} = \nabla \cdot (A\mathbf{B}) - \nabla A \cdot \mathbf{B}$ and Gauss' theorem have been exploited [157]. $\hat{\mathbf{n}}$ is the outwardly directed normal unit vector.

Due to the field homogeneity along the $\hat{\mathbf{z}}$ direction, only a few components of materials tensors will contribute to the equation, for instance

$$\overline{\overline{\nu}}_r = \begin{bmatrix} \nu_{r,\mathbf{xx}} & \nu_{r,\mathbf{xy}} \\ \nu_{r,\mathbf{yx}} & \nu_{r,\mathbf{yy}} \end{bmatrix} = \begin{bmatrix} \mu_{r,\mathbf{xx}} & \mu_{r,\mathbf{xy}} \\ \mu_{r,\mathbf{yx}} & \mu_{r,\mathbf{yy}} \end{bmatrix}^{-1}, \tag{4.3.3}$$

$$\overline{\overline{\sigma}} = \sigma_{\mathbf{zz}}, \tag{4.3.4}$$

$$\overline{\overline{\epsilon}}_r = \epsilon_{r,\mathbf{zz}}. \tag{4.3.5}$$

All the considerations made in chapter 2 can be applied on Γ integrals upon imposing the previous condition on the electric field. In particular, we will consider the waveports segments of figure 4.1 (as in 2D problem) with impinging TE_{m0} modes with $m \in \mathbb{N}^+$, hence respecting the $\mathbf{E} = E_z\hat{\mathbf{z}}$ condition. Also here, the modal distributions can be computed either analytically [101] or numerically by solving the transverse-longitudinal eigenvalue one-dimensional problem analogously to what is done in chapter 2 for a two-dimensional problem.

4.4 Numerical tests

Here follows three tests performed to illustrate the performances of the HBFE method for the wave equation.

4.4.1 Millimeter-wave bandpass filter with nonlinear dielectrics

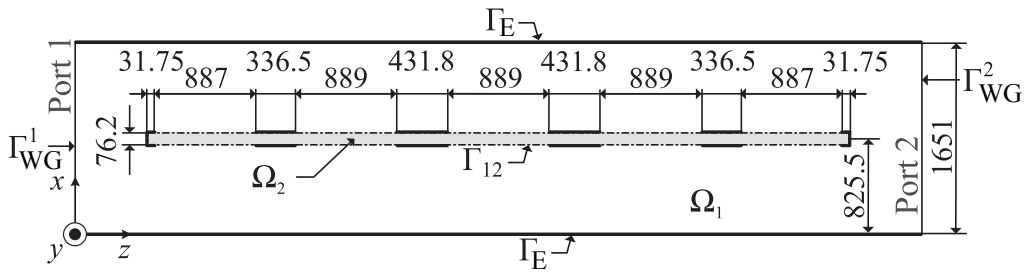

Figure 4.2: Cross section (H-plane) of a passband filter realized by placing on the E-plane a dielectric slab partially metalized on both sides (slab is shown in light grey; metal strips - uniform along y are shown as thick black lines) in a WR6 rectangular waveguide. Measures are given in μm.

The millimeter-wave passband filter in WR6 (1651x825.5 μm) rectangular waveguide, initially presented in chapter 2 with a full-wave formulation is here analyzed with a transverse magnetic 2D formulation [135]. The filter, uniform along y axis, is realized by placing on the E-plane a dielectric slab partially metalized on both sides as shown by the H-plane cross section of Fig. 4.2. All conductors are considered perfect. $\mu_r = 1$ and $\sigma = 0$ everywhere in Ω. The dielectric, enclosed in Ω_2, presents a Kerr-type nonlinearity of such that [153]

$$\tilde{\epsilon}_r(\mathbf{E}(\mathbf{r}), \mathbf{r}) = \bar{\epsilon}_r(\mathbf{r}) + \alpha_2 \, |\mathbf{E}(\mathbf{r})|^2, \qquad \mathbf{r} \in \Omega_2 \tag{4.4.1}$$

where $\bar{\epsilon}_r(\mathbf{r}) = 2.1$ and $\alpha_2 = 1.625\ 10^{-10}\ \frac{\mathrm{m}^2}{\mathrm{kV}^2}$.

The Kerr-like behavior of the permittivity induces the generation of odd order harmonics, thus even ones can been neglected. For the relaxed iteration stop criterion, $\tau = 10^{-6}$ has been chosen. The continuity of the field at the ports is imposed through a modal expansion exploiting only TE_{m0} modes, $m = 2n+1$, $n = 1, \ldots, 4$, even m modes being absent for the E-plane symmetry of the filter. The excitation is a TE_{10}

mode at fundamental frequency impinging at Port 1 with maximum field amplitude E_i. The waveguide discontinuity represented by the filter transfers power to higher order modes, which may result to be guided at higher harmonic frequencies. Furthermore, as a sinusoidal excitation is chosen, only $\sin(p\omega t)$ related coefficients are retained. Due to H-plane uniformity, the problem can be treated as two-dimensional [101]. First order nodal elements are used and the discretization leads to 2473 degrees of freedom, 80 of which belong to the nonlinear subdomain Ω_2, 314 to the boundaries and 2079 to the linear subdomain Ω_1. Such a fine discretization is necessary to obtain a good approximation of the field up to the 5^{th} harmonic.

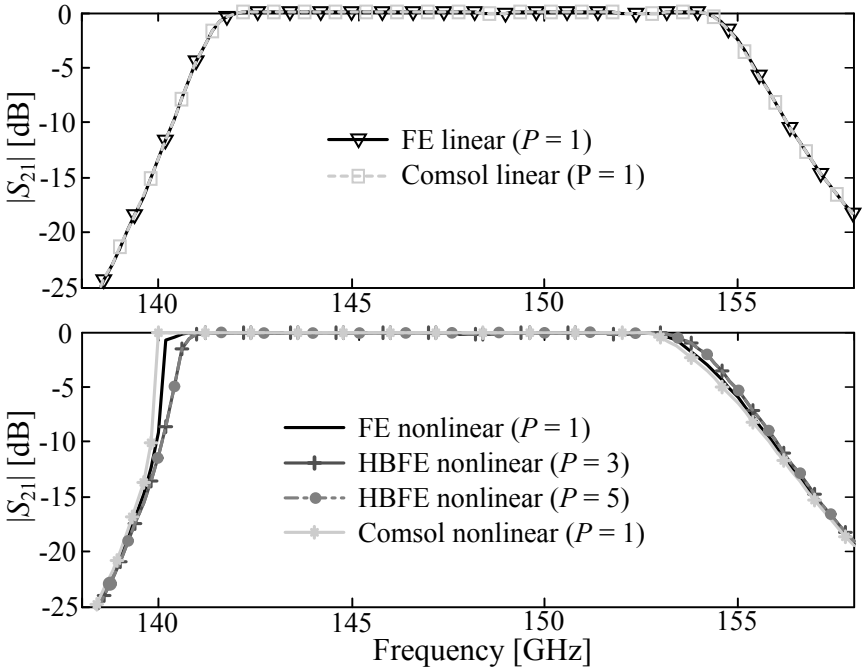

Figure 4.3: TE_{10} spectral response for linear (top) and nonlinear (bottom) permittivity with $E_i = 10\ \frac{\text{kV}}{\text{m}}$. The results are compared with Comsol RF module linear and nonlinear solutions.

As a first analysis, the effect of the total number of harmonics P retained on the filter's spectral response is investigated (Fig. 4.3). For an incident field amplitude $E_i = 10\ \frac{\text{kV}}{\text{m}}$, the Picard iteration proved to converge. Equal mesh and parameters have been used to conduct a 2D finite element (single harmonic) analysis with Comsol RF Module [6]. Being the nonlinear loop tackled differently (Comsol uses Newton algorithm), perfect matching in the spectral response is not obtained as for the linear permittivity case ($\alpha_2 = 0$). It is evident from Fig. 4.3 that including the 3^{rd} harmonic is crucial for proper evaluation of the device bandwidth.

The electric field distribution at 146 GHz, 438 GHz and 730 GHz are shown in Fig. 4.4. As higher-order harmonics are generated by the fundamental field flowing through nonlinear parts of the device, the related fields will be, also for passivity concerns, of various orders of magnitude lower.

To gain better insight, simulations have been repeated with $E_i = 5\ \frac{\text{kV}}{\text{m}}$ and $E_i =$

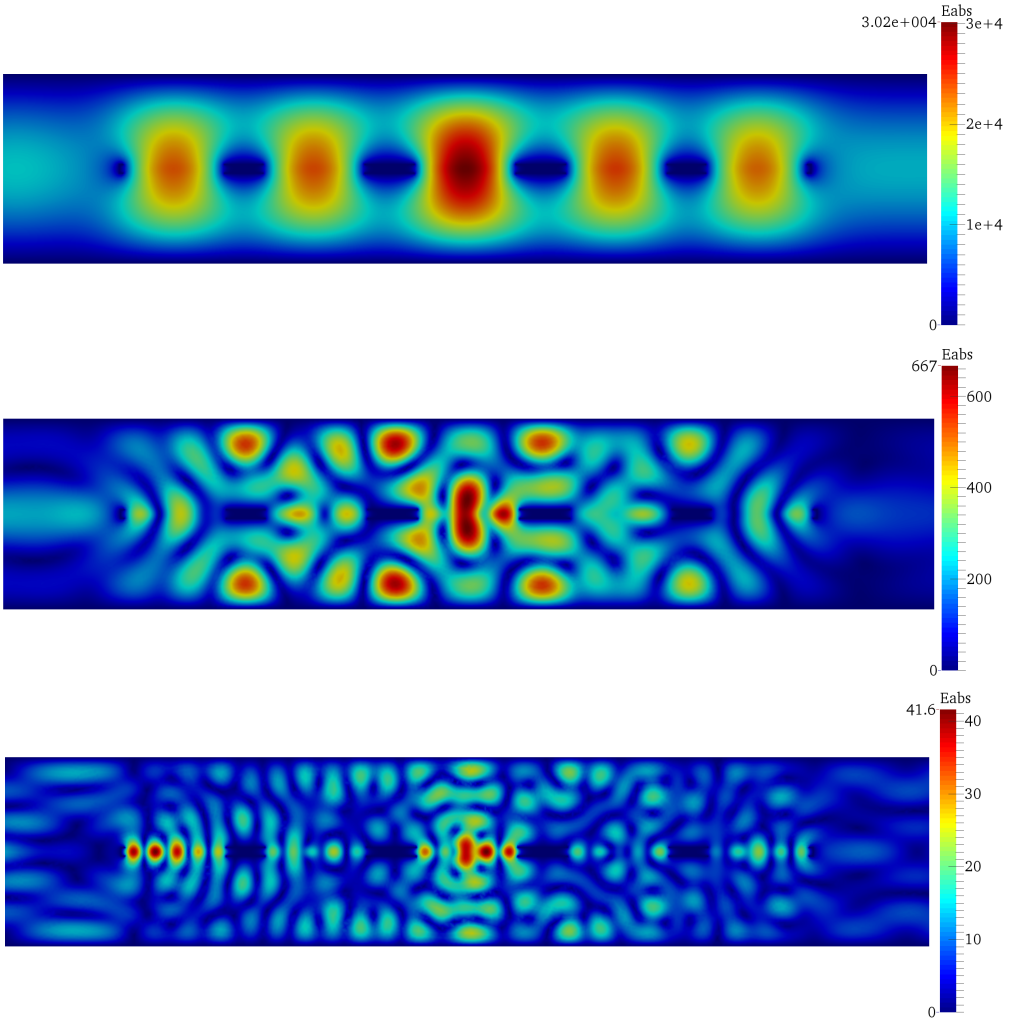

Figure 4.4: $|E_y|$ distribution within the filter at fundamental ($f_0 = 146$ GHz), 3rd and 5th order harmonics ($E_i = 10$ $\frac{kV}{m}$).

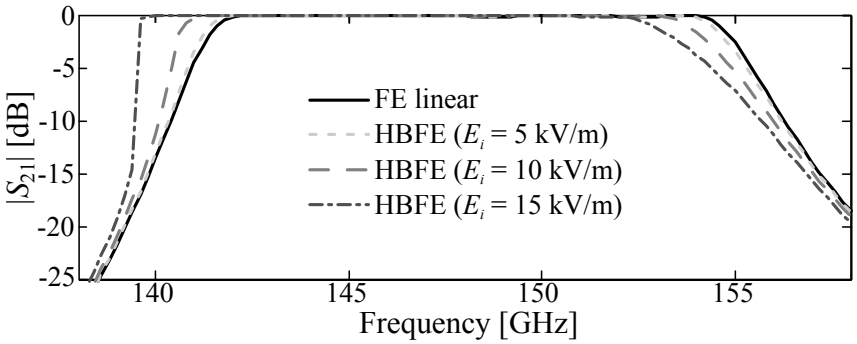

Figure 4.5: $|S_{21}|$ of the nonlinear filter for several values of E_i compared to the linear case. Field is approximated up to the 5th harmonic.

15 $\frac{kV}{m}$, for $P = 5$. The results compared to those of a linear device are shown in Fig. 4.5. There is an evident shift of the band towards lower frequencies as higher power densities are involved, which agrees to [158]. Furthermore the $E_i = 15$ $\frac{kV}{m}$

did not converge with Picard iteration and required a relaxed $\gamma = 0.1$ iteration.

Analysis of the spectral response convergence is performed computing the relative error, in Euclidean norm sense, all over the device bandwidth while increasing the order of HBFE system such that

$$\text{error}(P = p) = \frac{\| |S_{21}|^p - |S_{21}|^{p-2} \|_2}{\| |S_{21}|^{p-2} \|_2} \tag{4.4.2}$$

with $p = 2n + 1$, $n = 1, \ldots, 5$. Results (Fig. 4.6) show faster convergence for low intensity impinging fields.

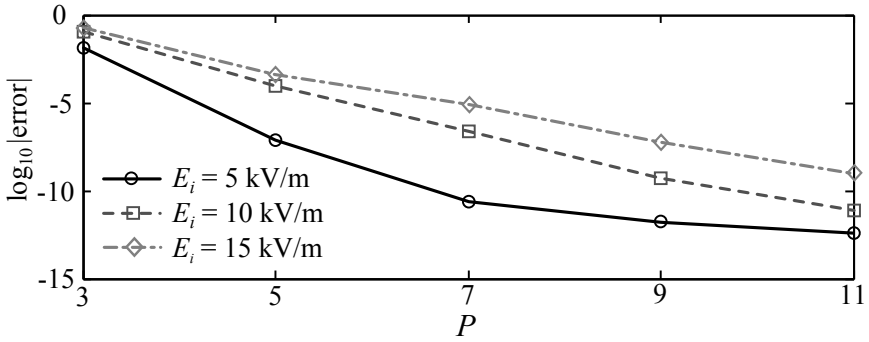

Figure 4.6: Relative error of the spectrum at fundamental frequency for various E_i values.

To enhance the computational efficiency, a Schur complement based domain decomposition approach is here proposed [153, 159]. The multiharmonic unknowns vector $[x]$ defined by the HBFE method over Ω can be split into two vectors $[x_1]$ and $[x_2]$ containing the unknowns belonging to interior points in Ω_1 and Ω_2, respectively. Unknowns belonging to the boundaries $\Gamma \cup \Gamma_{12}$ are placed in a third vector $[x_\Gamma]$. The HBFE system can then be recast in :

$$\begin{bmatrix} [A_{11}] & 0 & [A_{1\Gamma_1}] \\ 0 & [A_{22}]^{i-1} & [A_{2\Gamma_2}]^{i-1} \\ [A_{\Gamma_1 1}] & [A_{\Gamma_2 2}]^{i-1} & [A_{\Gamma\Gamma}]^{i-1} \end{bmatrix} \begin{bmatrix} [x_1]^i \\ [x_2]^i \\ [x_\Gamma]^i \end{bmatrix} = \begin{bmatrix} [b_1] \\ [b_2]^{i-1} \\ [b_\Gamma]^{i-1} \end{bmatrix} \tag{4.4.3}$$

where $[A_{11}]$ contains the HBFE coefficients of the linear system related to the unknowns $[x_1]$, with null harmonic coupling coefficients, while $[A_{22}]$ contains coefficients for the nonlinear subdomain Ω_2. $[A_{\Gamma_\times \times}]$ and $[A_{\times \Gamma_\times}]$ represent couplings between interior unknowns and boundary unknowns collected in $[x_\Gamma]$. By using the Schur complement concept, the boundary unknowns $[x_\Gamma]^i$ of (4.4.3), and hence the generalized scattering matrix of the device, can be retrieved [153, 159]. Hence, in order to solve the HBDDFE system, every single submatrix is assembled at first sight, then, within the iteration loop, only the submatrices related to Ω_2 and Γ_{12} are to be updated. The efficiency of this DD technique relies on the fragmentation of the matrices and the subsequent computation of partial solutions. When the number of coefficients related to the nonlinear media is small, noticeable improvements can be achieved.

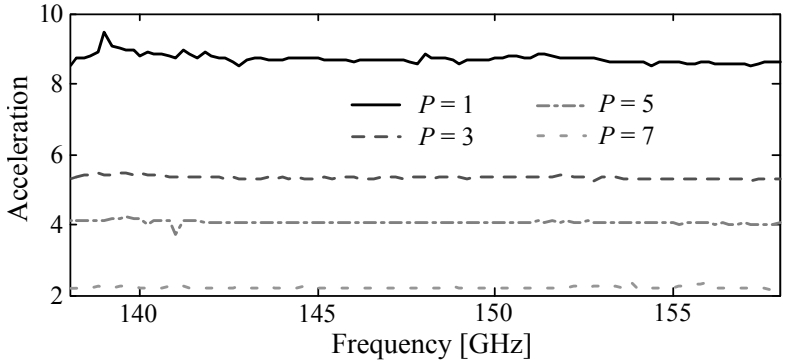

Figure 4.7: Acceleration spectrum obtained for an HBFE system of several harmonic orders. The computations are made for $E_i = 15\ \frac{\text{kV}}{\text{m}}$ ($\gamma = 0.1$).

The efficiency of the DD technique can be assessed by its acceleration,

$$\text{Acceleration} = \frac{\text{HBFE time}}{\text{HBDDFE time}},$$

that is the ratio between time for a full domain computation - inclusive of nonlinear iterations - and the corresponding DD computation (assembly and solve) [153]. Fig. 4.7 presents the acceleration for each frequency point, and for different values of P at $E_i = 10\ \frac{\text{kV}}{\text{m}}$.

In general, higher order HBDDFE systems have lower acceleration, since the matrices dimensions related to nonlinear media increase. With a $P = 3$ system, the acceleration varies in the range [2.51, 9.15], averaging to 4.18, and leading to an HBDDFE solution in 24% of the time required by a full domain HBFE solution.

4.4.2 Microwave circulator intermodulation products

The test case of a H-plane circulator in rectangular waveguide constituted by a Y-junction with a magnetized ferrite post is presented [160]. The circulator comprises three WR90 (cross-section dimensions a=22.86 mm and b=10.16 mm) waveguide sections of length l=33.4 mm joined forming a 120° angle one with each other in a Y shape and a magnetized ferrite post of height b, hence spanning the whole device height. The post is an equilateral triangular prism of base side d=7.80 mm, placed at the center of the junction as sketched in Fig. 4.8 and it is magnetized along $\hat{\mathbf{z}}$.

While the most of the device, Ω_1, is in air ($\bar{\epsilon}_r = \bar{\mu}_r = 1$), the post, Ω_2, is made of a nonlinear magnetized ferrite. In [160] and in many other papers, the ferrite is considered linear and characterized by:

$$\overline{\overline{\mu}}_r = \begin{bmatrix} \mu_r & j\kappa_r \\ -j\kappa_r & \mu_r \end{bmatrix}, \tag{4.4.4}$$

$$\overline{\overline{\epsilon}}_r = \epsilon_r, \tag{4.4.5}$$

with, as in the standard linear approach in which only the static (DC) external im-

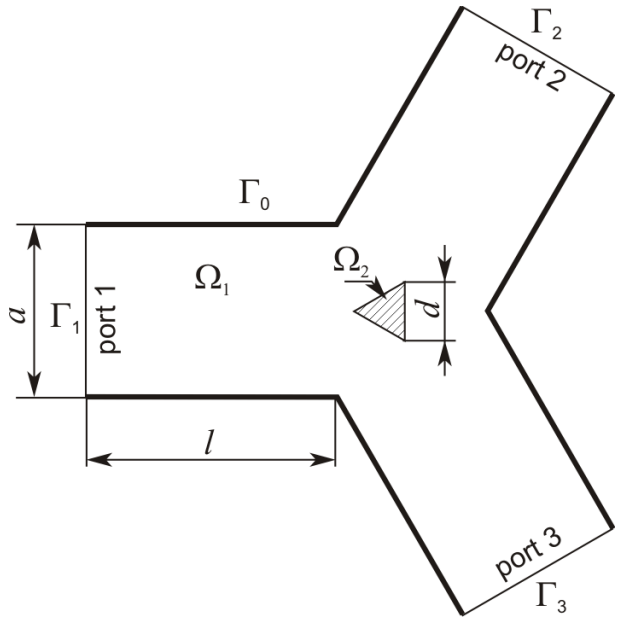

Figure 4.8: Geometry layout of the ferrite circulator. The two domains Ω_1 and Ω_2, respectively corresponding to linear and nonlinear domains, are shown.

pressed magnetic field is considered and the harmonic (AC) signal neglected:

$$\mu_r = 1 + \frac{(\omega_0 + j\omega\alpha)\omega_m}{(\omega_0 + j\omega\alpha)^2 - \omega^2}, \quad \kappa_r = \frac{\omega\omega_m}{(\omega_0 + j\omega\alpha)^2 - \omega^2}, \tag{4.4.6}$$

being $\omega_0 = \gamma H_i$, $\omega_m = \gamma M_s$, $\alpha = \gamma\frac{\Delta H}{2\omega}$; and being H_i the external DC magnetic impressed field, uniform along the out of plane direction, M_s the saturation magnetization, ΔH the resonance linewidth and γ the gyromagnetic ratio. In the following the values considered will be: $\gamma = 1.76\ 10^7\ \frac{\mathrm{C}}{\mathrm{kg}}$, $H_i = 200$ G, $M_s = 1317$ Oe, $\Delta H = 135$ Oe $\cdot$ s and $\epsilon_r = 11.7$ as reported in [160].

Relation (4.4.4) still holds for non-linear ferrites if the AC magnetic field is not neglected with respect to the external DC magnetic field. In this case $\mathbf{H} = H_i\hat{\mathbf{z}} + \mathbf{H}_{\mathrm{AC}}$ and $\mathbf{M} = M_s\hat{\mathbf{z}} + \mathbf{M}_{\mathrm{AC}}$, upon derivation from the macroscopic equation of motion for large signals and assumption of the $\hat{\mathbf{z}}$-directed components of the AC field to be neglectable, (4.4.6) are replaced by:

$$\mu_r = 1 + \frac{(\omega_0 + j\omega\alpha)\omega_m}{(\omega_0 + j\omega\alpha)^2 + (\gamma H_x)^2 + (\gamma H_y)^2 - \omega^2}, \tag{4.4.7}$$

$$\kappa_r = \frac{\omega\omega_m}{(\omega_0 + j\omega\alpha)^2 + (\gamma H_x)^2 + (\gamma H_y)^2 - \omega^2}, \tag{4.4.8}$$

being H_x and H_y the two components, on the H-plane, of the AC magnetic field.

The analysis is first conducted assuming small signals impinging on Port 1 (Γ_1), hence with linear permeability tensor. The resulting spectral response is given in Fig. 4.9, and it matches the one reported by [160]. Figure 4.10 reports the corresponding fieldmap for a 9 GHz signal.

To assess the nonlinearity of the modeled device, the circulator is analyzed assuming a strong interfering signal impinging on the isolated port (Γ_3) at $f_i = 10$ GHz,

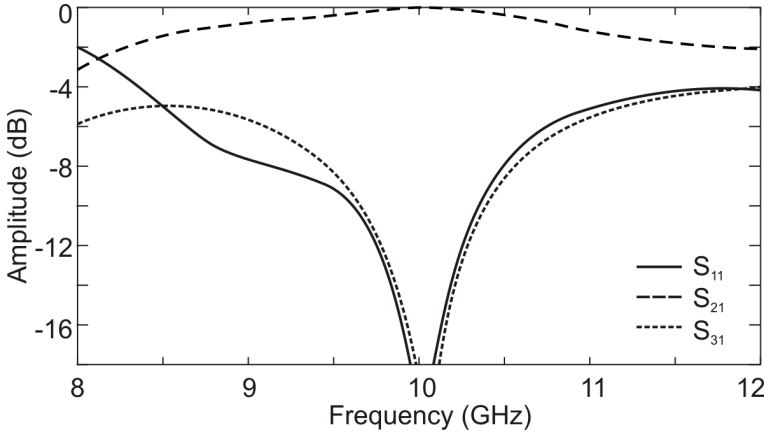

Figure 4.9: Circulator's small signal frequency response.

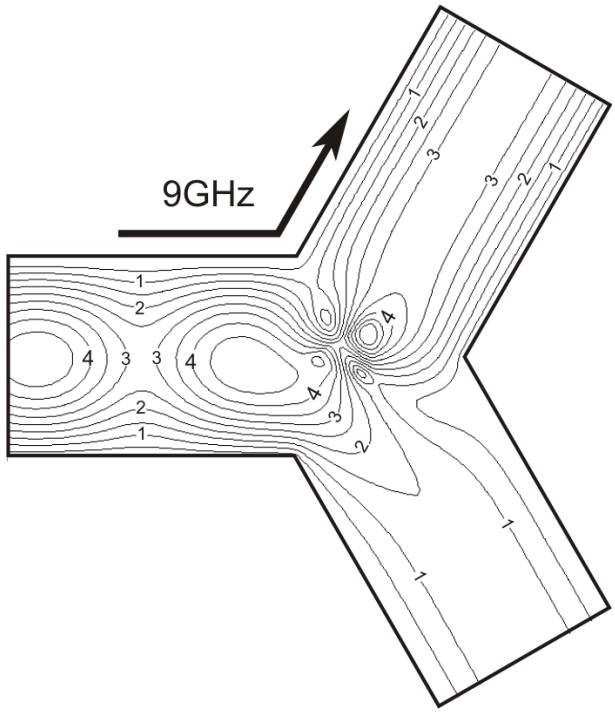

Figure 4.10: Electric field $\left(\frac{\text{kV}}{\text{m}}\right)$ distribution at 9 GHz for 1 W impinging on Γ_1.

10 dB higher than the signal at Port 1, being the signal frequency $f_s \in [8, 12]$ GHz, engendering undesired intermodulation products (IMPs) at the coupled port (Γ_2). The convergence of the harmonic orders (P) is analyzed upon increasing the order progressively and monitoring the power kept by in-band IMPs signals ($2f_i - f_s$ and $2f_s - f_i$). The order of G is chosen such that $G\omega_g = \max(\omega_{\{p\}})$, $\omega_g = \gcd(\omega_i, \omega_s)$. For this test, the signal power impinging at $f_s = 9$ GHz has been assumed of 150 W, and the interferer one of 1.5 kW at $f_i = 10$ GHz. An iteration loop stop criterion $\tau = 10^{-9}$ has been assumed. Results are shown in table 4.1, while Fig. 4.11 reports the fieldmaps at the signal and interferent frequencies, as well as the in-band interferent.

	Harmonic order considered (cumulative from left to right)			
Harmonic order	Only $2f_1 - f_2, 2f_2 - f_1$	$2f_1 + f_2, 2f_2 + f_1,$ $3f_1, 3f_2$ (all 3$^{\text{rd}}$ order)	$f_1 + f_2, \lvert f_1 - f_2 \rvert,$ $2f_1, 2f_2$ (all 2$^{\text{nd}}$ order)	$3f_1 - 2f_2, 3f_2 - 2f_1,$ $3f_1 + 2f_2, 3f_2 + 2f_1$
Power at $2f_1 - f_2$ [W]	$4.6019\ 10^{-3}$	$4.2246\ 10^{-3}$	$4.2246\ 10^{-3}$	$4.2186\ 10^{-3}$
Power at $2f_2 - f_1$ [W]	$2.0990\ 10^{-1}$	$2.1951\ 10^{-1}$	$2.1951\ 10^{-1}$	$2.1991\ 10^{-1}$

Table 4.1: Harmonic power at third order intermodulation products as P is increased.

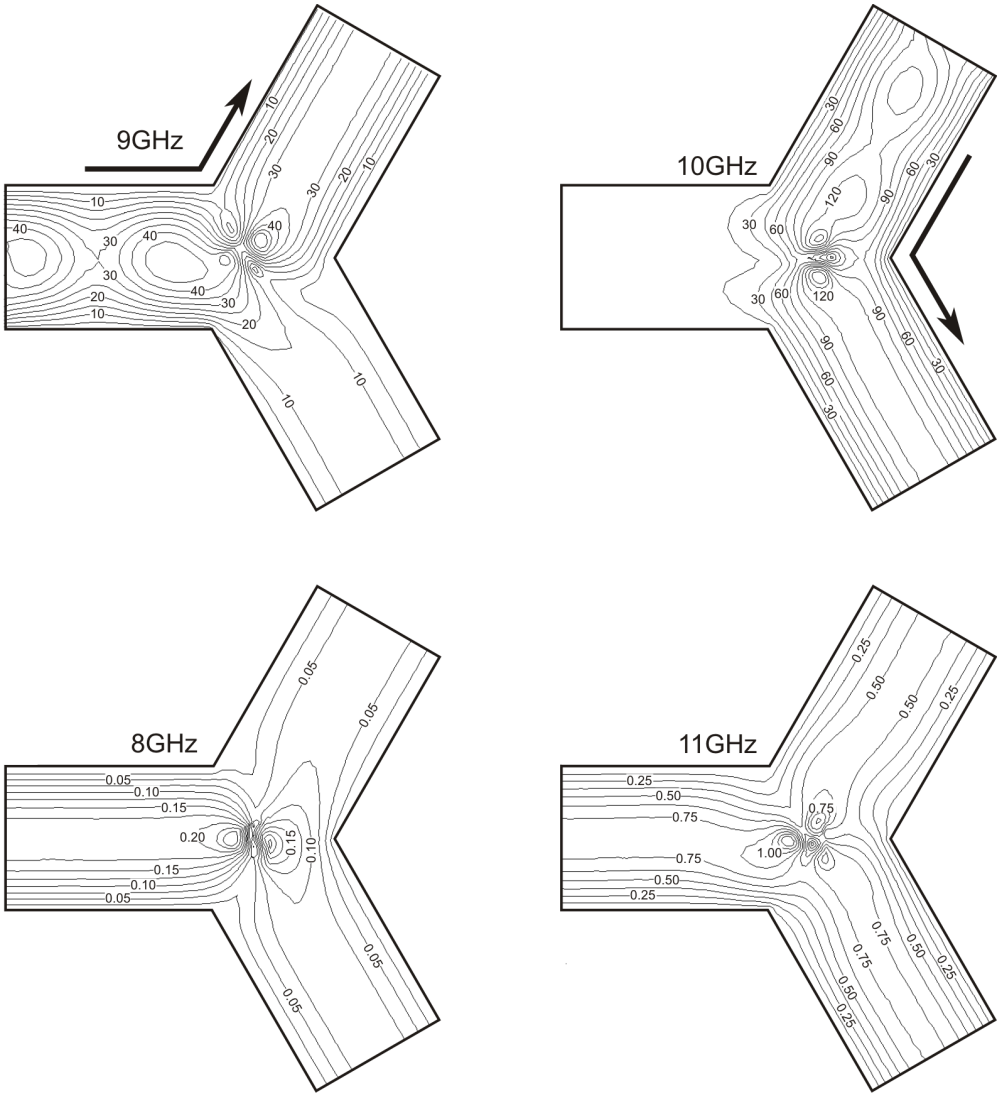

Figure 4.11: Electric field $\left(\frac{\text{kV}}{\text{m}}\right)$ distribution for the third order intermodulation problem, at 9 GHz, 10 GHz, and at in-band IMPs frequencies 8 and 11 GHz.

It is worth noticing that as the harmonic order grows, higher order TE modes at ports boundaries become propagating, and hence 10 modes [101] have been retained to accurately compute the power balance.

Even if the exact (continuous) solution cannot be achieved, table 4.1 shows that the computation of in-band third order products, considering up to all the third order products, leads to a maximum error of less than 0.2 %. In this case, Figs. 4.12 and 4.13 shows the resulting power amplitudes as a function of frequency for the two in-band third-order IMPs for different signal and interferent power levels. The power delivered to IMPs is in good agreement with those reported in [80].

Also here a Schur based domain decomposition (DD) scheme, which provides the same solution of the standard full system iteration scheme, allows to speed up the computations. The acceleration of the DD solver, defined as the ratio between the standard scheme times (assembly and solve for whole domain at each iteration)

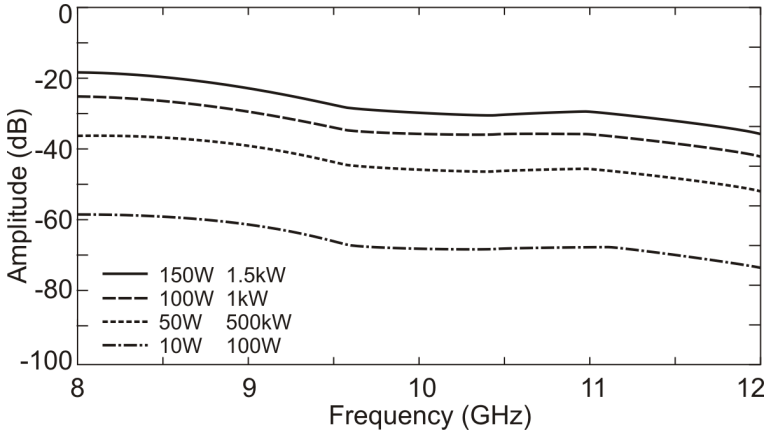

Figure 4.12: Intermodulation product power at $2f_s - f_i$ ($f_i = 10$ GHz).

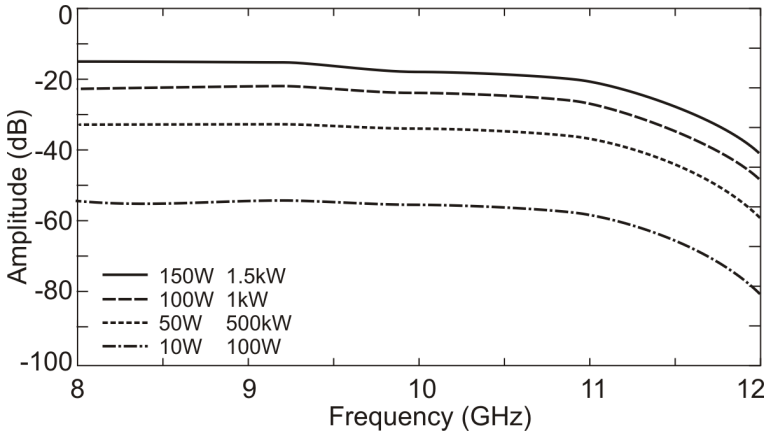

Figure 4.13: Intermodulation product power at $2f_i - f_s$ ($f_i = 10$ GHz).

and the DD times (assembly and solve for whole domain only at first iteration, then assembly and solve for nonlinear subdomains only), is reported in Fig. 4.15. Sparse direct solvers of a Matlab® implementation for both standard full and DD schemes have been employed to perform the computations. All over the frequency sweep, the FFT-based algorithm employed to compute nonlinear materials testing has required noticeably different amount of times, bound to differences in the number of iterations required, leading to different values of acceleration for the chosen frequency points. The time step required to accurately compute the testing integrals strongly depend on the difference between signal and interferer frequencies. However, 45 % to 60 % average speed-up have been noticed within the signal bandwidth.

Further tests are performed to assess the efficiency of the method, both for 2 and 5 subdomains (only 1 with nonlinear ferrite), while increasing the number of degrees of freedom (hence the non-zero entries of the system matrix $[A]$) by increasing the elements order from first to fourth (Fig. 4.14 and 4.16).

The higher is the number of linear subdomains, the smaller are the submatrices of the linear subdomains, leading to improved acceleration. Furthermore, acceleration grows logarithmically with the polynomial order, that is with the number of non-zero

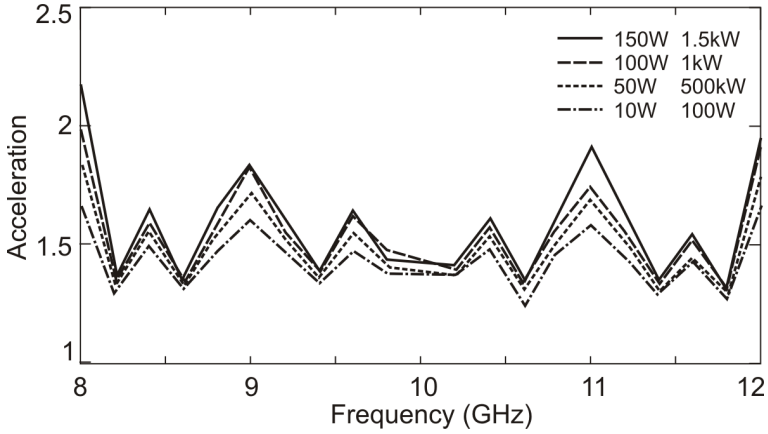

Figure 4.14: Acceleration of the DD scheme vs conventional scheme. Linear elements have been considered, leading to 700 degrees of freedom and 8100 non-zero entries of [A].

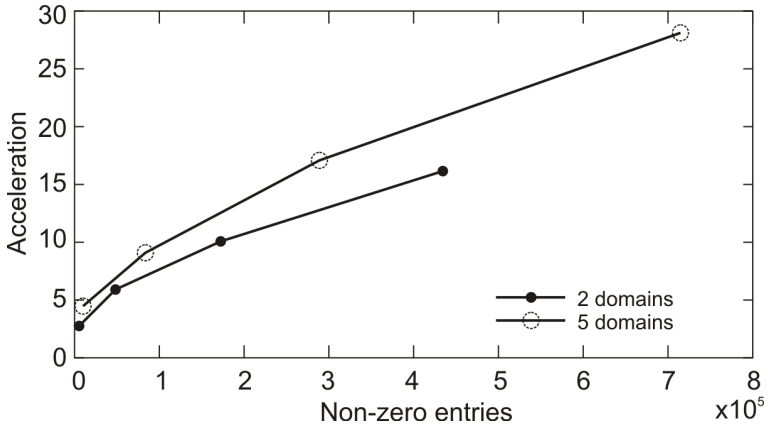

Figure 4.15: Acceleration of the DD scheme vs standard full scheme as a function of non-zero entries of [A].

entries of the system matrix.

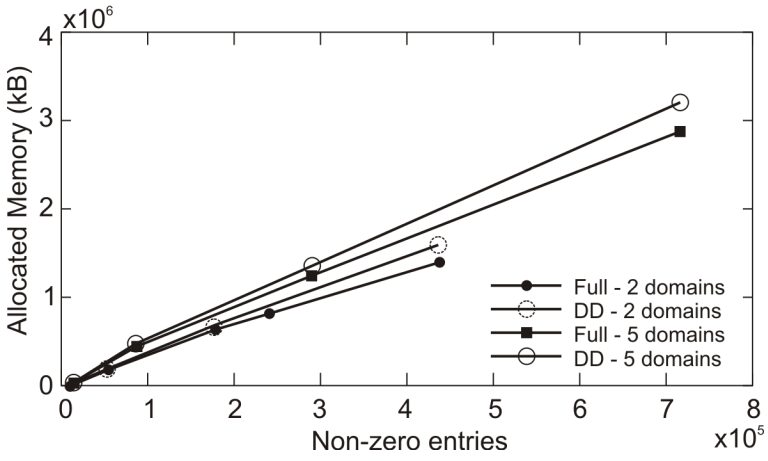

Figure 4.16: Allocated memory (stored and dynamically freed) as a function of non-zero entries of [A].

Increasing the number of subdomains generally leads to higher allocated memory. This is mainly due to an increase of geometrical and finite elements unknowns reordering information, which is kept in both standard full and DD schemes. DD schemes require more memory to store the Schur complement matrices and solve for related unknowns.

4.4.3 Barium strontium titanate thin film coplanar waveguide

The present test represent a first attempt to analyze the validity of the HBFE method to a 3D structure whose high-order harmonics measurements have been reported in [88].

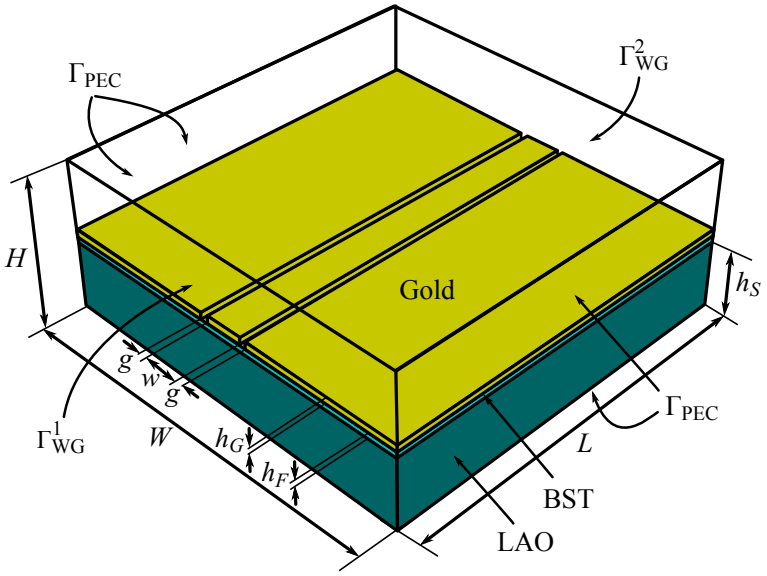

Figure 4.17: Sketch of the coplanar waveguide as the domain Ω of HBFE analysis and relative boundaries Γ_{PEC} for the perfect electric conductor shield and waveports boundary conditions on Γ^1_{WG} and Γ^2_{WG}. The center conductor of the strip is $w = 20$ μm with $g = 20$ μm gaps on both sides and $h_G = 0.3$ μm of thickness. The thickness of the BST thin-film is $h_F = 400$ nm-thick and that of the LAO substrate is $h_S = 500$ μm. Dimensions of the box are $W = 2$ mm, $H = 1$ mm and $L = 0.42$ mm.

It consists of a coplanar waveguide (CPW) transmission line as depicted in Fig. 4.17. A 400 nm $Ba_{0.3}Sr_{0.7}TiO_3$ (BST) thin film grown on a $LaAlO_3$ (LAO) substrate. [88] does not report the employed LAO substrate thickness, hence a typical value of 0.5 μm [161] have been used. The gold conductors that constitutes the CPW are 0.3 μm-thick. The center conductor linewidth is of 20 μm and so are the gaps around. The width (2 mm) and height (1 mm) of the shielding box walls are chosen far enough from the line such that the impedance of the dominant TEM mode slightly depend on the perfect electric walls, the dominant coplanar mode field being concentrated within the gaps. Furthermore, the mesh of the structure is such that the coupling between the coplanar mode and other modes such as the stripline mode

and higher-order hibrid TE and TM modes is minimized within the frequency range of analysis. Material properties for the linear case are set as reported in table 4.2, where $\bar{\epsilon}'$ and $\bar{\epsilon}''$ are, respectively, the real and imaginary parts of the permittivity.

Material	$\bar{\epsilon}'_r$	$\bar{\mu}_r$	$\bar{\sigma}\ \left[\frac{\mathrm{S}}{\mathrm{m}}\right]$	$\tan\delta = \frac{\bar{\epsilon}''}{\bar{\epsilon}'}$
LAO	24	1	0	0
BST	475	1	0	0.0842
Gold	1	0.99996	$4.1\ 10^7$	0
Vacuum	1	1	0	0

Table 4.2: Material properties for the linear CPW.

In the nonlinear case, the BST film has the following Kerr-like permittivity (real part)

$$\tilde{\varepsilon'}_r(\mathbf{E},\mathbf{r}) = \bar{\varepsilon}'_r\left(1+\alpha_2\,|\mathbf{E}|^2\right), \qquad \mathbf{r}\in\Omega_2 \tag{4.4.9}$$

with $\alpha_2 = -5.01\ 10^{-14}\ \frac{\mathrm{m}^2}{\mathrm{V}^2}$ as derived from measurements in [88]. The imaginary part has been left independent from the field intensity.

A first, linear, analysis is conducted with first order curl-conforming basis functions to ensure proper simulations setups. The choice of the basis order is motivated by the high mesh density within BST and gold materials, principally imposed by the thickness of these layers. The mesh is composed of 98 216 tetrahedra, 37 119 in the LAO substrate, 23 007 in the BST film, 13 441 in the gold strips and the remaining 24 619 in the vacuum. Three modes (transfinite element method) have been retained in the analysis while feeding the CPW only with the coplanar mode. The assembly has led to 112 899 unknowns, which is relatively high if we think of the electrical size. As introduced in chapter 1, this is the case of electrically small geometries and high permittivities that causes a small problem to become large. The scattering parameters over the frequency range $[2, 10]$ GHz are reported in Fig. 4.18. In particular, these show that the overall crosstalk between modes is below -35 dB all over the range. Furthermore, the stripline mode of the structure should be propagating if feeded at those frequencies.

Figs. 4.19, 4.20 and 4.21 show, respectively, the electric field when the coplanar, stripline and first hibrid TE mode are feeding the CPW at 6 GHz. The fields distributions clearly show that they are propagating, however, orthogonality between modes is such that the crosstalk remains below -35 dB.

Finally, the nonlinear analysis is conducted with harmonic orders 1 and 3 ($P = 3$) for different impinging powers P_1 at waveport 1: 10^{-3}, 10^{-2}, 10^{-1}, 1, 2, 5 and 10 W of coplanar mode power at 2 GHz. A residual tolerance of 10^{-5} as been chosen. The assembly led to 225 798 unknowns and 4 iterations at most were required to tackle the iterative solution for an impinging power of 10 W. The memory and time requirements for each assembly and solve (non-symmetric system) were of 4318 MB

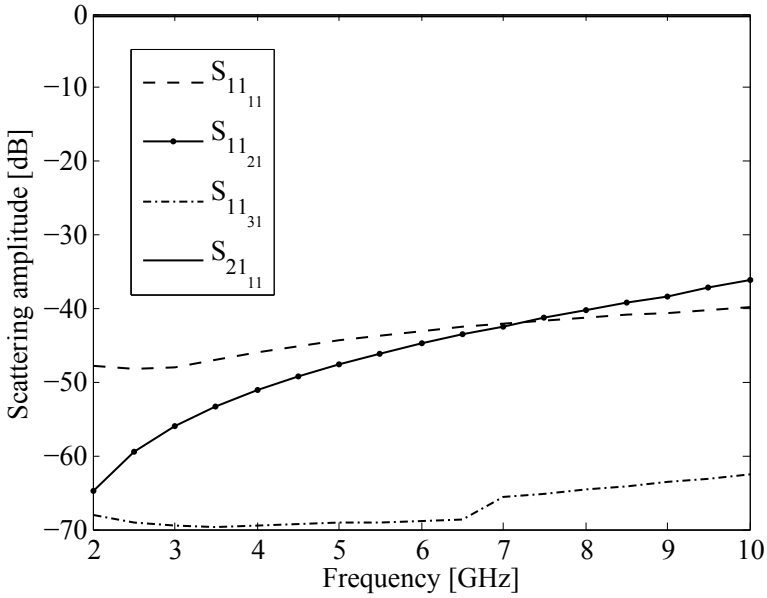

Figure 4.18: Spectral response of the CPW ($S_{\text{port1}|\text{port2}_{\text{mode1}|\text{mode2}}}$).

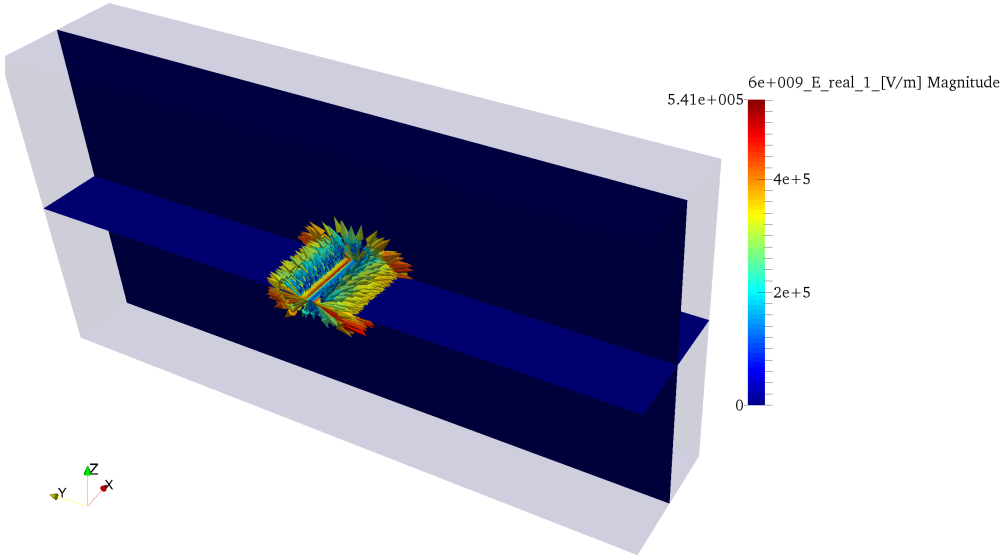

Figure 4.19: Coplanar mode traveling through the CPW at 6 GHz.

and almost 306 s for the slowest iteration. In fact, the first assembled system is almost block diagonal and hence contains less non-zero entries. Only 2335 MB and 267 s were required for the first iteration. The results of the power sweep are shown in Fig. 4.22. The good agreement between the HBFE results, with only $P = 3$, and measurements confirms the validity of the method. Fig. 4.23 shows the total electric field computed contemporaneously at 2 GHz and 6 GHz (3$^{\text{rd}}$ harmonic).

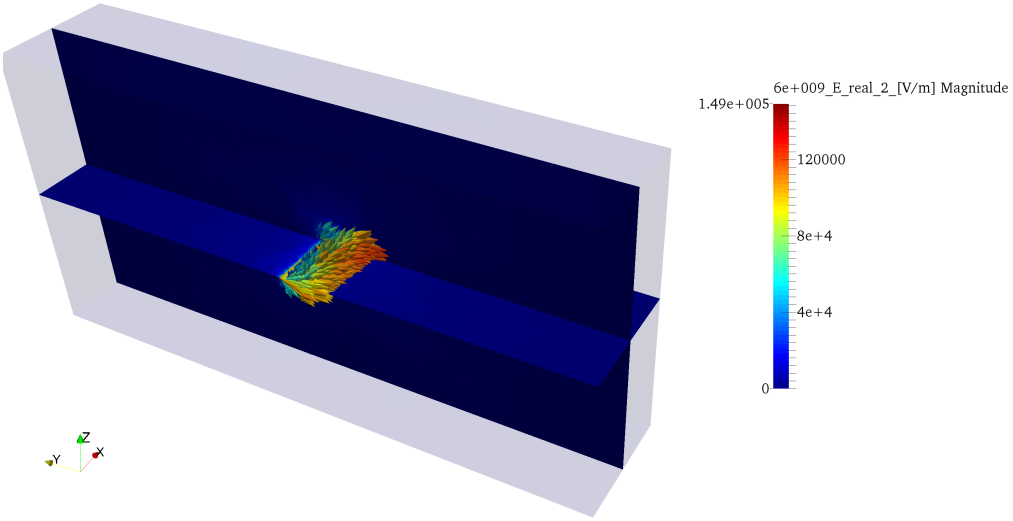

Figure 4.20: Stripline mode traveling through the CPW at 6 GHz.

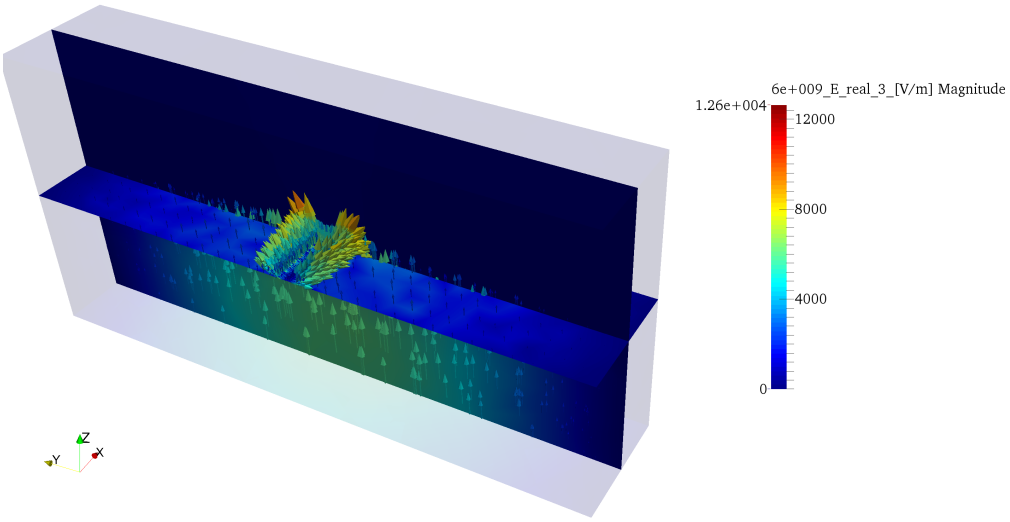

Figure 4.21: First hibrid TE mode traveling through the CPW at 6 GHz.

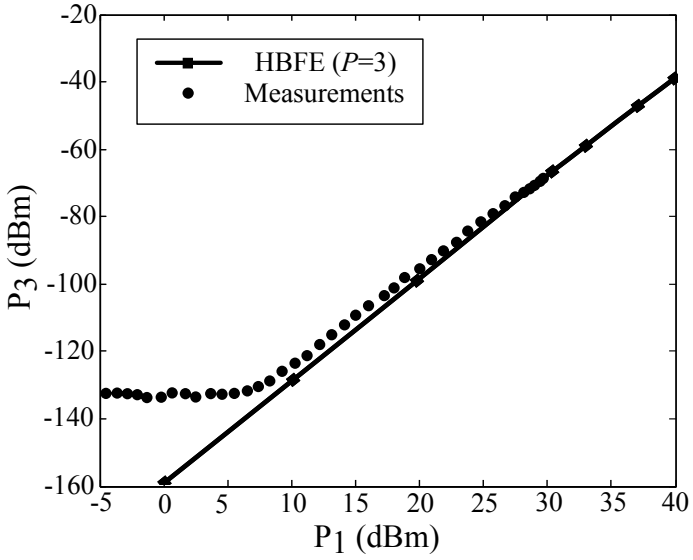

Figure 4.22: Third harmonic spurious power computed with the HBFE. Comparisons are with measurements reported in Mateu et al. 2006.

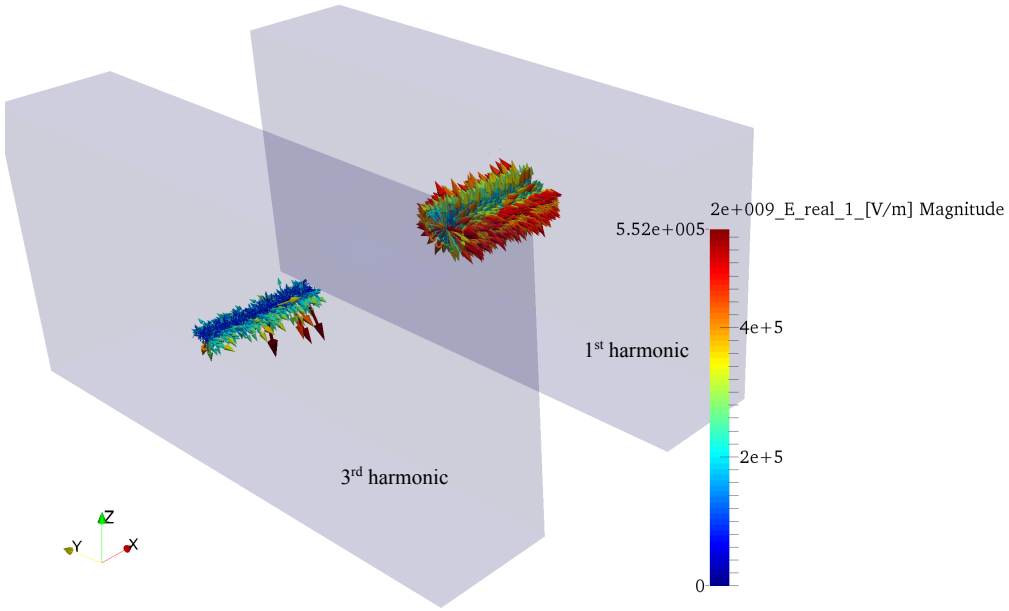

Figure 4.23: Fundamental (2 GHz) and third harmonic electric field distributions computed by the HBFE with 1 W coplanar mode feeding the CPW.

Chapter 5

Conclusion

This chapter draws some conclusions from the work presented in this dissertation, and provides a comprehensive outlook.

5.1 Summary

The present work has allowed to build up various finite element solvers for the wave equation that extend the capabilities of widely available, commercial or not, similar solvers.

In the first chapter, the finite element method for the wave equation have been introduced, and its implementation in the FES-3D package has been validated by an extensive comparison with a commercial package. Several boundary conditions have been tested in order to allow the analysis of many electromagnetic problems, for instance waveguide devices, antenna radiation and electromagnetic scattering of arbitrarily shaped objects. Due to the finite element approach, material properties can be easily treated in a rigorous manner.

Then, in the second chapter, two domain decomposition methods have been analyzed adding their formulations to the validated FES-3D, looking forward to apply the method to large electromagnetic problems. The direct Schur complement approach has demonstrated extremely high computational accuracies, while requiring high simulation times to assemble the Schur complement matrix. The finite element tearing and interconnecting dual-primal (FETI-DP) approach, whit Robin-Robin transmission conditions have demonstrated a better decoupling between subdomains and a better iterative behavior when used as preconditioner for a Krylov subspace iterative solver. However, the Schur complement based domain decomposition allow for a better waveports truncation method, the transfinite element method, while the FETI-DP requires a the waveports not to be shared between subdomains in order to maintain subproblems decoupling. The behavior of several domain decomposition preconditioners for iterative solvers have been analyzed, and a linear complexity could be achieved for memory requirements, while the simulation times behave al-

most as those of direct solvers.

In the third chapter, an accurate approach for solving nonlinear microwave problems have been proposed with the first documented application of the harmonic balance finite element method to the wave equation. Several tests have been conducted, first with FES-2D then with FES-3D, to assess the spurious fields generation by nonlinear dielectrics and nonlinear ferrites. The results almost match the measurements reported in literature.

5.2 Outlook

During the years dedicated to the research illustrated within this dissertation, many open problems and relevant fields of application of the method have appeared.

First, the Schur compement based Gauss-Seidel preconditioner could be improved by a mixing of the direct approach and Krylov subspace approach. For instance, if one could replace the $[A_{\Gamma\Gamma}]$ block of the preconditioner with an approximate Schur complement $[\tilde{S}]$, then the number of iterations required in the GMRES(r) solver would rapidly decrease, as it has been noticed that the substitution of $[A_{\Gamma\Gamma}] \leftarrow [S]$ only requires a couple of iterations to converge to numerical error. Its approximation, with the right trade-off to keep the block easily invertible, would lead to an optimal domain decomposition preconditioner, and hence the rapid solution of very large problems, while keeping the accuracy of multi-mode transfinite element method on waveports.

Also, the harmonic balance finite element method for the wave equation open the path to nonlinear problems currently solved only by non-rigorous methods. Among these there are all the passive intermodulation problems that occur at microwave frequencies. This is still one challenging problem that is still tackled without the direct solution of Maxwell's equations [162, 163] and hence all models strictly depend on the employed device type. Also, the nonlinearities of materials at microwave frequencies can be exploited to design electronically reconfigurable devices [164–166]. Coupling of electrostatic and microwave formulations may lead to accurate modeling of these devices. At optical frequencies, nanoparticles of barium titanate oxides have demonstrated interesting capabilities of subwavelength coherent light generation when illuminated by non-coherent light [167]. Accurate modeling of these nanoparticles, combined with a domain decomposition method to extend the problem dimensions may lead to very interesting photonics and biosensing applications. Same behavior is found with the emergent nanowires [168].

These were some of the most modern challenging problems that the results of this dissertation may allow for straightforward solution, in some cases upon combining both domain decomposition schemes with nonlinear analyzes.

Bibliography

[1] R. Courant, "Variational methods for the solution of problems of equilibrium and vibrations," *Bulletin of the American Mathematical Society*, vol. 49, no. 1, p. 23, 1943.

[2] P. P. Silvester, "Finite-element solution of homogeneous waveguide problems," *Alta Frequenza*, vol. 38, pp. 313–317, May 1969.

[3] R. Coccioli, T. Itoh, G. Pelosi, and P. P. Silvester, "Finite-element methods in microwaves: A selected bibliography," *Antennas and Propagation Magazine, IEEE*, vol. 38, no. 6, pp. 34–48, 1996.

[4] Computer Simulation Technology, "CST Microwave Studio," Dec. 2013. [Online]. Available: https://www.cst.com/Applications/MWandRF

[5] SPEAG, "SEMCAD X," Dec. 2013. [Online]. Available: http://www.speag.com/products/semcad/overview/

[6] COMSOL, "RF Module," Dec. 2013. [Online]. Available: http://www.comsol.com/rf-module

[7] Ansys, "HFSS," Dec. 2013. [Online]. Available: http://www.ansys.com/Products/Simulation+Technology/Electromagnetics

[8] EM Software & Systems, "FEKO," Dec. 2013. [Online]. Available: http://www.feko.info/

[9] R. Garg, *Analytical and Computational Methods in Electromagnetics*. Norwood, MA: Artech House, Inc., 2008.

[10] D. B. Davidson, *Computational Electromagnetics for RF and Microwave Engineering*, 2nd ed. New York: Cambridge University Press, 2011.

[11] T. Rylander, P. Ingelström, and A. Bondeson, *Computational Electromagnetics*, 2nd ed. New York: Springer Science and Business Media, 2011.

[12] J. Lee, "The maturity of computational electromagnetics: Are we there yet?" in *Antennas and Propagation (EUCAP), Proceedings of the 5th European Conference on*. IEEE, 2011, pp. 3011–3014.

[13] R. Mittra, "A look at some challenging problems in computational electromagnetics," *Antennas and Propagation Magazine, IEEE*, vol. 46, no. 5, pp. 18–32, 2004.

[14] I. Tsukerman, *Computational Methods for Nanoscale Applications, Particles, Plasmons and Waves*, D. J. Lockwood, Ed. Berlin: Springer, 2008.

[15] I. Tsukerman and A. Plaks, "Comparison of accuracy criteria for approximation of conservative fields on tetrahedra," *Magnetics, IEEE Transactions on*, vol. 34, no. 5, pp. 3252–3255, 1998.

[16] P. M. Goorjian and A. Taflove, "Direct time integration of maxwell's equations in nonlinear dispersive media for propagation and scattering of femtosecond electromagnetic solitons," *Optics letters*, vol. 17, no. 3, pp. 180–182, 1992.

[17] R. W. Ziolkowski and J. B. Judkins, "Full-wave vector Maxwell equation modeling of the self-focusing of ultrashort optical pulses in a nonlinear Kerr medium exhibiting a finite response time," *Journal of the Optical Society of America B*, vol. 10, no. 2, pp. 186–198, 1993.

[18] ——, "Nonlinear finite-difference time-domain modeling of linear and nonlinear corrugated waveguides," *Journal of the Optical Society of America B*, vol. 11, no. 9, pp. 1565–1575, 1994.

[19] R. M. Joseph and A. Taflove, "FDTD Maxwell's equations models for nonlinear electrodynamics and optics," *Antennas and Propagation, IEEE Transactions on*, vol. 45, no. 3, pp. 364–374, 1997.

[20] F. L. Teixeira, "Time-domain finite-difference and finite-element methods for Maxwell equations in complex media," *Antennas and Propagation, IEEE Transactions on*, vol. 56, no. 8, pp. 2150–2166, 2008.

[21] P. Sasanpour, A. Shahmansouri, and B. Rashidian, "Analysis of third harmonic generation and four wave mixing in gold nanostructures by nonlinear finite difference time domain," *Journal of Nanoscience and Nanotechnology*, vol. 10, no. 11, pp. 7179–7182, 2010.

[22] N. Potravkin, I. Perezhogin, and V. Makarov, "Numerical solution of Maxwell equations by a finite-difference time-domain method in a medium with frequency and spatial dispersion," *Physical Review E*, vol. 86, no. 5, p. 056706, 2012.

[23] J. Frances Monllor, J. Tervo, and C. Neipp, "Split-field finite-difference time-domain scheme for Kerr-type nonlinear periodic media," *Progress In Electromagnetics Research*, vol. 134, pp. 559–579, 2013.

[24] P. Silvester and M. V. Chari, "Finite element solution of saturable magnetic field problems," *Power Apparatus and Systems, IEEE Transactions on*, no. 7, pp. 1642–1651, 1970.

[25] S. Yamada and K. Bessho, "Harmonic field calculation by the combination of finite element analysis and harmonic balance method," *Magnetics, IEEE Transactions on*, vol. 24, no. 6, pp. 2588–2590, 1988.

[26] S. Yamada, K. Bessho, and J. Lu, "Harmonic balance finite element method applied to nonlinear AC magnetic analysis," *Magnetics, IEEE Transactions on*, vol. 25, no. 4, pp. 2971–2973, 1989.

[27] S. Yamada, P. Biringer, and K. Bessho, "Calculation of nonlinear eddy-current problems by the harmonic balance finite element method," *Magnetics, IEEE Transactions on*, vol. 27, no. 5, pp. 4122–4125, 1991.

[28] J. Gyselinck, P. Dular, C. Geuzaine, and W. Legros, "Harmonic-balance finite-element modeling of electromagnetic devices: a novel approach," *Magnetics, IEEE Transactions on*, vol. 38, no. 2, pp. 521–524, 2002.

[29] R. Pascal, P. Conraux, and J.-M. Bergheau, "Coupling between finite elements and boundary elements for the numerical simulation of induction heating processes using a harmonic balance method," *Magnetics, IEEE Transactions on*, vol. 39, no. 3, pp. 1535–1538, 2003.

[30] X. Zhao, J. Lu, L. Li, Z. Cheng, and T. Lu, "Analysis of the saturated electromagnetic devices under DC bias condition by the modified harmonic balance finite element method," in *Electromagnetic Field Computation (CEFC), 2010 14th Biennial IEEE Conference on*. IEEE, 2010, pp. 1–1.

[31] ——, "Analysis of the DC bias phenomenon by the harmonic balance finite-element method," *Power Delivery, IEEE Transactions on*, vol. 26, no. 1, pp. 475–485, 2011.

[32] O. Biro, K. Preis, and K. R. Richter, "Various FEM formulations for the calculation of transient 3D eddy currents in nonlinear media," *Magnetics, IEEE Transactions on*, vol. 31, no. 3, pp. 1307–1312, 1995.

[33] A. Gupta, F. G. Gustavson, M. Joshi, G. Karypis, and V. Kumar, "Design and implementation of a scalable parallel direct solver for sparse symmetric positive definite systems: preliminary results," in *Conference on Parallel Processing for Scientific Computing – PPSC, SIAM*, 1997.

[34] T. H. Cormen, C. E. Leiserson, R. L. Rivest, and C. Stein, *Introduction to Algorithms*, 3rd ed. Cambridge, MA: The MIT Press, 2009, ch. 28, p. 828.

[35] W. L. Briggs, V. E. Henson, and S. F. McCormick, *A Multigrid Tutorial*, 2nd ed. Philadelphia, PA: SIAM, 2000.

[36] V. Hill, O. Farle, and R. Dyczij-Edlinger, "A stabilized multilevel vector finite-element solver for time-harmonic electromagnetic waves," *Magnetics, IEEE Transactions on*, vol. 39, no. 3, pp. 1203–1206, 2003.

[37] P. Ingelström, "Higher order finite elements and adaptivity in computational electromagnetics," Ph.D. dissertation, Chalmers University, 2004.

[38] S. Gheorghe, "On multigrid methods for solving electromagnetic scattering problems," Ph.D. dissertation, Kiel Christian-Albrechts-Universität, 2005.

[39] Y. Zhu and A. C. Cangellaris, *Mutigrid Finite Element Methods for Electromagnetic Field Modeling*, ser. IEEE Press on Electromagnetic Wave Theory. Hoboken, NJ: John Wiley and Sons, Inc., 2006.

[40] V. Hill, "Schnelle finite-elemente-methoden zur simulation elektromagnetischer felder im frequenzbereich," Ph.D. dissertation, Universität des Saarlandes, 2006.

[41] P. Ingelström, V. Hill, and R. Dyczij-Edlinger, "Comparison of hierarchical basis functions for efficient multilevel solvers," *IET Science, Measurement & Technology*, vol. 1, no. 1, pp. 48–52, 2007.

[42] F. Vipiana, P. Pirinoli, and G. Vecchi, "A multiresolution method of moments for triangular meshes," *Antennas and Propagation, IEEE Transactions on*, vol. 53, no. 7, pp. 2247–2258, 2005.

[43] M. A. Khorrami, P. Dehkhoda, R. M. Mazandaran, and S. Sadeghi, "Fast shielding effectiveness calculation of metallic enclosures with apertures using a multiresolution method of moments technique," *Electromagnetic Compatibility, IEEE Transactions on*, vol. 52, no. 1, pp. 230–235, 2010.

[44] A. Quarteroni and A. Valli, *Domain Decomposition Methods for Partial Differential Equations*. Oxford: Oxford University Press, 1999.

[45] A. Toselli and O. Widlund, *Domain Decomposition Methods - Algorithms and Theory*. Berlin: Springer-Verlag, 2005.

[46] T. P. A. Mathew, *Domain Decomposition Methods for the Numerical Solution of Partial Differential Equations*. Berlin: Springer-Verlag, 2008.

[47] Y. Li and J.-M. Jin, "A vector dual-primal finite element tearing and interconnecting method for solving 3-D large-scale electromagnetic problems," *Antennas and Propagation, IEEE Transactions on*, vol. 54, no. 10, pp. 3000–3009, 2006.

[48] D.-K. Sun, K. Longtin, J.-F. Lee, and Z. Cendes, "A nonconforming domain decomposition method with a high order basis for the time-harmonic maxwell equation," in *Antennas and Propagation Society International Symposium, 2005 IEEE*, vol. 3. IEEE, 2005, pp. 40–43.

[49] M. Vouvakis, K. Zhao, S.-M. Seo, and J.-F. Lee, "A domain decomposition approach for non-conformal couplings between finite and boundary elements for unbounded electromagnetic problems in $\mathbb{R}^3$," *Journal of Computational Physics*, vol. 225, no. 1, pp. 975–994, 2007.

[50] A. A. Rodriguez and L. Gerardo-Giorda, "New nonoverlapping domain decomposition methods for the harmonic maxwell system," *SIAM Journal on Scientific Computing*, vol. 28, no. 1, pp. 102–122, 2006.

[51] K. Zhao, M. N. Vouvakis, and J.-F. Lee, "Solving electromagnetic problems using a novel symmetric FEM-BEM approach," *Magnetics, IEEE Transactions on*, vol. 42, no. 4, pp. 583–586, 2006.

[52] A. Barka and P. Caudrillier, "Domain decomposition method based on generalized scattering matrix for installed performance of antennas on aircraft," *Antennas and Propagation, IEEE Transactions on*, vol. 55, no. 6, pp. 1833–1842, 2007.

[53] K. Zhao, V. Rawat, and J.-F. Lee, "A domain decomposition method for electromagnetic radiation and scattering analysis of multi-target problems," *Antennas and Propagation, IEEE Transactions on*, vol. 56, no. 8, pp. 2211–2221, 2008.

[54] V. Rawat and J.-F. Lee, "A domain decomposition preconditioner for time-harmonic electromagnetics," in *Antennas and Propagation Society International Symposium, 2008. AP-S 2008. IEEE*. IEEE, 2008, pp. 1–4.

[55] L. Grasedyck, R. Kriemann, and S. Le Borne, "Domain decomposition based $\mathcal{H}$-lu preconditioning," *Numerische Mathematik*, vol. 112, no. 4, pp. 565–600, 2009.

[56] V. Rawat, "Finite element domain decomposition with second order transmission conditions for time-harmonic electromagnetic problems," Ph.D. dissertation, Ohio State University, 2009.

[57] O. Ozgun and M. Kuzuoglu, "Iterative leap-field domain decomposition method: a domain decomposition finite element algorithm for 3D electromagnetic boundary value problems," *IET Microwaves, Antennas & Propagation*, vol. 4, no. 4, pp. 543–552, 2010.

[58] Z. Peng and J.-F. Lee, "Non-conformal domain decomposition method with second-order transmission conditions for time-harmonic electromagnetics," *Journal of Computational Physics*, vol. 229, no. 16, pp. 5615–5629, 2010.

[59] A. Takei, S.-I. Sugimoto, M. Ogino, S. Yoshimura, and H. Kanayama, "Full wave analyses of electromagnetic fields with an iterative domain decomposition method," *Magnetics, IEEE Transactions on*, vol. 46, no. 8, pp. 2860–2863, 2010.

[60] Z. Peng, X.-C. Wang, and J.-F. Lee, "Integral equation based domain decomposition method for solving electromagnetic wave scattering from non-penetrable objects," *Antennas and Propagation, IEEE Transactions on*, vol. 59, no. 9, pp. 3328–3338, 2011.

[61] Y. Shao, Z. Peng, and J.-F. Lee, "Full-wave real-life 3-D package signal integrity analysis using nonconformal domain decomposition method," *Microwave Theory and Techniques, IEEE Transactions on*, vol. 59, no. 2, pp. 230–241, 2011.

[62] X. Wang, "A domain decomposition method for analysis of three-dimensional large-scale electromagnetic compatibility problems," Ph.D. dissertation, Ohio State University, 2012.

[63] O. B. Widlund and D. Keyes, *Domain decomposition methods in science and engineering XVI*. Berlin: Springer, 2007, vol. 55.

[64] W. C. Chew, J.-M. Jin, E. Michielssen, and J. Song, Eds., *Fast and Efficient Algorithms in Computational Electromagnetics*. Norwood, MA: Artech House, Inc., 2001.

[65] N. A. Gumerov and R. Duraiswami, *Fast Multipole Methods for the Helmholtz Equation in Three Dimensions*. Kidlington, Oxford: Elsevier Ltd., 2004.

[66] O. Farle, V. Hill, P. Nickel, and R. Dyczij-Edlinger, "Multivariate finite element model order reduction for permittivity or permeability estimation," *Magnetics, IEEE Transactions on*, vol. 42, no. 4, pp. 623–626, 2006.

[67] L. Ntibarikure, "Model order reduction in finite element analysis of phased array antennas," in *Numero Speciale 8 - Serie di Elettromagnetismo su "XIX Riunione Nazionale di Elettromagnetismo," Atti della "Fondazione Giorgio Ronchi"*, vol. LXVIII, no. 4, Jul–Aug 2012, pp. 97–102.

[68] V. Prakash and R. Mittra, "Characteristic basis function method: A new technique for efficient solution of method of moments matrix equations," *Microwave and Optical Technology Letters*, vol. 36, no. 2, pp. 95–100, 2003.

[69] A. Bayliss, M. Gunzburger, and E. Turkel, "Boundary conditions for the numerical solution of elliptic equations in exterior regions," *SIAM Journal on Applied Mathematics*, vol. 42, no. 2, pp. 430–451, 1982.

[70] C. W. Crowley, P. Silvester, and J. Hurwitz, H., "Covariant projection elements for 3D vector field problems," *Magnetics, IEEE Transactions on*, vol. 24, no. 1, pp. 397–400, 1988.

[71] J.-P. Berenger, "A perfectly matched layer for the absorption of electromagnetic waves," *Journal of Computational Physics*, vol. 114, no. 2, pp. 185 – 200, 1994.

[72] X.-B. Xu and J. Ao, "A hybrid integral and differential equation method solution of scattering of tm excitation by buried inhomogeneous cylinders," *Progress In Electromagnetics Research*, vol. 15, pp. 165–189, 1997.

[73] K. Zhao and M. Commens, "Efficient full-wave electromagnetic simulation with hybrid finite element-boundary integral," in *Microwave Conference (EuMC), 2011 41st European*. IEEE, 2011, pp. 171–174.

[74] D. M. Pozar, *Microwave engineering*. New York, NY: Wiley, 1998.

[75] J. D. Adam, L. E. Davis, G. F. Dionne, E. F. Schloemann, and S. N. Stitzer, "Ferrite devices and materials," *Microwave Theory and Techniques, IEEE Transactions on*, vol. 50, no. 3, pp. 721–737, 2002.

[76] H. Suhl, "The nonlinear behavior of ferrites at high microwave signal levels," *Proceedings of the IRE*, vol. 44, no. 10, pp. 1270–1284, 1956.

[77] ——, "The theory of ferromagnetic resonance at high signal powers," *Journal of Physics and Chemistry of Solids*, vol. 1, no. 4, pp. 209–227, 1957.

[78] G. Bailey and A. Ehrlich, "A study of RF nonlinearities in Nickel," *Journal of Applied Physics*, vol. 50, no. 1, pp. 453–461, 1979.

[79] Y. Wu, W. H. Ku, and J. E. Erickson, "A study of nonlinearities and intermodulation characteristics of 3-port distributed circulators," *Microwave Theory and Techniques, IEEE Transactions on*, vol. 24, no. 2, pp. 69–77, 1976.

[80] H. How, C. Vittoria, and R. Schmidt, "Nonlinear intermodulation coupling in ferrite circulator junctions," *Microwave Theory and Techniques, IEEE Transactions on*, vol. 45, no. 2, pp. 245–252, 1997.

[81] J. Sanford, "Passive intermodulation considerations in antenna design," in *Antennas and Propagation Society International Symposium, 1993. AP-S. Digest*, 1993, pp. 1651–1654 vol.3.

[82] F. Arazm and F. A. Benson, "Nonlinearities in metal contacts at microwave frequencies," *Electromagnetic Compatibility, IEEE Transactions on*, no. 3, pp. 142–149, 1980.

[83] M. B. Amin and F. A. Benson, "Coaxial cables as sources of intermodulation interference at microwave frequencies," *Electromagnetic Compatibility, IEEE Transactions on*, no. 3, pp. 376–384, 1978.

[84] C. D. Bond, C. S. Guenzer, and C. A. Carosella, "Intermodulation generation by electron tunneling through aluminum-oxide films," *Proceedings of the IEEE*, vol. 67, no. 12, pp. 1643–1652, 1979.

[85] J. Scott, M. Azuma, C. Paz de Araujo, L. McMillan, M. Scott, and T. Roberts, "Dielectric breakdown in high-ε films for ULSI DRAMs: II. barium-strontium titanate ceramics," *Integrated ferroelectrics*, vol. 4, no. 1, pp. 61–84, 1994.

[86] T. M. Shaw, Z. Suo, M. Huang, E. Liniger, R. B. Laibowitz, and J. D. Baniecki, "The effect of stress on the dielectric properties of barium strontium titanate thin films," *Applied Physics Letters*, vol. 75, no. 14, pp. 2129–2131, 1999.

[87] A. Kozyrev, T. Samoilova, O. Soldatenkov, O. Buslov, E. Hollmann, V. E. Loginov, A. M. Prudan, G. Koepf, K. Mueller, T. Rivkin, and Z. Zhang, "Ferroelectric films: nonlinear properties and applications in microwave devices," in *Microwave Conference, 1997. 27th European*, vol. 2, 1997, pp. 1020–1025.

[88] J. Mateu, J. Booth, S. Schima, C. Collado, D. Seron, and J. O'Callaghan, "Measurements and analysis of microwave nonlinearities in ferroelectric thin film transmission lines," in *Microwave Symposium Digest, 2006. IEEE MTT-S International*, 2006, pp. 1622–1625.

[89] J. Mateu, J. Booth, and S. Schima, "Frequency tuning and spurious signal generation at microwave frequencies in ferroelectric $SrTiO_3$ thin-film transmission lines," *Microwave Theory and Techniques, IEEE Transactions on*, vol. 55, no. 2, pp. 391–396, 2007.

[90] A. Giere, P. Scheele, Y. Zheng, and R. Jakoby, "Characterization of the field-dependent permittivity of nonlinear ferroelectric films using tunable coplanar lines," *Microwave and Wireless Components Letters, IEEE*, vol. 17, no. 6, pp. 442–444, 2007.

[91] K. Takeda, T. Muraishi, T. Hoshina, H. Takeda, and T. Tsurumi, "Dielectric tunability and electro-optic effect of $Ba_{0.5}Sr_{0.5}TiO_3$ thin films," *Journal of Applied Physics*, vol. 107, no. 7, p. 074105, 2010.

[92] J. Sigman, C. D. Nordquist, P. G. Clem, G. M. Kraus, and P. S. Finnegan, "Voltage-controlled Ku-band and X-band tunable combline filters using barium-strontium-titanate," *Microwave and Wireless Components Letters, IEEE*, vol. 18, no. 9, pp. 593–595, 2008.

[93] E. Rothwell and M. Cloud, *Electromagnetics*, ser. Electrical engineering textbook series. Newyork, NY: Taylor & Francis Group, 2009.

[94] Sandia National Laboratories, "The cubit geometry and mesh generation toolkit," May 2013. [Online]. Available: http://cubit.sandia.gov/

[95] D. K. Sun, Z. Cendes, and J.-F. Lee, "Adaptive mesh refinement, h-version, for solving multiport microwave devices in three dimensions," *Magnetics, IEEE Transactions on*, vol. 36, no. 4, pp. 1596–1599, 2000.

[96] P. Solin, L. Dubcova, J. Cerveny, and I. Dolezel, "Adaptive hp-FEM with arbitrary-level hanging nodes for maxwellâĂŹs equations," *Advances in Applied Mathematics and Mechanics*, vol. 2, no. 4, pp. 518–532, 2010.

[97] J. R. Shewchuk, "Delaunay refinement algorithms for triangular mesh generation," *Computational geometry*, vol. 22, no. 1, pp. 21–74, 2002.

[98] H. Si, "Three dimensional boundary conforming delaunay mesh generation," Ph.D. dissertation, Technischen Universität Berlin, 2008.

[99] P. Ciarlet, *The finite element method for elliptic problems*, ser. Studies in Mathematics and Its Applications, J. L. Lions, G. Papanicolaou, and R. T. Rockafellar, Eds. North-Holland, 1978.

[100] P. Monk, *Finite element methods for Maxwell's equations*. Oxford: Oxford University Press, 2003.

[101] G. Pelosi, S. Selleri, and R. Coccioli, *Quick Finite Element Methods for Electromagnetic Waves*, 2nd ed. Norwood, MA: Artech House, Inc., 2009.

[102] J.-C. Nédélec, "Mixed finite elements in $\mathbb{R}^3$," *Numerische Mathematik*, vol. 35, no. 3, pp. 315–341, 1980.

[103] J.-M. Jin, J. Jin, and J.-M. Jin, *The finite element method in electromagnetics*. Wiley New York, 2002.

[104] P. P. Silvester and R. L. Ferrari, *Finite elements for electrical engineers*. Newyork, NY: Cambridge University Press, 1996.

[105] D. Jiao, J. Zhu, and S. Chakravarty, "A fast frequency-domain eigenvalue-based approach to full-wave modeling of large-scale three-dimensional on-chip interconnect structures," *Advanced Packaging, IEEE Transactions on*, vol. 31, no. 4, pp. 890–899, 2008.

[106] O. Farle, V. Hill, and R. Dyczij-Edlinger, "Finite-element waveguide solvers revisited," *Magnetics, IEEE Transactions on*, vol. 40, no. 2, pp. 1468–1471, 2004.

[107] R. R. B. Lehoucq, D. D. C. Sorensen, and C.-C. Yang, *Arpack User's Guide: Solution of Large-Scale Eigenvalue Problems With Implicityly Restorted Arnoldi Methods*. Siam, 1998, vol. 6.

[108] M. E. Rognes, R. C. Kirby, and A. Logg, "Efficient assembly of $\mathcal{H}$(div) and $\mathcal{H}$(curl) conforming finite elements," *SIAM Journal on Scientific Computing*, vol. 31, no. 6, pp. 4130–4151, 2009.

[109] W. Rachowicz and A. Zdunek, "An hp-adaptive finite element method for scattering problems in computational electromagnetics," *International Journal for Numerical Methods in Engineering*, vol. 62, no. 9, pp. 1226–1249, 2005.

[110] S. Zaglmayr, "High order finite element methods for electromagnetic field computation," Ph.D. dissertation, 2006.

[111] P. Keast, "Moderate-degree tetrahedral quadrature formulas," *Computer Methods in Applied Mechanics and Engineering*, vol. 55, no. 3, pp. 339–348, 1986.

[112] D.-K. Sun, J.-F. Lee, and Z. Cendes, "Construction of nearly orthogonal nedelec bases for rapid convergence with multilevel preconditioned solvers," *SIAM Journal on Scientific Computing*, vol. 23, no. 4, pp. 1053–1076, 2001.

[113] P. Ingelström, "A new set of $\mathcal{H}$(curl)-conforming hierarchical basis functions for tetrahedral meshes," *Microwave Theory and Techniques, IEEE Transactions on*, vol. 54, no. 1, pp. 106–114, 2006.

[114] B. Chapman, G. Jost, and R. Van Der Pas, *Using OpenMP: portable shared memory parallel programming*. Cambridge, MA: The MIT Press, 2008.

[115] R. Shahnaz, A. Usman, and I. R. Chughtai, "Review of storage techniques for sparse matrices," in *9th International Multitopic Conference, IEEE INMIC 2005*. IEEE, 2005, pp. 1–7.

[116] Y. Renard and J. Pommier, "GMM++: a generic template matrix C++ library," *Short User Documentation, MIP, INSAT, Complexe scientifique de Rangueil*, vol. 31077, 2005.

[117] E. Anderson, Z. Bai, C. Bischof, J. Demmel, J. Dongarra, J. Du Croz, A. Greenbaum, S. Hammarling, A. McKenney, S. Ostrouchov *et al.*, *LAPACK Users' guide*. Society for Industrial and Applied Mathematics Philadelphia, 1995.

[118] Intel® Corporation, "Intel Math Kernel Library," 2013. [Online]. Available: http://software.intel.com/en-us/intel-mkl

[119] O. Schenk, K. Gärtner, W. Fichtner, and A. Stricker, "PARDISO: a high-performance serial and parallel sparse linear solver in semiconductor device simulation," *Future Generation Computer Systems*, vol. 18, no. 1, pp. 69–78, 2001.

[120] T. A. Davis, "Algorithm 832: UMFPACK V4. 3—an unsymmetric-pattern multifrontal method," *ACM Transactions on Mathematical Software (TOMS)*, vol. 30, no. 2, pp. 196–199, 2004.

[121] P. R. Amestoy, I. S. Duff, J.-Y. L'Excellent, and J. Koster, "MUMPS: a general purpose distributed memory sparse solver," in *Applied Parallel Computing. New Paradigms for HPC in Industry and Academia*. Springer, 2001, pp. 121–130.

[122] X. S. Li, J. Demmel, J. Gilbert, L. Grigori, and M. Shao, "SuperLU," in *Encyclopedia of Parallel Computing*. Springer, 2011, pp. 1955–1962.

[123] Z. Xianyi, W. Qian, and Z. Yunquan, "Openblas," http://www.openblas.net/, 2013.

[124] G. Karypis and V. Kumar, "Metis-unstructured graph partitioning and sparse matrix ordering system, version 2.0," 1995.

[125] Y. Saad, *Iterative Methods for Sparse Linear Systems*, 3rd ed. Philadelphia, PA: SIAM, 2000.

[126] C. Greif and D. Schötzau, "Preconditioners for the discretized time-harmonic maxwell equations in mixed form," *Numerical Linear Algebra with Applications*, vol. 14, no. 4, pp. 281–297, 2007.

[127] R. Kechroud, A. Soulaimani, Y. Saad, and S. Gowda, "Preconditioning techniques for the solution of the helmholtz equation by the finite element method," *Mathematics and Computers in Simulation*, vol. 65, no. 4, pp. 303–321, 2004.

[128] Y. Saad, "SPARSEKIT: a basic toll kit for sparse matrix computations," University of Minnesota, Computer Science Department, Tech. Rep., 1994.

[129] ——, "ILUT: A dual threshold incomplete LU factorization," *Numerical linear algebra with applications*, vol. 1, no. 4, pp. 387–402, 1994.

[130] R. Barrett, *Templates for the solution of linear systems: building blocks for iterative methods*. SIAM, 1994, no. 43.

[131] S. J. Orfanidis, *Electromagnetic waves and antennas*. Rutgers University, 2002.

[132] R. Szeliski, "Rapid octree construction from image sequences," *CVGIP: Image understanding*, vol. 58, no. 1, pp. 23–32, 1993.

[133] W. Schroeder, K. Martin, and B. Lorensen, *The Visualization Toolkit–An Object-Oriented Approach To 3D Graphics*, 4th ed. Kitware, Inc., 2006.

[134] J.-F. Remacle, N. Chevaugeon, E. Marchandise, and C. Geuzaine, "Efficient visualization of high-order finite elements," *International Journal for Numerical Methods in Engineering*, vol. 69, no. 4, pp. 750–771, 2007.

[135] L. Bui, D. Ball, and T. Itoh, "Broad-band millimeter-wave E-plane bandpass filters (short papers)," *Microwave Theory and Techniques, IEEE Transactions on*, vol. 32, no. 12, pp. 1655–1658, 1984.

[136] L. Lucci, G. Pelosi, S. Selleri, and R. Nesti, "Corrugated horn antennas," in *Encyclopedia of RF and Microwave Engineering*, K. Chang, Ed. John Wiley & Sons, Inc., 2005, vol. 1, pp. 833–849.

[137] J. Sun, G. D. Peterson, and O. O. Storaasli, "High-performance mixed-precision linear solver for FPGAs," *Computers, IEEE Transactions on*, vol. 57, no. 12, pp. 1614–1623, 2008.

[138] H. Schwarz, *Gesammelte Mathematische Abhandlungen*. Berlin: Springer, 1890, vol. 2.

[139] P.-L. Lions, "On the schwarz alternating method. iii: a variant for nonoverlapping subdomains," in *Third international symposium on domain decomposition methods for partial differential equations*, vol. 6. SIAM, Philadelphia, PA, 1990, pp. 202–223.

[140] C. Farhat and F.-X. Roux, "A method of finite element tearing and interconnecting and its parallel solution algorithm," *International Journal for Numerical Methods in Engineering*, vol. 32, no. 6, pp. 1205–1227, 1991.

[141] B. Després, "Méthodes de décomposition de domaine pour les problèmes de propagation d'ondes en régime harmonique," Ph.D. dissertation, Université Paris IX – Dauphine, 1991.

[142] B. Després, P. Joly, and J. Roberts, "A domain decomposition method for the harmonic maxwell equations," in *Iterative methods in linear algebra, North-Holland*, 1991, pp. 245–252.

[143] M. Vouvakis, K. Zhao, and J.-F. Lee, "Modeling large almost periodic structures using a non-overlapping domain decomposition method," in *Antennas and Propagation Society International Symposium, 2004. IEEE*, vol. 1, june 2004, pp. 343 – 346.

[144] S.-C. Lee, M. N. Vouvakis, and J.-F. Lee, "A non-overlapping domain decomposition method with non-matching grids for modeling large finite antenna arrays," *Journal of Computational Physics*, vol. 203, no. 1, pp. 1–21, 2005.

[145] M. Vouvakis, Z. Cendes, and J.-F. Lee, "A FEM domain decomposition method for photonic and electromagnetic band gap structures," *Antennas and Propagation, IEEE Transactions on*, vol. 54, no. 2, pp. 721 – 733, feb. 2006.

[146] Y. Saad and M. H. Schultz, "GMRES: A generalized minimal residual algorithm for solving nonsymmetric linear systems," *SIAM Journal on scientific and statistical computing*, vol. 7, no. 3, pp. 856–869, 1986.

[147] R. Dyczij-Edlinger, G. Peng, and J.-F. Lee, "Efficient finite element solvers for the maxwell equations in the frequency domain," *Computer methods in applied mechanics and engineering*, vol. 169, no. 3, pp. 297–309, 1999.

[148] H. De Gersem, H. Vande Sande, and K. Hameyer, "Strong coupled multiharmonic finite element simulation package," *COMPEL*, vol. 20, no. 2, pp. 535–546, 2001.

[149] D. M. Copeland and U. Langer, "Domain decomposition solvers for nonlinear multiharmonic finite element equations," *Journal of Numerical Mathematics*, vol. 18, no. 3, pp. 157–175, 2010.

[150] M. Kolmbauer and U. Langer, "A frequency-robust solver for the time-harmonic eddy current problem," in *Scientific Computing in Electrical Engineering SCEE 2010*. Springer, 2012, pp. 97–105.

[151] L. Ntibarikure, G. Pelosi, and S. Selleri, "Efficient harmonic balance analysis of waveguide devices with nonlinear dielectrics," *Microwave and Wireless Components Letters, IEEE*, vol. 22, no. 5, pp. 221–223, 2012.

[152] ——, "Harmonic balance domain decomposition finite elements for nonlinear passive microwave devices analysis," *Special Issue on "Finite Elements for Microwave Engineering," Electromagnetics*, vol. 34, no. 3, 2014.

[153] G. Guarnieri, G. Pelosi, L. Rossi, and S. Selleri, "A domain decomposition technique for efficient iterative solution of nonlinear electromagnetic problems," *Antennas and Propagation, IEEE Transactions on*, vol. 58, no. 12, pp. 4090–4095, Dec. 2010.

[154] F. Bachinger, U. Langer, and J. Schöberl, "Numerical analysis of nonlinear multiharmonic eddy current problems," *Numerische Mathematik*, vol. 100, no. 4, pp. 593–616, 2005.

[155] P. Silvester and R. Ferrari, *Finite Element for Electrical Engineering*. New York, NY: Cambridge University Press, 1997, ch. 5, pp. 187–190.

[156] M. Frigo and S. G. Johnson, "The design and implementation of FFTW3," *Proceedings of the IEEE*, vol. 93, no. 2, pp. 216–231, 2005, special issue on "Program Generation, Optimization, and Platform Adaptation".

[157] J. G. Van Bladel, *Electromagnetic fields*, 2nd ed. Hoboken, NJ: John Wiley & Sons, Inc., 2007, ch. Appendix 2–3, pp. 1001–1033.

[158] V. Yatsyk, "Resonant scattering by layered structure with weakly Kerr-like dielectric nonlinearity," in *International Conference on Mathematical Methods in Electromagnetic Theory, Kharkiv, Ukraine*, June 26-29 2006, pp. 497–499.

[159] G. Guarnieri, G. Pelosi, L. Rossi, and S. Selleri, "A domain decomposition technique for finite element based parametric sweep and tolerance analyses of microwave passive devices," *International Journal of RF and Microwave Computer-Aided Engineering*, vol. 19, no. 3, pp. 328–337, May 2009.

[160] M. Koshiba and M. Suzuki, "Finite-element analysis of h-plane waveguide junction with arbitrarily shaped ferrite post," *Microwave Theory and Techniques, IEEE Transactions on*, vol. 34, no. 1, pp. 103–109, 1986.

[161] Y. Gim, T. Hudson, Y. Fan, C. Kwon, A. T. Findikoglu, B. J. Gibbons, B. H. Park, and Q. X. Jia, "Microstructure and dielectric properties of $Ba_{1-x}Sr_{x}TiO_3$ films grown on $LaAlO_3$ substrates," *Applied Physics Letters*, vol. 77, no. 8, pp. 1200–1202, 2000.

[162] J. Henrie, A. Christianson, and W. J. Chappell, "Prediction of passive intermodulation from coaxial connectors in microwave networks," *Microwave Theory and Techniques, IEEE Transactions on*, vol. 56, no. 1, pp. 209–216, 2008.

[163] G. Lin, C. Wang, W. You, and Y. Wan, "The design of passive intermodulation test system applied in lte 2600," in *Unifying Electrical Engineering and Electronics Engineering*. Springer, 2014, pp. 1519–1526.

[164] J. Sigman, C. Nordquist, P. G. Clem, G. Kraus, and P. Finnegan, "Voltage-controlled ku-band and x-band tunable combline filters using barium-strontium-titanate," *IEEE Microwave and Wireless Components Letters*, vol. 18, no. 9, pp. 593–595, 2008.

[165] X.-Y. Zhang, P. Wang, S. Sheng, F. Xu, and C. K. Ong, "Ferroelectric $Ba_xSr_{1-x}TiO_3$ thin-film varactors with parallel plate and interdigital electrodes for microwave applications," *Journal of Applied Physics*, vol. 104, no. 12, p. 124110, 2008.

[166] S. L. Delprat, J. Oh, F. Xu, L. Li, E. E. Djoumessi, M. Ismail, M. Chaker, and K. Wu, "Fully distributed tunable bandpass filter based on ba0.5sr0.5tio3 thin-film slow-wave structure," 2011.

[167] Y. Pu, R. Grange, C.-L. Hsieh, and D. Psaltis, "Nonlinear optical properties of core-shell nanocavities for enhanced second-harmonic generation," *Physical review letters*, vol. 104, no. 20, p. 207402, 2010.

[168] F. Dutto, C. Raillon, K. Schenk, and A. Radenovic, "Nonlinear optical response in single alkaline niobate nanowires," *Nano letters*, vol. 11, no. 6, pp. 2517–2521, 2011.